

# Computational modeling of glutamate-induced calcium signal generation and propagation in astrocytes

vorgelegt von

Master of Science

**Franziska Oschmann**

geb. in Aachen

von der Fakultät IV – Elektrotechnik und Informatik  
der Technischen Universität Berlin



zur Erlangung des akademischen Grades

Doktor der Naturwissenschaften

- Dr. rer. nat. -

genehmigte Dissertation

Promotionsausschuss:

Vorsitzender: Prof. Dr. Henning Sprekeler

Gutachter: Prof. Dr. Klaus Obermayer

Gutachter: Prof. Dr. Christine Rose

Gutachter: Prof. Dr. Susanne Schreiber

Gutachter: Dr. Hugues Berry

Tag der wissenschaftlichen Aussprache: 26. Oktober 2018

Berlin 2018



Für meinen lieben Thomas, meine Eltern und ihre Ehepartner . . .



# Acknowledgements

First of all I would like to thank Prof. Dr. Klaus Obermayer for his support and supervision of my doctoral thesis. I am especially grateful that he gave me the possibility to write a master's thesis and later a doctoral thesis in a computational field, although I had a mainly experimental background. I found this time very instructive and highly enjoyed the work in his interdisciplinary Neural Information Processing Group at Technische Universität Berlin.

Next, I would like to thank the other members of my committee: Prof. Dr. Christine Rose, Prof. Dr. Susanne Schreiber, Dr. Hugues Berry and Prof. Dr. Henning Sprekeler, for the examination and evaluation of my doctoral thesis. Furthermore, I would like to thank Prof. Dr. Christine Rose and Dr. Hugues Berry for their scientific cooperation over the past years and for the discussions and suggestions concerning my PhD project that were quite important to me.

I thank the Bernstein Center Berlin for their scientific and financial support, which allowed me to invite speakers from the field and to attend international conferences. Especially, I would like to thank Margret Franke and Robert Martin, who were supportive throughout my time in Berlin.

I thank the whole NI-group very much, for just being the best group one could imagine working in. I highly enjoyed being a part of the group and will miss our daily lunch and coffee breaks, the summer and Christmas parties or just the small chats on the hallway. Also I would like to thank Camilla for making everything run smoothly in the group.

I would also like to thank my family, who supported me mentally during my studies and my doctoral thesis. In particular, I would like to thank Thomas for bringing me down to earth in stressful situations and for his support and encouragement throughout the whole time.



# Abstract

Since the 1990s researchers have shown that astrocytes generate calcium oscillations in response to neuronal activity and propagate them as intercellular calcium waves over long distances. Moreover, astrocytes release transmitters in a calcium-dependent manner and by that signal to neurons. These discoveries have made astrocytes and especially calcium signal generation and propagation in astrocytes an important research area in the neuroscience field. However, although the impact of astrocytes at single synapses is well understood, the functional role of astrocytes in neuronal networks is not captured yet. Therefore, it is of high importance to fully understand the generation and propagation of calcium signals, in order to predict the behavior of neuron-astrocyte networks. Coupled with that, the development of computational models has become an important method in the analysis and prediction of astrocytic calcium dynamics.

In the first part of my thesis, I develop a computational model reproducing the calcium signal generation at different positions along a subcellular compartment of the astrocyte, the astrocytic process. The novelty of my approach is the consideration of two interacting mechanisms for the generation of astrocytic calcium signals, namely the calcium entry from the extracellular space and the calcium release from internal stores. In addition, I apply parameters defining the astrocyte morphology in order to predict the calcium signal generation at different positions across the astrocyte. With this model I show that 1) seemingly there is a spatial separation of these two calcium signal generation mechanisms across the astrocyte, and 2) a high activity of both mechanisms evokes a depletion of the internal calcium store and the suppression of intracellular calcium oscillations.

In the second part of my thesis, I develop a reduced model for calcium signal generation in astrocytes and perform a stability analysis of this reduced model. The model reduction is based on the separation of time-scales of the dynamical variables and the subsequent derivation and application of the time-independent solutions of the fast-reacting variables. The stability analysis of the reduced system revealed that 1) the fixed-points of all dynamical variables are independent of those two parameters determining the impact of either the calcium release from internal stores or the calcium entry from the extracellular space and are solely determined by the extracellular stimulation, 2) the stabilities of all fixed points, however, are determined by these two parameters, and 3) the eigenvalues of the fixed points predict that the in part 1 observed depletion of internal calcium stores can be prevented by an increased transport of calcium into internal stores.

In the third part of my thesis, I study the propagation of calcium signals along astrocytic outgrowths, astrocytic processes, with the help of a multi-compartment model. I derive the multi-compartment model by the diffusive coupling of single point-models of astrocytes which I introduce in the first part of the thesis. With the help of this spatial model I discover, that there is a strong interaction between the sodium and the calcium signal propagation, and that the sodium signal carries the calcium signal in astrocytic regions devoid of the internal calcium store.

In summary, this thesis demonstrates the high benefit of computational modeling in the investigation of calcium dynamics in astrocytes and contributes to a better understanding of calcium signal generation and propagation in astrocytes.

# Zusammenfassung

Seit den 1990er Jahren haben Forscher gezeigt, dass Astrozyten als Reaktion auf neuronale Aktivität Calciumschwingungen erzeugen und diese als interzelluläre Calciumwellen über weite Strecken weiterleiten. Darüber hinaus schütten Astrozyten Transmitter in Abhängigkeit von den generierten Calciumsignalen aus und beeinflussen damit Neuronen. Diese Entdeckungen haben Astrozyten und insbesondere die Erzeugung und Vermehrung von Calciumsignalen in Astrozyten zu einem wichtigen Forschungsgebiet der Neurowissenschaften gemacht. Obwohl der Einfluss von Astrozyten auf einzelne Synapsen gut erforscht ist, ist die funktionelle Rolle von Astrozyten in neuronalen Netzwerken noch unklar. Daher ist es von großer Bedeutung, die Erzeugung und Ausbreitung von Calciumsignalen vollständig zu verstehen, um das Verhalten von Neuronen-Astrozyten-Netzwerken vorherzusagen. Damit verbunden ist die Entwicklung von mathematischen Modellen zu einer wichtigen Methode zur Analyse und Vorhersage der Calciumdynamik in Astrozyten geworden.

Im ersten Teil meiner Doktorarbeit entwickle ich ein mathematisches Modell, das die Calciumsignalerzeugung an verschiedenen Positionen entlang eines subzellulären Kompartiments des Astrozyten, dem astrozytischen Prozess, reproduziert. Die Neuheit meines Ansatzes ist die Berücksichtigung zweier interagierender Mechanismen zur Erzeugung der Calciumsignale in Astrozyten, nämlich der Calciumeinstrom aus dem extrazellulären Raum und die Calciumausschüttung aus den inneren Calciumspeichern. Zusätzlich wende ich Parameter an, die die Astrozytenmorphologie definieren, wie der Volumenanteil des internen Calciumspeichers oder das Oberflächen-Volumen-Verhältnis des Astrozyten. Mit diesem Modell zeige ich, dass 1) scheinbar eine räumliche Trennung dieser beiden Erzeugungsmechanismen für das Calciumsignal entlang des astrozytischen Prozesses stattfindet, und 2) ein hoher Calciumeinstrom aus dem extrazellulären Raum eine Erschöpfung des inneren Calciumspeichers und die Unterdrückung intrazellulärer Calciumschwingungen hervorruft.

Im zweiten Teil meiner Doktorarbeit entwickle ich ein reduziertes Modell für die Generierung von Calciumsignalen in Astrozyten und führe eine Stabilitätsanalyse dieses reduzierten Modells durch. Die Modellreduktion basiert auf der Trennung der Zeitskalen der dynamischen Variablen und der anschließenden Berechnung und Anwendung der zeitunabhängigen Lösungen der schnell reagierenden Variablen. Die Stabilitätsanalyse des reduzierten Systems ergab, dass 1) die Fixpunkte aller dynamischen Variablen unabhängig von den beiden Parametern sind, die den

Einfluss entweder der Calciumausschüttung aus internen Speichern oder des Calciumeintrags aus dem extrazellulären Raum bestimmen und ausschließlich durch die extrazelluläre Stimulation bestimmt werden, 2) die Stabilitäten aller Fixpunkte jedoch durch diese beiden Parameter bestimmt werden, und 3) die Eigenwerte der Fixpunkte vorhersagen, dass die in Teil 1 beobachtete Erschöpfung der internen Calciumspeicher durch einen erhöhten Rücktransport von Calcium in interne Speicher verhindert werden kann.

Im dritten Teil meiner Doktorarbeit untersuche ich die Ausbreitung von Calciumsignalen in astrozytären Prozessen mit Hilfe eines Mehrkammermodells. Ich leite das Mehrkammermodell durch die diffusive Kopplung der Punktmodelle der Astrozyten ab, die ich im ersten Teil der Arbeit vorgestellt habe. Mit Hilfe dieses räumlichen Modells entdeckte ich, dass 1) die Wechselwirkung zwischen den beiden Erzeugungsmechanismen für Calciumsignale auch die Calciumausbreitung in Abhängigkeit von der Stärke beider Mechanismen begünstigt oder behindert, und 2) das ausbreitende Natriumsignal in der Lage ist, das Calciumsignal in astrozytischen Teilen ohne interne Calciumspeicher zu transportieren.

Zusammenfassend zeigt diese Arbeit den hohen Nutzen der mathematischen Modellierung bei der Untersuchung der Calciumdynamik in Astrozyten und trägt zu einem besseren Verständnis der Erzeugung und Ausbreitung von Calciumsignalen bei.

# Contents

<b>Introduction</b>	<b>1</b>
1 Discovery of astrocytes . . . . .	1
2 Morphology of astrocytes . . . . .	2
3 Physiology of astrocytes . . . . .	3
3.1 Intracellular calcium dynamics . . . . .	3
3.2 Intracellular sodium dynamics . . . . .	5
3.3 Intracellular potassium dynamics . . . . .	6
4 Computational models for calcium signal generation in astrocytes . .	7
5 Motivation . . . . .	7
<b>1 Computational modeling of astrocytic calcium dynamics within a single compartment</b>	<b>9</b>
<b>Introduction</b>	<b>11</b>
<b>Model</b>	<b>13</b>
1 Computational model for $\text{Ca}^{2+}$ release from internal stores . . . . .	13
1.1 Computational model for $\text{Ca}^{2+}$ release from internal stores by DePitta et al., 2009 . . . . .	13
1.2 Changes of the model by De Pittà et al. (2009) . . . . .	16
2 Extension of the model of De Pittà et al. (2009) and introduction of $\text{Na}^+$ , $\text{K}^+$ and $V$ dynamics . . . . .	18
2.1 Dynamics of the ion concentrations and the membrane voltage	18
3 Neuronal stimulation of the astrocyte compartment . . . . .	22
4 Model parameter values . . . . .	23
5 Computational methods . . . . .	25
<b>Results</b>	<b>27</b>
1 $\text{Ca}^{2+}$ release from the internal $\text{Ca}^{2+}$ store along the astrocytic process	27
2 $\text{Ca}^{2+}$ entry from the extracellular space . . . . .	28
2.1 $\text{Na}^+$ entry into the astrocyte . . . . .	28
2.2 $\text{Ca}^{2+}$ transport through the plasma membrane . . . . .	30
2.3 Impact of the glutamate transporter activity on the $\text{Ca}^{2+}$ response under synaptic stimulation . . . . .	33

2.4	Interaction of the mGluR-dependent and GluT-dependent pathway . . . . .	35
	<b>Discussion</b>	<b>37</b>
	<b>2 Model reduction</b>	<b>39</b>
	<b>Introduction</b>	<b>41</b>
	<b>Model</b>	<b>43</b>
1	Model reduction . . . . .	43
1.1	Reduced model . . . . .	49
1.2	Model behavior in response to parameter variations and stability analysis of the reduced model . . . . .	50
1.3	Initialization of the dynamical system . . . . .	53
1.4	Computational methods . . . . .	54
	<b>Results</b>	<b>55</b>
1	Comparison of the full and the reduced model . . . . .	55
1.1	Analysis of the reduced model . . . . .	56
1.2	Prediction of the model behavior based on the eigenvalues of the Jacobian matrix . . . . .	59
	<b>Discussion</b>	<b>61</b>
	<b>3 Multi-compartment model for the signal propagation</b>	<b>65</b>
	<b>Introduction</b>	<b>67</b>
	<b>Model</b>	<b>69</b>
1	Astrocyte morphology . . . . .	69
2	Multi-compartment model . . . . .	71
2.1	General form of the diffusion equation . . . . .	71
2.2	Time- and space-dependent changes of $\text{Ca}^{2+}$ , $\text{Na}^+$ , $\text{K}^+$ and $\text{IP}_3$	72
2.3	Time- and space-dependent changes of the membrane potential	73
3	Morphology of the multi-compartment model . . . . .	75
3.1	Connectivity matrix for open and sealed end condition . . . . .	75
3.2	Connectivity matrix for a branching process . . . . .	76
4	Model parameter values . . . . .	77
	<b>Results</b>	<b>79</b>
1	$\text{Na}^+$ diffusion in astrocytic processes . . . . .	79
2	$\text{Ca}^{2+}$ signal propagation within an astrocytic process . . . . .	86
3	Model morphologies . . . . .	91
3.1	Branching of the astrocytic process . . . . .	91

3.2	Open and sealed end of the astrocytic process . . . . .	92
4	Modeling of the perisynaptic astrocytic process . . . . .	94
<b>Discussion</b>		<b>97</b>
1	Discussion . . . . .	101
2	Outlook . . . . .	102



# List of Figures

0.1	Drawing of astrocytes by Cajal. . . . .	2
1.1	Geometry of a single astrocytic compartment. . . . .	16
1.2	The volume ratio of the endoplasmatic reticulum (ER) as a function of the surface volume ratio (SVR). . . . .	17
1.3	Ca <sup>2+</sup> signal generation in astrocytes. . . . .	19
1.4	Ca <sup>2+</sup> concentration dynamics in the intracellular compartment during synaptic activation. . . . .	28
1.5	Intracellular Na <sup>+</sup> concentration dynamics during a constant extracellular glutamate concentration. . . . .	29
1.6	Intracellular Ca <sup>2+</sup> concentration dynamics for different values of the maximal pump current of the Na <sup>+</sup> -Ca <sup>2+</sup> exchanger. . . . .	31
1.7	Ca <sup>2+</sup> oscillation frequency and amplitude for different parameter combinations of the volume fraction of the internal store and the maximal pump currents of the membrane transporters. . . . .	32
1.8	Intracellular Ca <sup>2+</sup> concentration dynamics under synaptic stimulation for a blocked glutamate transporter (GluT) in comparison to the control condition. . . . .	34
1.9	Increase of the intracellular Na <sup>+</sup> concentration during synaptic stimulation. . . . .	35
1.10	Behavior of the dynamical variables as a function of the maximal pump current of the Na <sup>+</sup> -Ca <sup>2+</sup> exchanger and the volume fraction of the internal Ca <sup>2+</sup> store. . . . .	36
2.1	The time-dependent behavior of the dynamical variables of the full model. . . . .	43
2.2	The current strengths of the membrane transporters. . . . .	44
2.3	The Na <sup>+</sup> <sub>i</sub> , K <sup>+</sup> <sub>i</sub> and V dynamics as a function of the glutamate concentration. . . . .	45
2.4	Calculated steady state values of K <sup>+</sup> (K <sup>+</sup> <sub>ss</sub> ) and V (V <sub>ss</sub> ) given the computed steady state values of Na <sup>+</sup> (Na <sup>+</sup> <sub>ss</sub> ). . . . .	46
2.5	The values of Na <sup>+</sup> <sub>ss</sub> and glutamate determine the values of K <sup>+</sup> <sub>ss</sub> and V <sub>ss</sub> . . . . .	46
2.6	The simulated and fitted steady state values Na <sup>+</sup> <sub>ss</sub> , K <sup>+</sup> <sub>ss</sub> and V <sub>ss</sub> as a function of the applied glutamate concentration. . . . .	48
2.7	Comparison of a dynamic and a constant extracellular Ca <sup>2+</sup> concentration. . . . .	49

2.8	The oscillatory behaviors of the full and the reduced model. . . . .	55
2.9	Stability behavior of the reduced model. . . . .	57
2.10	The real parts of the eigenvalues mainly predict the transition between oscillatory and non-oscillatory model behavior. . . . .	58
2.11	The eigenvalues of the Jacobian matrix predict the boundary between the oscillatory and the non-oscillatory range of the reduced model. . . . .	60
3.1	Scheme of the astrocyte morphology. . . . .	69
3.2	Morphological parameters of the astrocytic process. . . . .	70
3.3	Scheme of a branching process. . . . .	76
3.4	Amplitude and pace of the $\text{Na}^+$ signal propagation within an astrocytic process. . . . .	80
3.5	Amplitude and pace of the $\text{Na}^+$ signal propagation within an astrocytic process assuming the same tortuosity in the intra- and extracellular space. . . . .	81
3.6	Time-dependent $\text{Na}^+$ signal propagation along the astrocytic process. . . . .	82
3.7	Space-dependent $\text{Na}^+$ signal propagation along the astrocytic process. . . . .	83
3.8	Effect of the tortuosity on the $\text{Na}^+$ diffusion in the intra- and extracellular space. . . . .	84
3.9	$\text{Ca}^{2+}$ signal propagation as a function of the $\text{IP}_3$ and $\text{Ca}^{2+}$ diffusion coefficients. . . . .	86
3.10	$\text{Ca}^{2+}$ signal propagation during a low activity of the $\text{Na}^+$ - $\text{Ca}^{2+}$ exchanger. . . . .	88
3.11	$\text{Ca}^{2+}$ signal propagation during a moderate activity of the $\text{Na}^+$ - $\text{Ca}^{2+}$ exchanger. . . . .	89
3.12	$\text{Ca}^{2+}$ signal propagation during a high activity of the $\text{Na}^+$ - $\text{Ca}^{2+}$ exchanger. . . . .	90
3.13	$\text{Na}^+$ signal propagation in a branching astrocytic process. . . . .	91
3.14	$\text{Ca}^{2+}$ and $\text{Na}^+$ signal propagation along an astrocytic process with either a sealed or an open end. . . . .	93
3.15	Intracellular $\text{Na}^+$ signals drive the $\text{Ca}^{2+}$ signal propagation at perisynaptic astrocytic processes. . . . .	95

# List of Tables

1.1	Initial values. . . . .	23
1.2	Model parameters for the dynamics of h. . . . .	23
1.3	Model parameters for the $\text{Ca}^{2+}$ currents at the endoplasmatic reticulum. . . . .	24
1.4	Model parameters for the production and degradation of $\text{IP}_3$ . . . . .	24
1.5	Model parameters for the membrane currents. . . . .	25
1.6	Parameters for the Tsodyks and Markram model. . . . .	25
1.7	Physical constants used in the model. . . . .	25
2.1	Model parameters for the steady-state values of $\text{Na}^+_i$ , $\text{K}^+_i$ and V. . . . .	47
3.1	Morphological parameters of astrocyte. . . . .	71
3.2	Parameters for the propagation of $\text{Ca}^{2+}$ , $\text{Na}^+$ , $\text{IP}_3$ and $\text{K}^+$ . . . . .	77
3.3	Morphological parameters of the multi-compartment model. . . . .	77



# Introduction

## 1 Discovery of astrocytes

The brain consists of two main cell types: neurons and glial cells. While the important function of neurons was recognized early and intensively studied, the relevance of glial cells was unknown for a long time. However, already in the 1850s Rudolf Virchow discovered glial cells and described them as “substance. . . which lies between the proper nervous parts, holds them together and gives the whole its form in a greater or lesser degree” (Virchow, 1858; Kettenmann and Verkhratsky, 2008). His finding was followed by numerous reports about different types of glial cells discovered in the brain like Müller cells or Bergmann glia. The black staining reaction developed by Golgi allowed the detailed study of the glial cell morphology. Based on his drawings Golgi suggested that glial cells form the metabolic link between blood vessels and the brain parenchyma and by that take on a nutritive role. Finally, Ramón y Cajal developed the first specific staining method for astrocytes and by that allowed the specific investigation of astroglia (Kettenmann and Verkhratsky, 2008).

Unlike neurons, however, astrocytes are electrically non-excitabile and only display small changes in their membrane potential in response to stimulations like current injection (Kang et al., 1998; Nedergaard et al., 2003). This is why astrocytes were initially not considered as active partners in information transmission. Instead, it was thought that astrocytes function as metabolic supporters of neurons and mediate the glutamate synthesis for neurons (Norenberg and Martinez-Hernandez, 1979). Only when the first researchers detected calcium signals in astrocytes in response to neuronal activity, the view on astrocytes changed (Cornell-Bell et al., 1990; Charles et al., 1991). Since then more and more evidence was collected supporting the active role in information transmission of astrocytes like for example at the tripartite synapse (Perea et al., 2009). The main assumption is that calcium is the key component of the astrocyte physiology and plays an active role in the detection and control of neuronal network activity.

In the following, I will give a short overview on the morphology and physiology of astrocytes as well as on the mathematical models describing the calcium signal generation in astrocytes.

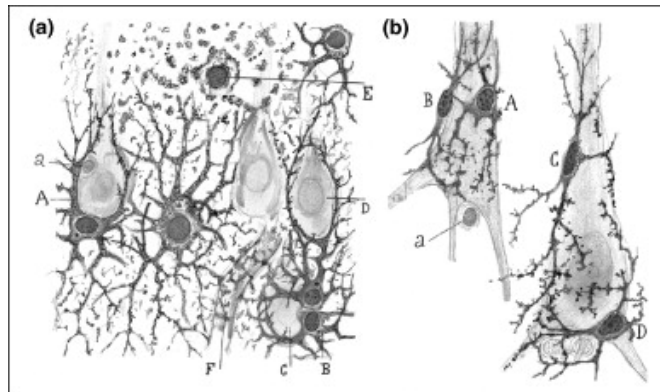


Figure 0.1: **Drawing of astrocytes by Cajal.** **a** Drawing of astrocytes in the pyramidal layer of the human hippocampus. Sublimated gold chloride method. **b** Different astrocytes surrounding neuronal somas in the pyramidal layer of the human hippocampus. Sublimated gold chloride method. Figure and caption adapted from (García-Marín et al., 2007)

## 2 Morphology of astrocytes

Basically, the appearance of astrocytes can be described as star-shaped. Astrocytes have a soma and several outgrowths, called bigger branches (see Figure 0.1). These branches split up into smaller and smaller branches called processes. The ends of these processes are spatially adjacent to the neuronal synapses and are therefore called perisynaptic astrocytic processes. Since these ends of the processes wrap themselves around the synaptic cleft and are thus in direct contact with the neurons, the synapse consists of three parts: the pre- and postsynaptic neuron as well as the astrocyte. A further astrocytic subcellular compartment, the astrocytic endfeet, ensheathes blood-vessels (Mathiisen et al., 2010; McCaslin et al., 2011) and contributes to the generation and maintenance of the blood-brain barrier (Abbott et al., 2006). The cellular morphology and anatomical location of the astrocytes can be divided into two main groups: protoplasmic and fibrous astrocytes.

Protoplasmic astrocytes are found in gray matter. Characteristic for the morphology of protoplasmic astrocytes is that they occupy a spherical volume. The soma gives rise to several radially spreading stem branches which split into fine processes (Kettenmann and Ransom, 2013, p. 38). These cell extensions occupy 50% of the volume and even 80% of the surface of the astrocyte. This results in a high surface-to-volume ratio which allows the astrocytes to contact as much neurons as possible (Kettenmann and Ransom, 2013, p. 38).

Fibrous astrocytes are found in white matter. The somas of fibrous astrocytes are organized in rows between the axon bundles and give rise to many long fiber-like processes which are oriented in parallel to the axons. The processes of fibrous astrocytes are longer than those of protoplasmic astrocytes. In mice, for example, the length of fibrous astrocytes is 300  $\mu\text{m}$ , while processes of protoplasmic astrocytes are less than 50  $\mu\text{m}$  long (Kettenmann and Ransom, 2013, p. 39).

### 3 Physiology of astrocytes

Unlike neurons astrocytes do not generate action potentials, but exhibit changes in their intracellular calcium concentration in response to transmitter release by neurons (Cornell-Bell et al., 1990; Charles et al., 1991). This form of astrocyte excitability not only reflects the integration of neuronal activity by astrocytes, but also allows astrocytes to affect neuronal activity by the release of transmitters into the synaptic cleft (Pasti et al., 2001; Henneberger et al., 2010; Sahlender et al., 2014). Besides elevations in the calcium concentration, also sodium and potassium signals have been found to dependent on ion and transmitter changes in the extracellular space evoked by neuronal activity (Kirischuk et al., 2007; Langer and Rose, 2009). However, sodium and potassium signals differ substantially in their propagation radius and their propagation mechanism to calcium signals, so that unlike calcium they are not attributed to the integration of neural network activity.

Astrocytes express a wide variety of ion channels and transporters as well as transmitter receptors, which allows them to sense neuronal activity (for reviews see Verkhratsky et al. (1998) and Verkhratsky and Steinhäuser (2000)). In general, these channels, transporters and receptors can be divided into two subgroups: those activated by changes of the extracellular calcium, sodium or potassium concentration on the one side, and those activated by changes of the extracellular neurotransmitter concentration on the other side. In the following the dynamics of intracellular calcium, sodium and potassium and the contributing channels, transporters and receptors are described.

#### 3.1 Intracellular calcium dynamics

Calcium signals in astrocytes are generated either by calcium release from the internal calcium store (endoplasmatic reticulum) or by calcium entry from the extracellular space. Both the membrane of the internal calcium store and the plasma membrane contain several families of calcium channels, which allow a flow of calcium between the internal calcium store and the intracellular space as well as between the intracellular space and the extracellular space.

The expression of metabotropic receptors, which are activated by the binding of neurotransmitters, enables astrocytes to sense neuronal activity. Upon binding of neurotransmitters to the metabotropic receptors, the second-messenger inositol-triphosphate ( $IP_3$ ) is produced, which activates the calcium release from internal stores (Verkhratsky et al., 1998; Agulhon et al., 2008).

Channels responsible for the release and uptake of calcium at the internal store are for example the  $IP_3$ -gated calcium channels/receptors ( $IP_3R$ ) (Streb et al., 1983; Spät et al., 1986) or the SERCA pump. While the  $IP_3$ -gated calcium channels are mainly responsible for the calcium release from the internal store and thus for the generation of cytoplasmic calcium signals, the SERCA pumps mediate the energy-dependent calcium uptake into the internal store.

A link between the plasma membrane and the internal calcium store allows a store-operated calcium entry into the astrocyte (Putney, 1986). A depletion of the internal calcium store from releasable calcium activates the store-operated calcium entry into

the astrocyte through specific channels and the replenishment of the internal calcium store (Parekh and Lewis, 2005).

The calcium entry from the extracellular space is mediated by several calcium channels located in the plasma membrane. Among others the calcium entry pathway including the sodium-calcium exchanger is of particular interest since it can be activated by an elevation of the extracellular glutamate concentration (Kirischuk et al., 2007). The sodium-calcium exchanger can operate either in the forward or in the reverse mode by exchanging intracellular calcium with extracellular sodium or the other way round. The stoichiometry of that exchange is 3 sodium : 1 calcium. The switch between both modes is regulated by the ion gradients of sodium and calcium as well by the membrane potential (Goldman et al., 1994). For example, an activation of astrocytic glutamate transporters or NMDA receptors induce the accumulation of sodium within the astrocyte (Rose and Karus, 2013). Upon stimulation with glutamate the glutamate transporter mediates the cotransport of one glutamate molecule together with three sodium ions and the countertransport of one potassium ion as well as one proton (Tzingounis and Wadiche, 2007). The generated sodium accumulation in turn activates the sodium-calcium exchanger and gives rise to the transport of calcium into the cell (Rojas et al., 2007).

Recent experimental results suggest that the generation of intracellular calcium signals varies between subcellular compartments. With the discovery that the shape and frequency of calcium signals in the astrocytic processes are significantly different from those in soma (Kanemaru et al., 2014), experimentalists studied the location-dependent generation of calcium signals by knocking out or blocking receptors and transporters (Srinivasan et al., 2015). While a knockout of the IP<sub>3</sub> receptor 2 (IP<sub>3</sub>R2) at the internal calcium store abolished the majority of somatic calcium transients, it had a lower effect on calcium signals in the astrocytic processes (Srinivasan et al., 2015; Stobart et al., 2016). Moreover, while the removal of extracellular calcium had only a minor effect on calcium signals in the soma, it clearly reduced the frequency of calcium transients in the astrocytic processes (Srinivasan et al., 2015). From that it was concluded, that the main source for calcium signal generation in the soma is calcium release from internal stores, while in the astrocytic processes calcium signals are generated by calcium entry from the extracellular space (Bazargani and Attwell, 2016). This finding is also supported by the fact that astrocytic regions close to the synapse, perisynaptic astrocytic processes, are devoid of internal calcium stores. Thus, these regions do not allow calcium release from internal stores Patrushev et al. (2013).

Astrocytic calcium signals are not a local event, but spread throughout the whole astrocyte and even between neighboring astrocytes. The propagation of these calcium waves, however, differ between subcellular compartments of the astrocyte. On the one side, in astrocytic compartments which contain internal calcium stores, the propagation of calcium waves is driven by the diffusion of calcium and of the second messenger IP<sub>3</sub>, which then evokes an intracellular amplification of the calcium signal by calcium release from internal stores (Golovina and Blaustein, 2000; Scemes, 2000; Sheppard et al., 1997). On the other side, in thin astrocytic processes the generation of strong calcium signals by transmembrane calcium transport and

their propagation via diffusion is favored (Rusakov et al., 2011). Single-cell calcium signals do not stop at the astrocyte cell border, but propagate into neighboring astrocytes and by that create an intercellular calcium wave. This intercellular spread of calcium waves through gap junctions travels over long distances (300-400  $\mu\text{m}$ ) and is able to excite up to hundreds of cells (Giaume and Venance, 1998; Scemes and Giaume, 2006). The generation and maintenance of calcium waves is not achieved by the diffusion of calcium itself but by the diffusion of  $\text{IP}_3$  through gap junctions and the subsequent release of calcium from internal stores (Scemes and Giaume, 2006).

### 3.2 Intracellular sodium dynamics

The role of sodium in astrocyte physiology consists of ion regulation and homeostasis on the one side, and the generation of sodium signals in response to neuronal activity on the other side (Rose and Karus, 2013). Although much evidence for both aspects has been found in experiments, these two functions are nevertheless contradictory. Sodium homeostasis provides a low intracellular sodium concentration to maintain the ion gradient, and in contrast, the generation of sodium signals is characterized by a strong increase of the intracellular sodium concentration (for a review see: (Rose and Karus, 2013)).

The sodium homeostasis in astrocytes consists of maintaining a low intracellular sodium concentration and a large inwardly directed concentration gradient. The intracellular sodium concentration is around 15 mM and is therefore significantly lower than the extracellular sodium concentration, which is 145 mM (Kirischuk et al., 2012). Therefore, the transport of sodium against its concentration gradient and thus out of the cell requires energy. This transport is largely handled by the sodium-potassium pump, which exchanges three sodium ions with two potassium ions (Kaplan, 2002). This strong inwardly directed sodium gradient generated by the sodium-potassium pump supports the uptake of ions and transmitters by astrocytes. For example, the uptake of glutamate mediated by the glutamate transporter is accompanied by the transport of three sodium ions into the astrocyte and one potassium ion out of the astrocyte Danbolt (2001). Thus, the uptake of glutamate produces an accumulation of sodium in the intracellular space (Chatton et al., 2000). The close spatial association of the glutamate transporter and the sodium-potassium pump, however, favors the glutamate uptake by astrocytes as the sodium-potassium pump generates a strong inwardly directed sodium gradient and outwardly directed potassium gradient (Rose et al., 2009).

In contrast to the energy-dependent maintenance of a low intracellular sodium concentration is the generation of activity dependent sodium signals. Intracellular sodium signals are induced by an enhanced neuronal activity and subsequent accumulation of neurotransmitters in the extracellular space (Rose, 2002). The uptake of glutamate or GABA from the extracellular space by astrocytes is coupled to the co-transport of sodium (Chatton et al., 2000, 2003).

Moreover, the neurotransmitter-dependent accumulation of sodium in the intracellular space mediates calcium entry into the astrocyte. The rise of the intracellular

sodium concentration evoked by the uptake of, for example, glutamate or GABA cause a switch of the sodium-calcium exchanger into the reverse mode such that calcium is transported into the astrocyte and sodium is transported out of the astrocyte (Rojas et al., 2007; Doengi et al., 2009). This sodium-dependent pathway is of particular interest since it also allows calcium signal generation in response to neuronal transmitter release in astrocytic subcellular compartments which are devoid of internal calcium stores (Patrushev et al., 2013).

Unlike the propagation of calcium signals, the propagation of sodium signals is not affected by intracellular amplification mechanisms and is only determined by sodium diffusion (Rose and Karus, 2013). The diffusion speed of sodium is about  $60 \mu\text{m/s}$  in somatic regions (Langer et al., 2012), and probably even higher in astrocytic processes due to their elaborate morphology (Nedergaard et al., 2003). Within astrocytic endfeet sodium signals spread with a maximum velocity of  $120 \mu\text{m/s}$  (Langer et al., 2016).

### 3.3 Intracellular potassium dynamics

Astrocytes express various types of potassium channels and transporters. These channels and transporters contribute significantly to the membrane potential of astrocytes, since the membrane potential is largely determined by the potassium gradient (Kuffler et al., 1966). Thus, small changes of the extracellular potassium concentration lead to an activation of the potassium transporters and channels as well as a potassium uptake. Therefore, astrocytes play a major role in the buffering of excess extracellular potassium, which is released during neuronal activity. At rest, the extracellular potassium concentration is 3 mM. During intense neuronal activity or epileptiform bursting the extracellular potassium concentration can rise up to 5-15 mM (Somjen, 1979). According to the spatial buffering hypothesis, astrocytes take up this excess potassium from the extracellular space, distribute it within their astrocyte network and release the potassium at sites of lower extracellular potassium concentration (Orkand et al., 1966). Channels and transporters attributed to the uptake of excess extracellular potassium are the sodium-potassium-pump (Walz and Hinks, 1986) or the inward rectifying potassium ( $K_{ir}$ ) channel (Orkand et al., 1966).

The sodium-potassium-pump is responsible for the maintenance of the sodium and potassium ion gradients across the plasma membrane. These ion gradients are maintained by an exchange of intracellular sodium for extracellular potassium with a stoichiometry 3:2. This resulting inwardly directed sodium gradient is used by numerous channels and transporters to generate gradients for other ions such as calcium or potassium (Kettenmann and Ransom, 2013, p. 190). The glutamate uptake mediated by the glutamate transporter, for example, is mainly driven by the inwardly directed sodium and the outwardly directed potassium gradient. Moreover, the glutamate transporters are directly coupled to the sodium-potassium pumps such that the sodium-potassium pumps can control the glutamate uptake (Rose et al., 2009).

## 4 Computational models for calcium signal generation in astrocytes

The discovery of the generation of neuronal-activity dependent calcium signals in astrocytes was accompanied with the development of computational models analyzing and predicting the signal generation in astrocytes (for a review see Oschmann et al. (2017a) and Manninen et al. (2018)).

In the original, two-dimensional model calcium signals are evoked by only one mechanism: the calcium- and  $IP_3$ -dependent release of calcium from the internal calcium store (Li and Rinzel, 1994). Here, solely the calcium dynamics in the internal calcium store and in the intracellular space are considered. This original model constitutes the core mechanism and has been adopted in most subsequent models for calcium signal generation in astrocytes (Höfer et al., 2002; Goto et al., 2004; De Pittà et al., 2009).

The mathematical description of the  $IP_3$ -dynamics in astrocytes is more heterogeneous. In the early models  $IP_3$  is assumed to be a constant parameter (Dupont and Goldbeter, 1993; Li and Rinzel, 1994). These models predict the generation of calcium oscillations also for the application of constant  $IP_3$  levels, despite the fact the time-dependent dynamics of  $IP_3$  is essential for the generation of calcium oscillations. Later models apply a more complete description of the  $IP_3$  dynamics consisting of the agonist-, calcium- and  $IP_3$ -dependent synthesis and degradation of  $IP_3$  (Goto et al., 2004; Nadkarni and Jung, 2007; De Pittà et al., 2009).

Some computational models also consider the calcium entry from the extracellular space and by that assume a combination of calcium generation mechanisms. Applied mechanisms for the calcium entry are voltage-gated calcium channels (Postnov et al., 2008) or store-operated calcium channels (Handy et al., 2017). Most of these mechanisms are not solely driven by calcium, but also by other ions or the membrane potential. Thus, a consideration of these mechanisms results in the consideration of additional model variables.

The spread of calcium waves across astrocyte-networks was investigated by numerous computational models. In general, the coupling of several astrocytes via gap junctions allows the spread of calcium and  $IP_3$  to neighboring astrocytes and by that facilitates intercellular communication. For example, Ullah et al. (2006) showed that the synchronization of intracellular calcium signals across several cells depends on the coupling strength between the astrocytes. Here, the astrocyte-network only consists of two cells. Subsequent studies, however, increased the number of considered astrocytes (Kang and Othmer, 2009) or also included neurons (Amiri et al., 2013).

## 5 Motivation

Although already numerous models addressed the generation of astrocytic calcium signals by calcium release from internal stores, most of them lack the additional contribution of calcium entry from the extracellular space driven by neurotransmitters like glutamate.

Schummers et al. (2008) showed the high dependence of the calcium signal in astro-

cytes on the activity of the glutamate transporter. They observed a strong attenuation of the calcium signal during a block of the glutamate transporter. The glutamate transporter couples the transport of glutamate and sodium and by that induces an accumulation of sodium in the intracellular space. This accumulated sodium is able to activate the sodium-calcium exchanger such that calcium is transported into the astrocyte. By that the transport of glutamate is linked to the calcium transport into the astrocyte. Thus, the glutamate-driven calcium entry via the sodium-calcium exchanger could explain the neurotransmitter-dependent generation of calcium signals in astrocytic regions devoid of internal calcium stores. Moreover, this second pathway also allows a strong interaction of propagating calcium and sodium signals. Thus, based on this mechanism the propagating sodium signal could drive the calcium signal in astrocytic regions devoid of the internal calcium store.

In the first part of my thesis I focus on the development of a computational model for calcium signal generation in astrocytes, which accounts for calcium release from internal stores and calcium entry from the extracellular space both driven by an elevated glutamate level in the extracellular space. Moreover, I include the volume of the internal calcium store as a morphological parameter into the model in order to scale the calcium release from internal stores. With this model I test whether the sodium-calcium exchanger serves as a source for calcium signals in astrocytes and how this second mechanisms affects the calcium release from internal stores.

In the second part of my thesis, I develop a reduced version of the model presented in the first part, which allows an analytic analysis. Starting from that, I first investigate, if the reduced model quantitatively and qualitatively reproduces the behavior of the full model. In a second step I determine, if the analytic determined fixed points and their stabilities are sufficient in order to predict the calcium dynamics without performing a numerical integration.

In the third part of my thesis, I develop a multi-compartment model in order to investigate the calcium signal propagation within the astrocyte. With the help of that model I study how the propagating calcium and sodium signals interact with each other.

## **Part 1**

# **Computational modeling of astrocytic calcium dynamics within a single compartment**



# Introduction

The discovery that astrocytes integrate and process synaptic activity by the generation of intracellular calcium signals (Perea et al., 2009) was accompanied with the development of numerous computational models reproducing and investigating the calcium dynamics of astrocytes (for a review see Oschmann et al. (2017a) or Manninen et al. (2018)). One of the first models designed for this purpose was published by Li and Rinzel (1994) and accounts for calcium oscillations mediated by the second-messenger inositol trisphosphate ( $IP_3$ ). Although this model was not explicitly developed for astrocytes, it constitutes the core mechanisms for numerous models describing astrocytic calcium dynamics (Postnov et al., 2008; Nadkarni and Jung, 2007; De Pittà et al., 2009). The model published by De Pittà et al. (2009) stands out from the other ones since it includes an explicit computation of the  $IP_3$  concentration and by that allows a link between the stimulus, the extracellular glutamate concentration, and the intracellular oscillations of calcium as well as  $IP_3$ .

Although experimental studies have demonstrated that calcium signals are shaped by calcium release from internal stores as well as calcium entry from the extracellular space, the majority of the computational models focuses on the former mechanism. The former mechanism consists of the glutamate dependent production of the second messenger  $IP_3$  by metabotropic glutamate receptors (mGluRs) and the subsequent  $IP_3$ - and calcium-dependent exchange of calcium between the intracellular space and the internal calcium store. The latter mechanisms describes the calcium entry into the astrocyte via for example the sodium-calcium exchanger, which is activated by the glutamate-driven sodium accumulation within the intracellular space of astrocytes.

However, astrocytic calcium signals are not only shaped by different mechanisms, but also by the weighting of these mechanisms, which varies between different subcellular compartments of the astrocyte. These different subcellular compartments are the soma and the astrocytic processes. While calcium release from internal stores primary generates calcium signals in the soma, calcium entry from the extracellular space forms the majority of calcium signals in astrocytic processes (Srinivasan et al., 2015; Stobart et al., 2016; Bindocci et al., 2017). These findings are supported by the fact that the volume fraction of internal calcium stores decreases along the astrocytic process from the soma towards the synapse and perisynaptic astrocytic processes are devoid of internal calcium stores (Patrushev et al., 2013).

Based on the above cited results I hypothesize that calcium signals in astrocytes are generated by two mechanisms whose impact changes along the astrocytic process

and in dependence on the volume fraction of the internal calcium store. Here, I propose a mathematical model which accounts for glutamate driven calcium signals in astrocytes shaped by both calcium release from internal stores as well as calcium entry from the extracellular space. Key element of the model is the consideration of the volume fraction of the internal calcium store, which allows a model parametrization for different positions along the astrocytic process between the soma and the synapse. With the help of the model I investigate the impact of the volume fraction of the internal calcium store on the calcium signal generation mediated by both mechanisms for different positions along the astrocytic process.

The results of this paper have been previously published (Oschmann et al., 2017b):

<sup>1</sup> <sup>2</sup>.

---

<sup>1</sup>The authors contribution to the original article are (FO: Franziska Oschmann, KM: Konstantin Mergenthaler, EJ: Evelyn Jungnickel, KO: Klaus Obermayer): Conceptualization: FO KM EJ KO. Funding acquisition: FO KM KO. Investigation: FO KM EJ. Methodology: FO KM EJ KO. Software: FO KM EJ. Writing – original draft: FO KO.

<sup>2</sup>The article is published under the Creative Commons Attribution License (CC BY 4.0).

Link: <https://doi.org/10.1371/journal.pcbi.1005377>

# Model

The objective of this first part of my thesis is the development of a computational model which accounts for (1) the generation of calcium ( $\text{Ca}^{2+}$ ) signals by  $\text{Ca}^{2+}$  release from internal stores as well as  $\text{Ca}^{2+}$  entry from the extracellular space together with (2) the varying weighting of these mechanisms in the different subcellular compartments of the astrocyte like the soma or an perisynaptic astrocytic process. For the purpose of addressing the former task, I extend a consisting model for  $\text{Ca}^{2+}$  release from internal stores (De Pittà et al., 2009) with  $\text{Ca}^{2+}$  entry from the extracellular space. I choose the model of De Pittà et al. (2009) as the basis of the model extension since it allows a direct stimulation of the  $\text{Ca}^{2+}$  dynamics via glutamate. In order to approach the latter problem, I include geometrical parameters into the model, which allow a model parametrization for different subcellular compartments.

In the following, first, I introduce the computational model for  $\text{Ca}^{2+}$  release from internal stores which serves as a basis for the model extension and, second, I extend this model with the mechanism for  $\text{Ca}^{2+}$  entry from the extracellular space as well as with the geometrical parameters which allow the investigation of  $\text{Ca}^{2+}$  signals in different subcellular compartments.

## 1 Computational model for $\text{Ca}^{2+}$ release from internal stores

### 1.1 Computational model for $\text{Ca}^{2+}$ release from internal stores by DePitta et al., 2009

De Pittà et al. (2009) developed a computational model for  $\text{Ca}^{2+}$  signal generation in astrocytes, which accounts for  $\text{Ca}^{2+}$  release from internal stores evoked by the stimulation with extracellular glutamate. The computational model describes the temporal changes of the intracellular concentrations of  $\text{Ca}^{2+}$  ( $\text{Ca}^{2+}_i$ ) and  $\text{IP}_3$  ( $\text{IP}_{3i}$ ) as well as the opening probability of receptor channels at the internal  $\text{Ca}^{2+}$  store (h).  $\text{Ca}^{2+}$  currents crossing the outer membrane are neglected, such that the model builds a closed system with a constant overall  $\text{Ca}^{2+}$  concentration in the intracellular space and the internal  $\text{Ca}^{2+}$  store.

Three  $\text{Ca}^{2+}$  currents determine the exchange of  $\text{Ca}^{2+}$  between the internal  $\text{Ca}^{2+}$  store and the intracellular space and by that shape the intracellular  $\text{Ca}^{2+}$  concentration. These  $\text{Ca}^{2+}$  currents crossing the membrane of the internal  $\text{Ca}^{2+}$  store are: the  $\text{IP}_3$  receptor current, the SERCA pump and a calcium leak current. While the  $\text{IP}_3$  receptor current is sensitive for the concentrations of  $\text{Ca}^{2+}$  and  $\text{IP}_3$ , the SERCA pump

and the  $\text{Ca}^{2+}$  leak current solely depend on the concentrations of  $\text{Ca}^{2+}$  in the internal store and in the intracellular space.

### 1.1.1 Dynamical variables

**Intracellular  $\text{Ca}^{2+}$  concentration** The intracellular  $\text{Ca}^{2+}$  concentration is defined by the sum of all  $\text{Ca}^{2+}$  currents, which contribute to a change of the intracellular  $\text{Ca}^{2+}$  concentration:

$$\frac{d\text{Ca}_i^{2+}}{dt} = I_{\text{IP}_3\text{R}} - I_{\text{Serca}} + I_{\text{CERleak}}. \quad (1.1)$$

These  $\text{Ca}^{2+}$  currents flowing between the internal  $\text{Ca}^{2+}$  store and the intracellular space are the SERCA pump ( $I_{\text{Serca}}$ ), a leak current ( $I_{\text{CERleak}}$ ) and the  $\text{IP}_3$  receptor current ( $I_{\text{IP}_3\text{R}}$ ). Detailed mathematical descriptions of the named currents can be found in Section 1.1.2.

**Intracellular  $\text{IP}_3$  concentration** The concentration change of the second messenger  $\text{IP}_3$  is determined by the production and degradation of  $\text{IP}_3$ . The production is mediated by the phosphoinositide-specific phospholipase C  $\beta$  ( $\text{PLC}\beta$ ) and the phosphoinositide-specific phospholipase C  $\delta$  ( $\text{PLC}\delta$ ). The degradation is mediated by the  $\text{IP}_3$  3-kinase ( $\text{IP}_3\text{-3K}$ ) and the inositol polyphosphate 5-phosphatase ( $\text{IP-5P}$ ).

$$\begin{aligned} \frac{d\text{IP}_{3i}}{dt} &= \text{prod}_{\text{PLC}\beta} + \text{prod}_{\text{PLC}\delta} - \text{degr}_{\text{IP}_3\text{-3K}} - \text{degr}_{\text{IP-5P}} \\ \text{prod}_{\text{PLC}\beta} &= v_\beta \cdot \frac{g^{0.7}}{g^{0.7} + (K_R + K_p \cdot \frac{\text{Ca}_i^{2+}}{\text{Ca}_i^{2+} + K_\pi})^{0.7}} \\ \text{prod}_{\text{PLC}\delta} &= \frac{v_\delta}{1 + \frac{\text{IP}_{3i}}{k_\delta}} \cdot \frac{\text{Ca}_i^{2+2}}{\text{Ca}_i^{2+2} + K_{\text{PLC}\delta}^2} \\ \text{degr}_{\text{IP}_3\text{-3K}} &= v_{3\text{K}} \cdot \frac{\text{Ca}_i^{2+4}}{\text{Ca}_i^{2+4} + K_D^4} \cdot \frac{\text{IP}_{3i}}{\text{IP}_{3i} + K_3} \\ \text{degr}_{\text{IP-5P}} &= r_{5p} \cdot \text{IP}_{3i} \end{aligned} \quad (1.2)$$

The production of  $\text{IP}_3$  by the phosphoinositide-specific phospholipase C ( $\text{PLC}$ )  $\beta$  is linked to the level of the extracellular glutamate concentration  $g$ . The maximal rate of  $\text{IP}_3$  production by  $\text{PLC}\beta$  is described by  $v_\beta$  and the glutamate affinity of the receptor is set by  $K_R$ .  $K_p$  is the  $\text{Ca}^{2+}$ -/ $\text{PLC}$ -dependent inhibition factor and  $K_\pi$  determines the  $\text{Ca}^{2+}$  affinity of  $\text{PLC}$ .

The maximal rate of  $\text{IP}_3$  production by  $\text{PLC}\delta$  is described by  $v_\delta$ . The activity of  $\text{PLC}\delta$  is inhibited according to the inhibition constant  $k_\delta$ . The  $\text{Ca}^{2+}$  affinity of  $\text{PLC}\delta$  is set by  $K_{\text{PLC}\delta}$ .

The maximal degradation rate of  $\text{IP}_3$  by  $\text{IP}_3\text{-3K}$  is determined by  $v_{3\text{K}}$ .  $K_D$  is the  $\text{Ca}^{2+}$  affinity of  $\text{IP}_3\text{-3K}$  and  $K_3$  is the  $\text{IP}_3$  affinity of  $\text{IP}_3\text{-3K}$ .

The degradation of  $\text{IP}_3$  through dephosphorylation by the inositol polyphosphate 5-phosphatase ( $\text{IP-5P}$ ) depends on the maximal rate,  $r_{5p}$ , of degradation by  $\text{IP-5P}$ .

Values of the model parameters can be found in Table 1.4.

**Activation of the IP<sub>3</sub> receptor channel** The activation of the IP<sub>3</sub> receptor channel is defined by h:

$$\frac{dh}{dt} = \frac{h_{\infty} - h}{\tau_h}, \quad (1.3)$$

with:  $h_{\infty} = \frac{Q_2}{Q_2 + Ca_i^{2+}}$ ,  $\tau_h = \frac{1}{a_2(Q_2 - Ca_i^{2+})}$  and  $Q_2 = d_2 \frac{IP_{3i} + d_1}{IP_{3i} + d_3}$ .

Here,  $a_2$  determines the IP<sub>3</sub> receptor binding rate for Ca<sup>2+</sup> inhibition. The inactivation dissociation constants of Ca<sup>2+</sup> and IP<sub>3</sub> are  $d_2$  and  $d_3$ , respectively.

**Ca<sup>2+</sup> concentration in the internal calcium store** The Ca<sup>2+</sup> concentration within the internal Ca<sup>2+</sup> store is defined by the change of the intracellular Ca<sup>2+</sup> concentration. Since De Pittà et al. (2009) neglected the flow of Ca<sup>2+</sup> through the outer membrane, the total free Ca<sup>2+</sup> (Ca<sup>2+</sup><sub>free</sub>) concentration remains constant and the Ca<sup>2+</sup> concentration in the internal Ca<sup>2+</sup> store is defined by:

$$Ca_{ER}^{2+} = (Ca_{free}^{2+} - Ca_i^{2+}) / ratio_{ER}. \quad (1.4)$$

Here,  $ratio_{ER}$  is the ratio between the volumes of the internal Ca<sup>2+</sup> store and the intracellular space.

### 1.1.2 Ca<sup>2+</sup> currents at the internal calcium store

**Calcium current through IP<sub>3</sub> receptor channels** IP<sub>3</sub> receptor channels mediate the Ca<sup>2+</sup>- and IP<sub>3</sub>-dependent Ca<sup>2+</sup> transport from the internal Ca<sup>2+</sup> store into the intracellular space. The channels are build up by four subunits. Each subunit consists of three binding sites: two Ca<sup>2+</sup> binding sites and one IP<sub>3</sub> binding site. The binding of Ca<sup>2+</sup> and IP<sub>3</sub> to these binding sites determines the activity of the receptor channel. While the binding of one Ca<sup>2+</sup> ion and one IP<sub>3</sub> molecule opens the channel, the binding of a second Ca<sup>2+</sup> ion to the third binding site closes the channel:

$$I_{IP_3R} = r_C \cdot \left( \frac{IP_{3i}}{IP_{3i} + d_1} \right)^3 \cdot \left( \frac{Ca_i^{2+}}{Ca_i^{2+} + d_5} \right)^3 \cdot h^3 \cdot (Ca_{ER}^{2+} - Ca_i^{2+}). \quad (1.5)$$

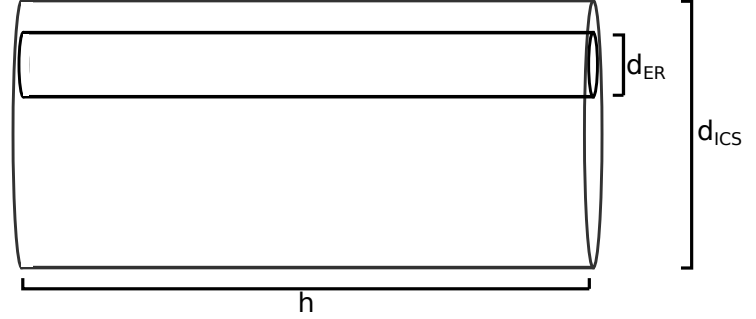
The IP<sub>3</sub> and Ca<sup>2+</sup> binding affinities of the channels' subunits are determined by  $d_1$  and  $d_5$ , respectively. The maximal channel permeability is  $r_C$ .

**SERCA pump** The SERCA pump mediates the Ca<sup>2+</sup> transport from the intracellular space into the internal Ca<sup>2+</sup> store:

$$I_{Serca} = v_{er} \cdot \frac{Ca_i^{2+2}}{Ca_i^{2+2} + K_{er}^2}. \quad (1.6)$$

Here, the maximal rate of Ca<sup>2+</sup> uptake by the SERCA pump is  $v_{ER}$  and  $K_{ER}$  determines the Ca<sup>2+</sup> affinity of the SERCA pump.

Figure 1.1: **Geometry of a single astrocytic compartment.** The geometry of a single astrocytic compartments is described by the diameter of the intracellular space ( $d_{ICS}$ ), the diameter of the internal  $Ca^{2+}$  store ( $d_{ER}$ ) and the length of a single compartment ( $h$ ).



**$Ca^{2+}$  leak from the ER** The unspecific  $Ca^{2+}$  leak current follows the  $Ca^{2+}$  concentration gradient between the internal  $Ca^{2+}$  store and the intracellular space multiplied with the maximal  $Ca^{2+}$  leakage from the internal  $Ca^{2+}$  store,  $r_L$ :

$$I_{C_{ER}leak} = r_L \cdot (Ca_{ER}^{2+} - Ca_i^{2+}). \quad (1.7)$$

## 1.2 Changes of the model by De Pittà et al. (2009)

With the intention to allow a model parametrization for different astrocytic subcellular compartments, I change the model developed by De Pittà et al. (2009) regarding the geometry of the considered astrocyte element as well as the computation of the  $Ca^{2+}$  concentration within the intracellular space and the internal  $Ca^{2+}$  store.

**Geometry** A single astrocyte consists of numerous subcellular compartments: one soma and several big branches which originate at the soma and split up into smaller branches (processes). These subcellular compartments differ in their surface area, their volume and in the volume fraction of the internal  $Ca^{2+}$  store. Thus, in order to apply these geometric parameters to the model, I first define the surface area, the volume and the volume fraction of the internal  $Ca^{2+}$  store for the different subcellular compartments.

The outer shell of a single compartment of an extended astrocyte can be approximated by a cylinder. A second cylinder of same length and smaller diameter lying within this compartment then defines the shape and the position of the internal  $Ca^{2+}$  store (see Figure 1.1). Since the diffusion to neighboring compartments is neglected the surface area of the compartment is defined by the shell surface of the cylinder. The surface area ( $A$ ) and the volume ( $Vol$ ) of the astrocytic compartment are described by:

$$A = d_{ICS} \cdot \pi \cdot h_{ICS},$$

$$Vol = \left(\frac{d_{ICS}}{2}\right)^2 \cdot \pi \cdot h_{ICS}.$$

Here,  $d_{ICS}$  and  $h_{ICS}$  are the diameter and the length of the intracellular space of the astrocytic compartment, respectively.

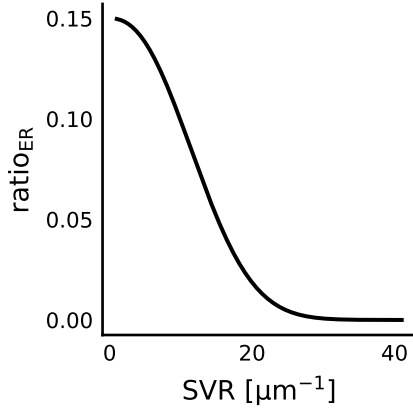


Figure 1.2: **The volume ratio of the endoplasmic reticulum (ER) as a function of the surface volume ratio (SVR).** The data has been adapted from Patrushev et al. (2013). Figure and caption adapted from (Oschmann et al., 2017b).

The volume of the cylinder describing the internal  $\text{Ca}^{2+}$  store ( $\text{Vol}_{ER}$ ) is defined by the multiplication of the volume of the astrocytic compartment with the volume fraction of the internal  $\text{Ca}^{2+}$  store ( $\text{ratio}_{ER}$ ):

$$\text{Vol}_{ER} = \text{Vol} \cdot \text{ratio}_{ER}. \quad (1.8)$$

The volume of the intracellular space ( $\text{Vol}_{ICS}$ ) results from the difference between the volumes of the astrocytic compartment and the internal  $\text{Ca}^{2+}$  store:

$$\text{Vol}_{ICS} = \text{Vol} - \text{Vol} \cdot \text{ratio}_{ER} = \text{Vol} \cdot (1 - \text{ratio}_{ER}). \quad (1.9)$$

Since the cylinder describing the internal  $\text{Ca}^{2+}$  store only differs in its radius compared to the cylinder describing the whole astrocytic compartment, the surface area ( $A_{ER}$ ) of the internal  $\text{Ca}^{2+}$  store is defined as follows:

$$A_{ER} = A \cdot \sqrt{\text{ratio}_{ER}}. \quad (1.10)$$

Along the astrocytic process variations of the surface volume ratio ( $\text{SVR} = \frac{A}{\text{Vol}}$ ) and also the volume fraction of the internal  $\text{Ca}^{2+}$  store ( $\text{ratio}_{ER}$ ) were observed (Patrushev et al., 2013) (see Figure 1.2). Moreover, a dependency between both parameters has been reported, which can be quantified by:

$$\text{ratio}_{ER} = 0.15 \cdot e^{-(0.002\mu\text{m} \cdot \text{SVR})^{2.32}}. \quad (1.11)$$

In order to relate the dynamics of the intracellular  $\text{Ca}^{2+}$  concentration to the surface area and the volume of an astrocytic compartment as well as the volume fraction of internal  $\text{Ca}^{2+}$  store, I define the intracellular  $\text{Ca}^{2+}$  concentration by the sum of all currents contributing to a change of the intracellular  $\text{Ca}^{2+}$  concentration multiplied with the area of the internal  $\text{Ca}^{2+}$  store ( $A_{ER}$ ) and divided by the volume of the intracellular space ( $\text{Vol}_{ICS}$ ) and the Faraday constant ( $F$ ):

$$\frac{d\text{Ca}^{2+}_i}{dt} = \frac{A_{ER}}{F \cdot \text{Vol}_{ICS}} \cdot (I_{IP3R} - I_{Serca} + I_{C_{ER}leak}). \quad (1.12)$$

For the purpose of maintaining the unit of the differential equation of the intracellular  $\text{Ca}^{2+}$  concentration, I adapt the unit of the  $\text{Ca}^{2+}$  currents. De Pittà et al. (2009) defined the unit of the  $\text{Ca}^{2+}$  currents to be  $\frac{\mu\text{M}}{\text{sec}}$ . The changed differential equation requires currents of the unit  $\frac{\text{A}}{\text{m}^2}$ . Therefore, I multiply the rates of  $I_{\text{IP}_3\text{R}}$ ,  $I_{\text{Serca}}$  and  $I_{\text{CERleak}}$  with  $\frac{F \cdot \text{Vol}}{A_{\text{ER}}}$ .

**$\text{Ca}^{2+}$  concentration in the internal  $\text{Ca}^{2+}$  store.** In order to relate the  $\text{Ca}^{2+}$  concentration in the internal  $\text{Ca}^{2+}$  store to the surface area and the volume of the internal  $\text{Ca}^{2+}$  store, the change of this concentration was defined by the sum of all  $\text{Ca}^{2+}$  currents crossing the membrane of the internal  $\text{Ca}^{2+}$  store and divided by the volume of the internal  $\text{Ca}^{2+}$  store ( $\text{Vol}_{\text{ER}}$ ) multiplied with the Faraday constant (F):

$$\frac{d\text{Ca}_{\text{ER}}^{2+}}{dt} = \frac{A_{\text{ER}}}{F \cdot \text{Vol}_{\text{ER}}} \cdot (-I_{\text{IP}_3\text{R}} + I_{\text{Serca}} - I_{\text{CERleak}}). \quad (1.13)$$

## 2 Extension of the model of De Pittà et al. (2009) and introduction of $\text{Na}^+$ , $\text{K}^+$ and V dynamics

In order to account for a mechanism for  $\text{Ca}^{2+}$  entry from the extracellular space, I extend the model for  $\text{Ca}^{2+}$  release from internal stores by De Pittà et al. (2009) with a mechanisms for  $\text{Ca}^{2+}$  entry from the extracellular space. The mechanism for  $\text{Ca}^{2+}$  entry is performed by the interaction of the glutamate transporter (GluT), the sodium-potassium pump (NKA), the sodium-calcium exchanger (NCX) and a sodium ( $\text{Na}^+$ ) as well as a potassium ( $\text{K}^+$ ) leak current (see Figure 1.3). The glutamate transporter mediates the transport of glutamate from the extracellular space into the intracellular space. Together with each glutamate molecule three  $\text{Na}^+$  ions are transported into the astrocyte and one  $\text{K}^+$  ion out of the astrocyte. The elevated  $\text{Na}^+$  concentration within the astrocyte activates the  $\text{Na}^+$ - $\text{Ca}^{2+}$  exchanger in the reverse mode and gives rise to  $\text{Ca}^{2+}$  entry from the extracellular space. The  $\text{Na}^+$ - $\text{K}^+$  pump promotes the transport of three  $\text{Na}^+$  ions out of the astrocyte and two  $\text{K}^+$  ions into the astrocyte. By that the pump produces the concentration gradient which is necessary for the glutamate uptake by astrocytes mediated by the glutamate transporter. Unspecific flows of  $\text{Na}^+$  and  $\text{K}^+$  through the membrane are covered by a  $\text{Na}^+$  and a  $\text{K}^+$  leak current.

### 2.1 Dynamics of the ion concentrations and the membrane voltage

**Dynamics of ion concentrations** In general the change of the ion concentration is given by the following equation:

$$\frac{dion}{dt} = \frac{A}{F \cdot \text{Vol}} \cdot \sum I_{ion}. \quad (1.14)$$

It depends on the sum of all ionic currents carrying the respective ion ( $\sum I_{ion}$ ) with respect to the number of carried ions, multiplied with the area (A), the ionic currents are flowing through, and divided by the volume (Vol) of the space the ions

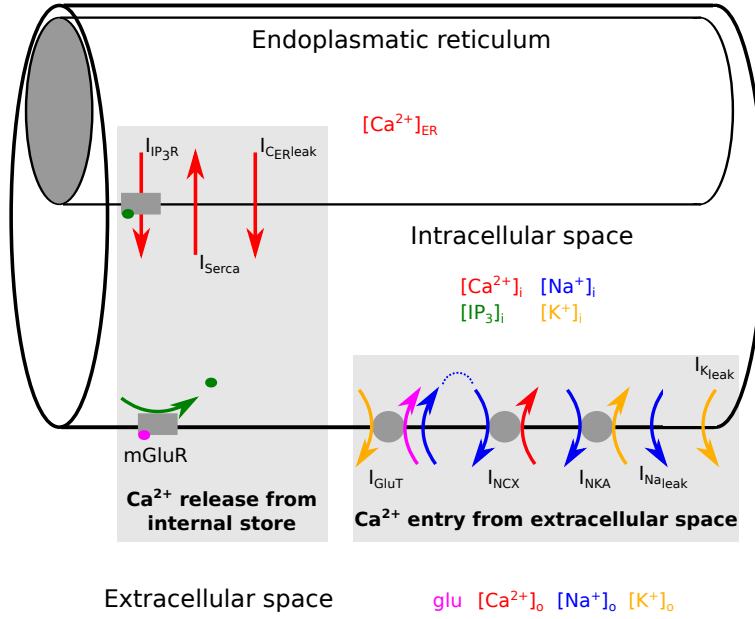


Figure 1.3: **Ca<sup>2+</sup> signal generation in astrocytes.** Astrocytic compartments consist of three parts: the intracellular space, the internal Ca<sup>2+</sup> store (endoplasmic reticulum) and the extracellular space. Ca<sup>2+</sup> signals in the intracellular space are generated by two different pathways: Ca<sup>2+</sup> release from internal stores and Ca<sup>2+</sup> entry from the extracellular space. The former mechanism is driven by the glutamate dependent production of IP<sub>3</sub>, which then evokes IP<sub>3</sub> and Ca<sup>2+</sup> dependent exchange of Ca<sup>2+</sup> between the intracellular space and the internal Ca<sup>2+</sup> store. The other mechanism describes the glutamate transporter driven transport of Ca<sup>2+</sup> between the extracellular and the intracellular space. Figure and caption adapted from (Oschmann et al., 2017b).

are located in as well as by the Faraday constant.

The change of the intracellular Ca<sup>2+</sup> concentration is determined by currents crossing either the membrane of the internal Ca<sup>2+</sup> store ( $I_{IP_3R}$ ,  $I_{SERCA}$ ,  $I_{CERleak}$ ) or of the outer cell membrane ( $I_{NCX}$ ). Consequently, I change the differential equation of the intracellular Ca<sup>2+</sup> concentration to:

$$\frac{dCa^{2+}_i}{dt} = \frac{A}{F \cdot Vol_{ICS}} \cdot I_{NCX} + \frac{A_{ER}}{F \cdot Vol_{ICS}} \cdot (I_{IP_3R} - I_{SERCA} + I_{CERleak}). \quad (1.15)$$

$A$  and  $A_{ER}$  denote the area of the outer cell membrane and of the internal Ca<sup>2+</sup> store, respectively. The volume of the intracellular space is defined by  $Vol_{ICS}$ .

The change of the Ca<sup>2+</sup> concentration in the internal Ca<sup>2+</sup> store is solely determined by currents crossing the membrane of the internal Ca<sup>2+</sup> store:

$$\frac{dCa^{2+}_{ER}}{dt} = \frac{A_{ER}}{F \cdot Vol_{ER}} \cdot (-I_{IP_3R} + I_{SERCA} - I_{CERleak}),$$

here  $A_{ER}$  and  $Vol_{ER}$  describe the area and the volume of the internal Ca<sup>2+</sup> store, respectively.

The change of the intracellular  $\text{Na}^+$  concentration is determined by all  $\text{Na}^+$  currents crossing the outer membrane:

$$\frac{d\text{Na}_i^+}{dt} = \frac{A}{F \cdot \text{Vol}_{ICS}} \cdot (3I_{\text{GluT}} - 3I_{\text{NKA}} - 3I_{\text{NCX}} - I_{\text{Na}_{leak}}). \quad (1.16)$$

The change of the intracellular  $\text{K}^+$  concentrations is described in the same manner:

$$\frac{d\text{K}_i^+}{dt} = \frac{A}{F \cdot \text{Vol}_{ICS}} \cdot (-I_{\text{GluT}} + 2I_{\text{NKA}} - I_{\text{K}_{leak}}). \quad (1.17)$$

**Dynamics of the membrane voltage** The change of the membrane voltage  $V$  is determined by:

$$\frac{dV}{dt} = -\frac{1}{C_m} (-2I_{\text{IP}_3\text{R}} + 2I_{\text{Serca}} - 2I_{\text{CER}_{leak}} + I_{\text{NCX}} - 2I_{\text{GluT}} + I_{\text{NKA}} + I_{\text{Na}_{leak}} + I_{\text{K}_{leak}}). \quad (1.18)$$

The right hand side of the equation consists of the sum of all ionic currents crossing either the membrane of the internal  $\text{Ca}^{2+}$  store or the outer cell membrane with the consideration of carried charges per ion (see Figure 1.3). Here, it is important to realize that the transport of  $\text{Na}^+$  and  $\text{K}^+$  mediated by the glutamate transporter lead to a net transfer of two positive charges per cycle across the membrane.  $C_m$  denotes the membrane capacitance.

**Extracellular ion concentrations** In order to set the overall concentrations of  $\text{Ca}^{2+}$ ,  $\text{Na}^+$  and  $\text{K}^+$  to constant levels, I define the extracellular concentrations by:

$$\text{Ca}_o^{2+} - \text{Ca}_{orest}^{2+} = \text{Ca}_{irest}^{2+} + \text{Ca}_{ERrest}^{2+} - \text{Ca}_i^{2+} - \text{Ca}_{ER}^{2+}, \quad (1.19)$$

$$\text{Na}_o^+ - \text{Na}_{orest}^+ = \text{Na}_{irest}^+ - \text{Na}_i^+, \quad (1.20)$$

$$\text{K}_o^+ - \text{K}_{orest}^+ = \text{K}_{irest}^+ - \text{K}_i^+. \quad (1.21)$$

The extracellular concentrations were defined as a function of the intracellular concentrations. This definition of the extracellular concentration was based on the assumption that the volume of the intracellular and the extracellular space of an astrocytic compartment are the same as well as that the overall concentration in the intracellular and the extracellular space of an astrocytic compartment stays constant. Values of the model parameters can be found in Table 3.3.

### Transmembrane Transporters

**Glutamate Transporter** The transport of glutamate mediated by the glutamate transporter (GluT) is determined by:

$$I_{\text{GluT}} = I_{\text{GluT}_{max}} \cdot \frac{\text{K}_i^+}{\text{K}_i^+ + K_{\text{GluT}_{mK}}} \cdot \frac{\text{Na}_o^{+3}}{\text{Na}_o^{+3} + K_{\text{GluT}_{mN}}^3} \cdot \frac{g}{g + K_{\text{GluT}_{mg}}}. \quad (1.22)$$

Here,  $I_{\text{GluTmax}}$  is the maximal transport current of the glutamate transporter. The half saturation constants of  $\text{Na}^+$ ,  $\text{K}^+$  and glutamate are given by  $K_{\text{GluTmN}}$ ,  $K_{\text{GluTmK}}$  and  $K_{\text{GluTmg}}$ , respectively. The half saturation constant of  $\text{K}^+$  is not known from experimental results. Since the half saturation constant of  $\text{Na}^+$  is close to its intracellular resting concentration, I define the half saturation constant of  $\text{K}^+$  in the same manner.

The transport of glutamate is coupled to the cotransport of three  $\text{Na}^+$  ions and one  $\text{H}^+$  ion and the countertransport of one  $\text{K}^+$  ion (Tzingounis and Wadiche, 2007; Kanner and Bendahan, 1982). Additionally, glutamate transporters enable the movement of anions across the membrane, which is not coupled to the transported of glutamate (Wadiche et al., 1995). However, since the uncoupled anion current has only a little effect on the transport of glutamate, it is neglected.

The intracellular glutamate concentration does not affect the glutamate uptake by the glutamate transporter. Therefore, I do not consider the intracellular glutamate concentration in the model.

Values of the model parameters can be found in Table 1.5.

**$\text{Na}^+$ - $\text{K}^+$ -ATPase** The transport of  $\text{Na}^+$  and  $\text{K}^+$  against its concentration gradient is performed by the  $\text{Na}^+$ - $\text{K}^+$ -ATPase (NKA). Here, I apply the mathematical expression of Luo and Rudy (1994) in a simplified form:

$$I_{\text{NKA}} = I_{\text{NKA}_{\text{max}}} \cdot \frac{\text{Na}_i^{+1.5}}{\text{Na}_i^{+1.5} + K_{\text{NKA}_{\text{mN}}}^{1.5}} \cdot \frac{K_o^+}{K_o^+ + K_{\text{NKA}_{\text{mK}}}}. \quad (1.23)$$

$I_{\text{NKA}_{\text{max}}}$  defines the maximal pumping activity of the  $\text{Na}^+$ - $\text{K}^+$  pump.  $K_{\text{NKA}_{\text{mN}}}$  and  $K_{\text{NKA}_{\text{mK}}}$  determine the half saturation constants of  $\text{Na}^+$  and  $\text{K}^+$ , respectively.

The  $\text{Na}^+$ - $\text{K}^+$ -ATPase transports three  $\text{Na}^+$  ions out of the cell and two  $\text{K}^+$  ions into the cell. Its pumping activity depends on the intracellular  $\text{Na}^+$  concentration and the extracellular  $\text{K}^+$  concentration.

Values of the model parameters can be found in Table 1.5.

**$\text{Na}^+$ - $\text{Ca}^{2+}$  exchanger** The  $\text{Na}^+$ - $\text{Ca}^{2+}$  exchanger (NCX) mediates the exchange of three  $\text{Na}^+$  ions with one  $\text{Ca}^{2+}$  ion. Here, I apply the mathematical description of the  $\text{Na}^+$ - $\text{Ca}^{2+}$  exchanger developed by Luo and Rudy (1994):

$$I_{\text{NCX}} = I_{\text{NCX}_{\text{max}}} \cdot \frac{\text{Na}_o^{+3}}{K_{\text{NCX}_{\text{mN}}}^3 + \text{Na}_o^{+3}} \cdot \frac{\text{Ca}_o^{2+}}{K_{\text{NCX}_{\text{mC}}} + \text{Ca}_o^{2+}} \cdot \frac{\frac{\text{Na}_i^{+3}}{\text{Na}_i^{+3}} \cdot \exp(\eta \cdot \frac{V \cdot F}{R \cdot T}) - \frac{\text{Ca}_i^{2+}}{\text{Ca}_o^{2+}} \cdot \exp((\eta - 1) \cdot \frac{V \cdot F}{R \cdot T})}{1 + k_{\text{sat}} \cdot \exp((\eta - 1) \cdot \frac{V \cdot F}{R \cdot T})}. \quad (1.24)$$

$I_{\text{NCX}_{\text{max}}}$  is the maximal pump current of the exchanger. The half saturation constants for  $\text{Na}^+$  and  $\text{Ca}^{2+}$  are given by  $K_{\text{NCX}_{\text{mN}}}$  and  $K_{\text{NCX}_{\text{mC}}}$ , respectively. The position of the energy barrier  $\eta$  controls the voltage dependence.  $k_{\text{sat}}$  is a saturation factor ensuring saturation at large negative potentials.

The exchanger works either in the forward or in the reverse mode. In the forward mode  $\text{Ca}^{2+}$  is transported out of the astrocyte and  $\text{Na}^+$  is transported into the astrocyte. The reverse mode works the other way round. A switch into the reverse mode is induced by an increased intracellular  $\text{Na}^+$  concentration (Blaustein and Santiago, 1977). The current strength of the  $\text{Na}^+$ - $\text{Ca}^{2+}$  exchanger depends on the intra- and extracellular  $\text{Na}^+$  and  $\text{Ca}^{2+}$  concentrations.

Values of the model parameters can be found in Table 1.5.

**Leak currents** The unspecific flow of  $\text{Na}^+$  and  $\text{K}^+$  ions across the membrane is given by the leak currents:

$$I_{\text{Na}_{leak}} = g_{\text{Na}_{leak}} \cdot (V - E_{\text{Na}}), \quad (1.25)$$

$$I_{\text{K}_{leak}} = g_{\text{K}_{leak}} \cdot (V - E_{\text{K}}). \quad (1.26)$$

Here,  $g_{\text{Na}_{leak}}$  and  $g_{\text{K}_{leak}}$  are the corresponding conductances of the  $\text{Na}^+$  and  $\text{K}^+$  currents. The Nernst potentials of  $\text{Na}^+$  and  $\text{K}^+$  are given by  $E_{\text{Na}} = \frac{R \cdot T}{F} \log\left(\frac{\text{Na}_o^+}{\text{Na}_i^+}\right)$  and  $E_{\text{K}} = \frac{R \cdot T}{F} \log\left(\frac{\text{K}_o^+}{\text{K}_i^+}\right)$ . Here,  $R$  is the gas constant,  $T$  is the temperature and  $F$  is the Faraday constant.

Values of the model parameters can be found in Table 1.5.

### 3 Neuronal stimulation of the astrocyte compartment

The release of neurotransmitters from an activated nearby synapse is calculated using the Tsodyks and Makram model (Tsodyks and Markram, 1997; Fuhrmann et al., 2002) in its for glutamate release adapted form published by Wallach et al. (2014):

$$\begin{aligned} r(t) &= x(t) \cdot y(t), \\ \frac{dx}{dt} &= \frac{(1 - x(t))}{\tau_{rec}} - x(t) \cdot y(t) \cdot s(t), \\ \frac{dy}{dt} &= -\frac{y(t)}{\tau_{facil}} + U_0(1 - y(t)) \cdot s(t), \\ \frac{dg}{dt} &= -\frac{g}{\tau_{clear}} + \rho_C G_T \cdot r(t). \end{aligned}$$

The ratio of glutamate released during each spike is given by the product  $r(t)$  of the fraction of recovered resources ( $x$ ) and active resources ( $y$ ). During each spike a fraction of active synaptic resources ( $y$ ) is released into the synaptic cleft and increases with a step increase determined by  $U_0$ . Between spikes the fraction of these active synaptic resources ( $y$ ) decays back to a baseline level with time constant  $\tau_{facil}$ . At the same time the fraction of recovered resources ( $x$ ) recovers to 1 with the time constant  $\tau_{rec}$ . The change of the glutamate concentration in the synaptic cleft

is determined by the product of the total glutamate content of readily releasable vesicles ( $G_T$ ) and of the volume ratio between the synaptic vesicles and the synaptic cleft ( $\rho_C$ ). Glutamate is removed from the synaptic cleft with the time constant  $\tau_{clear}$ .

Values of the model parameters can be found in Table 1.6.

## 4 Model parameter values

I determine the initial values of the intracellular  $IP_3$  concentration, the fraction  $h$  of active  $IP_3$  receptor channels, and the  $Ca^{2+}$  in the internal store as well as the model parameters  $g_{Na_{leak}}$  and  $g_{K_{leak}}$  in the same manner. For example, since the model parameters for the production and degradation of  $IP_3$  and the intracellular resting concentration of  $Ca^{2+}$  are known from literature, the zero of  $\frac{dIP_{3i}}{dt}$  reveals the initial concentration of  $IP_3$ . In the same way I calculate the initial ratio of activated  $IP_3$  receptor channels,  $h$ , and the initial concentration of the  $Ca^{2+}$  concentration in the internal  $Ca^{2+}$  store. In this way a stable resting state is ensured. The model parameter  $g_{Na_{leak}}$  is calculated by setting  $\frac{dNa_i^+}{dt}$  equal to zero and solving the equation for  $g_{Na_{leak}}$ . The model parameter  $g_{K_{leak}}$  is calculated the same way by setting  $\frac{dK_i^+}{dt}$  equal to zero.

Table 1.1: Initial values.

Initial values of the ion concentrations, the membrane voltage,  $IP_3$  and the fraction of the activated  $IP_3$  receptor channels,  $h$ . The calculation of  $Ca^{2+}_{ER}$ ,  $IP_{3i}$  and  $h$  is explained above.

Parameter	Value	Source
$Ca_i^{2+}$	0.073 $\mu$ M	Reyes et al. (2012)
$Ca_{ER}^{2+}$	19 $\mu$ M	see text
$Ca_o^{2+}$	1800 $\mu$ M	Luo and Rudy (1994)
$Na_i^+$	15 mM	Østby et al. (2009)
$Na_o^+$	145 mM	Østby et al. (2009)
$K_i^+$	100 mM	Østby et al. (2009)
$K_o^+$	3 mM	Østby et al. (2009)
V	-85 mV	McKhann et al. (1997)
$IP_{3i}$	0.15659 $\mu$ M	see text
h	0.7892	see text

Table 1.2: Model parameters for the dynamics of  $h$ .

Parameter	Value	Source
$a_2$	0.2 $\frac{1}{s}$	De Pittà et al. (2009)
$d_2$	1.049 $\mu$ M	De Pittà et al. (2009)
$d_3$	0.9434 $\mu$ M	De Pittà et al. (2009)

Table 1.3: Model parameters for the  $\text{Ca}^{2+}$  currents at the endoplasmatic reticulum.

Parameter	Value	Source
<b>IP<sub>3</sub> receptor channel</b>		
$r_C$	$6 \frac{1}{s}$	De Pittà et al. (2009)
$d_1$	$0.13 \mu\text{M}$	De Pittà et al. (2009)
$d_5$	$0.08234 \mu\text{M}$	De Pittà et al. (2009)
<b>SERCA pump</b>		
$v_{ER}$	$4 \frac{\mu\text{M}}{s}$	(Falcke et al., 1999; Ullah et al., 2006)
$K_{ER}$	$0.1 \mu\text{M}$	De Pittà et al. (2009)
<b>Ca<sup>2+</sup> leak</b>		
$r_L$	$0.11 \frac{1}{s}$	De Pittà et al. (2009)

Table 1.4: Model parameters for the production and degradation of IP<sub>3</sub>.

IP<sub>3</sub> production is mediated by PLC $\beta$  and PLC $\delta$  and IP<sub>3</sub> degradation is mediated by IP<sub>3</sub> - 3K and IP - 5P.

Parameter	Value	Source
<b>IP<sub>3</sub> production by PLC<math>\beta</math></b>		
$v_\beta$	$0.05 \frac{\mu\text{M}}{s}$	De Pittà et al. (2009)
$K_R$	$1.3 \mu\text{M}$	De Pittà et al. (2009)
$K_P$	$10 \mu\text{M}$	De Pittà et al. (2009)
$K_\pi$	$0.6 \mu\text{M}$	De Pittà et al. (2009)
<b>IP<sub>3</sub> production by PLC<math>\delta</math></b>		
$v_\delta$	$0.02 \frac{\mu\text{M}}{s}$	De Pittà et al. (2009)
$k_\delta$	$1.5 \mu\text{M}$	De Pittà et al. (2009)
$K_{PLC\delta}$	$0.1 \mu\text{M}$	De Pittà et al. (2009)
<b>IP<sub>3</sub> degradation by IP<sub>3</sub> - 3K</b>		
$v_{3K}$	$2 \frac{\mu\text{M}}{s}$	De Pittà et al. (2009)
$K_D$	$0.7 \mu\text{M}$	De Pittà et al. (2009)
$K_3$	$1 \mu\text{M}$	De Pittà et al. (2009)
<b>IP<sub>3</sub> degradation by IP - 5P</b>		
$r_{5P}$	$0.04 \frac{1}{s}$	De Pittà et al. (2009)

Table 1.5: **Model parameters for the membrane currents.**

The Glutamate Transporter, the Na<sup>+</sup>/K<sup>+</sup> ATPase, the Na<sup>+</sup>/Ca<sup>2+</sup> exchanger and the leak currents for Na<sup>+</sup> and K<sup>+</sup>. The determination of the model parameters  $I_{\text{GluTmax}}$  and  $I_{\text{NKAmx}}$  can be found in the Results Section. The definition of the model parameter  $K_{\text{GluTmK}}$  can be found in the Model Section. The calculation of  $g_{\text{NaLeak}}$  and  $g_{\text{KLeak}}$  is explained above.

Parameter	Value	Source
<b>Glutamate Transporter</b>		
$I_{\text{GluTmax}}$	$0.75 \frac{\text{pA}}{\mu\text{m}^2}$	see text
$K_{\text{GluTmN}}$	15 mM	Horak et al. (1990)
$K_{\text{GluTmK}}$	5 mM	see text
$K_{\text{GluTmg}}$	34 $\mu\text{M}$	Horak et al. (1990)
<b>Na<sup>+</sup>/K<sup>+</sup> ATPase</b>		
$I_{\text{NKAmx}}$	$1.52 \frac{\text{pA}}{\mu\text{m}^2}$	see text
$K_{\text{NKAmN}}$	10 mM	Luo and Rudy (1994)
$K_{\text{NKAmK}}$	1.5 mM	Luo and Rudy (1994)
<b>Na<sup>+</sup>/Ca<sup>2+</sup> exchanger</b>		
$I_{\text{NCXmax}}$	$0.1 \frac{\text{pA}}{\mu\text{m}^2}$	see text
$K_{\text{NCXmN}}$	87500 $\mu\text{M}$	Luo and Rudy (1994)
$K_{\text{NCXmC}}$	1380 $\mu\text{M}$	Luo and Rudy (1994)
$k_{\text{sat}}$	0.1	Luo and Rudy (1994)
$\eta$	0.35	Luo and Rudy (1994)
<b>Leak Currents</b>		
$g_{\text{NaLeak}}$	$13.34 \frac{\text{S}}{\text{m}^2}$	see text
$g_{\text{KLeak}}$	$162.46 \frac{\text{S}}{\text{m}^2}$	see text

Table 1.6: **Parameters for the Tsodyks and Markram model.**

Parameter	Value	Source
$\tau_{\text{facil}}$	$2 \text{ s}^{-1}$	Wallach et al. (2014)
$\tau_{\text{rec}}$	$1 \text{ s}^{-1}$	Wallach et al. (2014)
$\tau_{\text{clear}}$	$60 \text{ s}^{-1}$	Wallach et al. (2014)
$U_0$	0.25	Wallach et al. (2014)
$\rho_C$	$6.5 \cdot 10^{-4}$	Wallach et al. (2014)

Table 1.7: **Physical constants used in the model.**

Parameter	Value	Description
$F$	$96\,500 \frac{\text{C}}{\text{mol}}$	Faraday constant
$R$	$8.314 \frac{\text{J}}{\text{mol}\cdot\text{K}}$	Gas constant
$T$	311 K	Temperature

## 5 Computational methods

All simulations were performed with Python 2.7 using the packages Brian (Goodman and Brette, 2008), NumPy and Matplotlib. The Brian Simulator used the Euler integration as numerical integration method for the non-linear differential equations with time step  $dt=1\text{ms}$ .



# Results

## 1 $\text{Ca}^{2+}$ release from the internal $\text{Ca}^{2+}$ store along the astrocytic process

As a first step I analyze the  $\text{Ca}^{2+}$  release from the internal  $\text{Ca}^{2+}$  store and its dependence on the considered position along the astrocytic process. A parametrization for different positions along the astrocytic process is achieved by a variation of the volume fraction of the internal  $\text{Ca}^{2+}$  store ( $\text{ratio}_{\text{ER}}$ ) together with the surface volume ratio (SVR) (see Model Section 1). The object of this first experiment is to investigate solely the  $\text{Ca}^{2+}$  signal generation evoked by  $\text{Ca}^{2+}$  release (see Figure 1.4). For this purpose, I set all currents related to the  $\text{Ca}^{2+}$  entry from the extracellular space to zero.

The decrease of the volume fraction of the internal  $\text{Ca}^{2+}$  store ( $\text{ratio}_{\text{ER}}$ ) causes a bifurcation of the dynamical system and thus a transition from oscillatory to non-oscillation behavior (see Figure 1.4 b). Astrocytic compartments with a high volume fraction of the internal  $\text{Ca}^{2+}$  store ( $\text{ratio}_{\text{ER}} \geq 0.6$ ) show long-lasting  $\text{Ca}^{2+}$  oscillations. In this parameter range a reduction of  $\text{ratio}_{\text{ER}}$  causes a decrease of the oscillation amplitude and an increase of the oscillation frequency (see Figure 1.4 c). A further decrease of the volume fraction of the internal  $\text{Ca}^{2+}$  store ( $\text{ratio}_{\text{ER}} < 0.6$ ) results in a bifurcation. Volume fractions below 0.6 do not allow the generation of intracellular  $\text{Ca}^{2+}$  oscillations. Instead the  $\text{Ca}^{2+}$  concentration increases to a steady level. However, if the astrocytic compartment is devoid of the internal  $\text{Ca}^{2+}$  store ( $\text{ratio}_{\text{ER}} = 0$ ), the  $\text{Ca}^{2+}$  concentration remains unchanged.

In summary, the consideration of  $\text{Ca}^{2+}$  release from internal stores in isolation produces  $\text{Ca}^{2+}$  oscillations in astrocytic regions with a large volume fraction of the internal  $\text{Ca}^{2+}$  store.  $\text{Ca}^{2+}$  elevations in astrocytic compartments devoid of the internal  $\text{Ca}^{2+}$  store, however, can not be explained by this mechanisms.

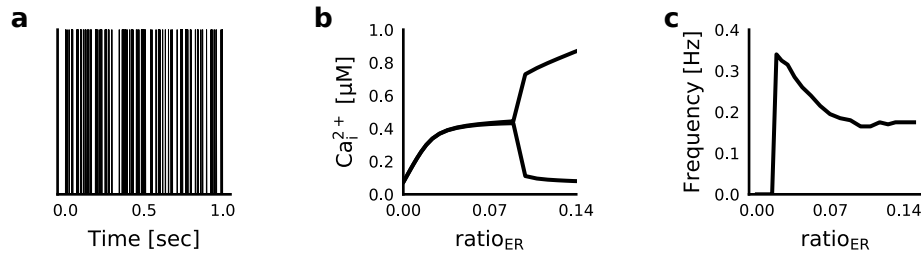


Figure 1.4: **Dynamics of the  $\text{Ca}^{2+}$  concentration in the intracellular compartment during synaptic activation.** **a** Sample stimulus (spikes). The astrocytic compartment is stimulated for 200 seconds with a Poisson spike train of 100 Hz. The corresponding glutamate concentration in the extracellular compartment as a function of time is calculated using the Tsodyks-Markram model. **b**  $\text{Ca}^{2+}_i$  for different values of the volume ratio ( $\text{ratio}_{\text{ER}}$ ) between the internal  $\text{Ca}^{2+}$  store and the intracellular compartments. The upper and lower lines for  $\text{ratio}_{\text{ER}} > 0.06$  denote the average height of peaks and troughs of the emerging  $\text{Ca}^{2+}$  oscillations. For  $\text{ratio}_{\text{ER}} \leq 0.06$  no  $\text{Ca}^{2+}$  oscillations are present and the line denotes the average concentration of  $\text{Ca}^{2+}$  over the stimulation period. **c** Frequency of  $\text{Ca}^{2+}$  oscillations as a function of  $\text{ratio}_{\text{ER}}$ . Figure and caption adapted from (Oschmann et al., 2017b).

## 2 $\text{Ca}^{2+}$ entry from the extracellular space

As a next step, I analyze the  $\text{Ca}^{2+}$  entry from the extracellular space and its effect on the  $\text{Ca}^{2+}$  release from internal stores. The  $\text{Ca}^{2+}$  entry from the extracellular space is mediated by the  $\text{Na}^+$ - $\text{Ca}^{2+}$  exchanger (NCX). The NCX can operate in the forward as well as in the reverse mode. While in the forward mode  $\text{Ca}^{2+}$  is transported out of the astrocyte and  $\text{Na}^+$  into the astrocyte, the reverse mode operates the other way round. A switch between these two modes is evoked by changes in the concentrations of  $\text{Ca}^{2+}$  and  $\text{Na}^+$ . For example an accumulation of intracellular  $\text{Na}^+$  leads to a switch into the reverse mode and thus to  $\text{Ca}^{2+}$  entry into the astrocyte. Therefore, the intracellular  $\text{Na}^+$  dynamic is crucial for the transport of  $\text{Ca}^{2+}$  into the astrocyte. The intracellular  $\text{Na}^+$  dynamic is determined by the glutamate transporter (GluT), the  $\text{Na}^+$ - $\text{K}^+$  pump (NKA) as well as the  $\text{Na}^+$ - $\text{Ca}^{2+}$  exchanger (NCX). Thus, as a first experiment I analyze the glutamate dependent increase of the intracellular  $\text{Na}^+$  concentration in dependence on the above named currents and compare the results to experimental data. Once I find a weighting of the  $\text{Na}^+$  currents reflecting the experimental data, I investigate the  $\text{Ca}^{2+}$  entry into the astrocyte itself and its effect on  $\text{Ca}^{2+}$  release from internal stores.

### 2.1 $\text{Na}^+$ entry into the astrocyte

In order to study the glutamate dependent increase of the intracellular  $\text{Na}^+$  concentration, I vary the maximal pump currents of the considered  $\text{Na}^+$  currents ( $I_{\text{GluT}_{\text{max}}}$ ,  $I_{\text{NKA}_{\text{max}}}$ ,  $I_{\text{NCX}_{\text{max}}}$ ) and analyze the effect of those variations on the intracellular  $\text{Na}^+$  concentration.

While the maximal pump currents of the glutamate transporter and the  $\text{Na}^+$ - $\text{K}^+$  pump have a strong effect on the intracellular  $\text{Na}^+$  concentration, the effect of the  $\text{Na}^+$ - $\text{Ca}^{2+}$  exchanger is negligible (see Figure 1.5). The maximal intracellular  $\text{Na}^+$  concentration ( $\Delta\text{Na}^+$ ) increases with an increase of the current strength of the glu-

tamate transporter and a decrease of the current strength of the  $\text{Na}^+$ - $\text{K}^+$  pump (see Figure 1.5 a). Thus, the glutamate transporter is mainly responsible for the transport of  $\text{Na}^+$  into the astrocyte. The  $\text{Na}^+$ - $\text{K}^+$  pump in turn counteracts the function of the glutamate transporter, so that  $\text{Na}^+$  is pumped out of the astrocyte and the intracellular  $\text{Na}^+$  concentration saturates at lower concentration levels.

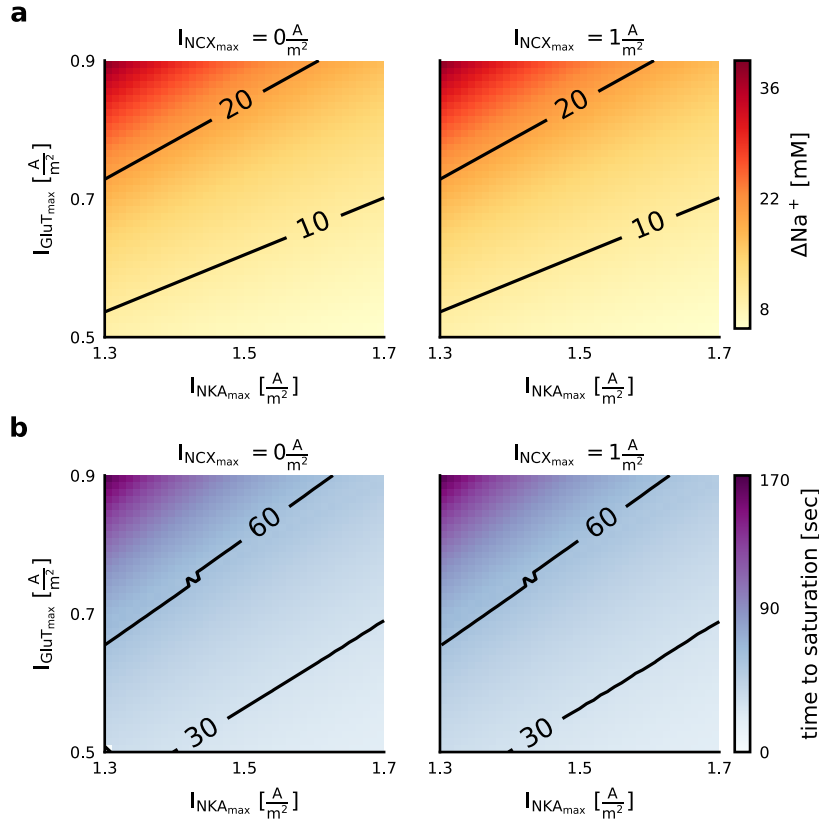


Figure 1.5: Increase of the  $\text{Na}^+$  concentration in the intracellular compartment,  $[\text{Na}^+]_i$ , during a constant extracellular glutamate concentration for different values of the maximal pump currents of the  $\text{Na}^+$ - $\text{Ca}^{2+}$  exchanger ( $I_{\text{NCX}_{\text{max}}}$ ), the glutamate transporter ( $I_{\text{GluT}_{\text{max}}}$ ), the  $\text{Na}^+$ /K<sup>+</sup>-ATPase ( $I_{\text{NKA}_{\text{max}}}$ ). The astrocytic compartment is stimulated for 200 seconds with a constant extracellular glutamate concentration of  $100 \mu\text{M}$ . The surface volume ratio (SVR) is set equal to  $1^{-1} \mu\text{m}$ , which corresponds to astrocytic compartments close to the soma. **a**  $[\text{Na}^+]_i$  after 200 seconds with respect to its resting concentration ( $[\text{Na}^+]_{\text{rest}} = 15 \text{ mM}$ ,  $\Delta\text{Na}^+ = [\text{Na}^+]_{\text{End}} - [\text{Na}^+]_{\text{rest}}$ ) for a maximal pump current of the  $\text{Na}^+$ - $\text{Ca}^{2+}$  exchanger ( $I_{\text{NCX}_{\text{max}}}$ ) equal to  $0 \frac{\text{A}}{\text{m}^2}$  (left) or equal to  $1 \frac{\text{A}}{\text{m}^2}$  (right) and different values of the maximal pump current of the glutamate transporter ( $I_{\text{GluT}_{\text{max}}}$ ) and the  $\text{Na}^+$ /K<sup>+</sup>-ATPase ( $I_{\text{NKA}_{\text{max}}}$ ). **b** Time until saturation is reached for a maximal pump current of the  $\text{Na}^+$ - $\text{Ca}^{2+}$  exchanger ( $I_{\text{NCX}_{\text{max}}}$ ) equal to  $0 \frac{\text{A}}{\text{m}^2}$  (left) or equal to  $1 \frac{\text{A}}{\text{m}^2}$  (right) and different values of the maximal pump current of the glutamate transporter ( $I_{\text{GluT}_{\text{max}}}$ ) and the  $\text{Na}^+$ /K<sup>+</sup>-ATPase ( $I_{\text{NKA}_{\text{max}}}$ ). The time to saturation is defined as the time required for the intracellular  $\text{Na}^+$  concentration to reach a constant concentration. Figure and caption adapted from (Oschmann et al., 2017b).

The investigated parameters also determine the time until the  $\text{Na}^+$  concentration saturates (see Figure 1.5 b). Since a low activity of the glutamate transporter results in a low increase of the intracellular  $\text{Na}^+$  concentration, the saturation of the  $\text{Na}^+$

concentration is reached comparably fast. At the same time a high activity of the  $\text{Na}^+$ - $\text{K}^+$  pump intensifies this effect, as the reached maximal  $\text{Na}^+$  concentration is even lower.

In experimental studies an increase of the intracellular  $\text{Na}^+$  concentration between 10 mM and 20 mM in response to external glutamate stimulation was observed. The maximal  $\text{Na}^+$  concentration saturated with an increase of the applied glutamate concentrations and reached its steady state level in under 60 seconds (Rose and Karus, 2013). Based on the comparison of these experimental results and the performed parameter exploration, I choose the following values for the maximal pump currents of the glutamate transporter and the  $\text{Na}^+$ - $\text{K}^+$  pump for the upcoming simulations:  $I_{\text{GluT}_{\text{max}}} = 0.75 \frac{\text{A}}{\text{m}^2}$  and  $I_{\text{NKAT}_{\text{max}}} = 1.52 \frac{\text{A}}{\text{m}^2}$ .

In summary, the glutamate transporter promotes a high increase of the  $\text{Na}^+$  concentration. The  $\text{Na}^+$ - $\text{K}^+$  pump counteracts this effect and the  $\text{Na}^+$  concentration saturates at lower levels for a higher activity of the  $\text{Na}^+$ - $\text{K}^+$  pump. The time until the  $\text{Na}^+$  increase saturates is in general favored by a high activity of the glutamate transporter and a low activity of the  $\text{Na}^+$ - $\text{K}^+$  pump.

## 2.2 $\text{Ca}^{2+}$ transport through the plasma membrane

As a next step, I include  $\text{Ca}^{2+}$  entry from the extracellular space into the model and study its effect on the  $\text{Ca}^{2+}$  release from the internal store. For this purpose I vary the maximal pump currents of both the  $\text{Na}^+$ - $\text{Ca}^{2+}$  exchanger ( $I_{\text{NCX}_{\text{max}}}$ ) and the glutamate transporter ( $I_{\text{GluT}_{\text{max}}}$ ), as these currents modulate the  $\text{Ca}^{2+}$  entry from the extracellular space. Moreover, in order to parameterize the model for different positions along the astrocytic process, I study the impact of the  $\text{Ca}^{2+}$  entry on the  $\text{Ca}^{2+}$  release for different values of the volume fraction of internal  $\text{Ca}^{2+}$  stores ( $\text{ratio}_{\text{ER}}$ ).

First, I investigate the impact of the  $\text{Ca}^{2+}$  entry from the extracellular space mediated by the  $\text{Na}^+$ - $\text{Ca}^{2+}$  exchanger on the intracellular  $\text{Ca}^{2+}$  signal along the astrocytic process (see Figure 1.6). During a blocked  $\text{Ca}^{2+}$  entry from the extracellular space ( $I_{\text{NCX}_{\text{max}}} = 0 \frac{\text{pA}}{\mu\text{m}^2}$ ),  $\text{Ca}^{2+}$  oscillations solely occur for a high volume fraction of the internal  $\text{Ca}^{2+}$  store ( $\text{ratio}_{\text{ER}} > 0.06$ ) (see Figure 1.6 a, f and g). During an increase of the maximal pump current of the  $\text{Na}^+$ - $\text{Ca}^{2+}$  exchanger this critical point for the onset of  $\text{Ca}^{2+}$  oscillations shifts to higher values of the volume fraction of the internal  $\text{Ca}^{2+}$  store (see Figure 1.6 a) and culminates in a complete suppression of the  $\text{Ca}^{2+}$  oscillations (see Figure 1.6 e). Moreover, astrocytic compartments lacking the internal  $\text{Ca}^{2+}$  store ( $\text{ratio}_{\text{ER}} = 0$ ) show an increase of the intracellular  $\text{Ca}^{2+}$  concentration during an active  $\text{Ca}^{2+}$  transport ( $I_{\text{NCX}_{\text{max}}} > 0 \frac{\text{pA}}{\mu\text{m}^2}$ ) (see Figure 1.6 c and b).

Second, I analyze the impact of the  $\text{Na}^+$  transport into the astrocyte mediated by the glutamate transporter on the intracellular  $\text{Ca}^{2+}$  signal. For this purpose, I vary the maximal pump current of the glutamate transporter ( $I_{\text{GluT}_{\text{max}}}$ ) (see Figure 1.7). The influence of the glutamate transporter activity on the  $\text{Ca}^{2+}$  signal is mainly determined by the maximal pump current of the  $\text{Na}^+$ - $\text{Ca}^{2+}$  exchanger ( $I_{\text{NCX}_{\text{max}}}$ ) and the volume fraction of the internal  $\text{Ca}^{2+}$  store ( $\text{ratio}_{\text{ER}}$ ). For example in astrocytic

compartments close to the soma, an increase of the glutamate transporter activity enhances the  $\text{Ca}^{2+}$  oscillation frequency up to a maximal value (see Figure 1.7 a and b). A further increase of the glutamate transporter activity beyond this point leads to a decrease of the oscillation frequency. An increase of the activity of the  $\text{Na}^+$ - $\text{Ca}^{2+}$  exchanger, however, lowers the maximal value of the oscillation frequency. The cause of the suppressing effect of the  $\text{Na}^+$ - $\text{Ca}^{2+}$  exchanger on the  $\text{Ca}^{2+}$  oscillations is investigated in the Results Section 2.4.

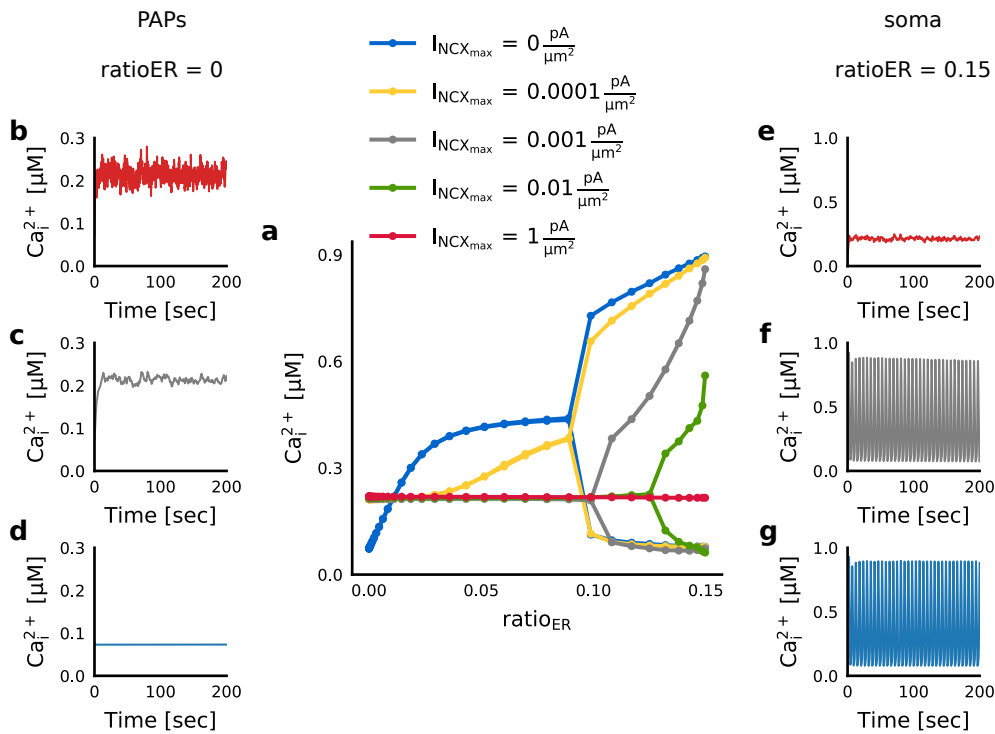


Figure 1.6: **Dynamics of the  $\text{Ca}^{2+}$  concentration in the intracellular compartment during synaptic activation for different values of the maximal pump current of the  $\text{Na}^+$ - $\text{Ca}^{2+}$  exchanger ( $I_{\text{NCXmax}}$ ).** The astrocytic compartment is stimulated for 200 seconds with a Poisson spike train of 100 Hz. The corresponding glutamate concentration in the extracellular compartment as a function of time is calculated using the Tsodyks and Markram model. **a**  $\text{Ca}_i^{2+}$  as a function of the volume ratio ( $\text{ratio}_{\text{ER}}$ ) of internal  $\text{Ca}^{2+}$  stores and the maximal pump current of the  $\text{Na}^+$ - $\text{Ca}^{2+}$  exchanger ( $I_{\text{NCXmax}}$ ). The upper and lower symbols denote the average height of peaks and troughs of the emerging  $\text{Ca}^{2+}$  oscillations (in [μM]). In case no oscillations are present, the symbols denote the average concentration of  $\text{Ca}^{2+}$  over the stimulation period. **b-d** Time course of the  $\text{Ca}^{2+}$  concentration for  $\text{ratio}_{\text{ER}} = 0$  and  $I_{\text{NCXmax}}$  equal to  $0 \frac{\text{pA}}{\mu\text{m}^2}$  (blue),  $0.01 \frac{\text{pA}}{\mu\text{m}^2}$  (gray) and  $1 \frac{\text{pA}}{\mu\text{m}^2}$  (red). **e-g** Time course of the  $\text{Ca}^{2+}$  concentration for  $\text{ratio}_{\text{ER}} = 0.15$  and  $I_{\text{NCXmax}}$  equal to  $0 \frac{\text{pA}}{\mu\text{m}^2}$  (blue),  $0.01 \frac{\text{pA}}{\mu\text{m}^2}$  (gray) and  $1 \frac{\text{pA}}{\mu\text{m}^2}$  (red). Figure and caption adapted from (Oschmann et al., 2017b).

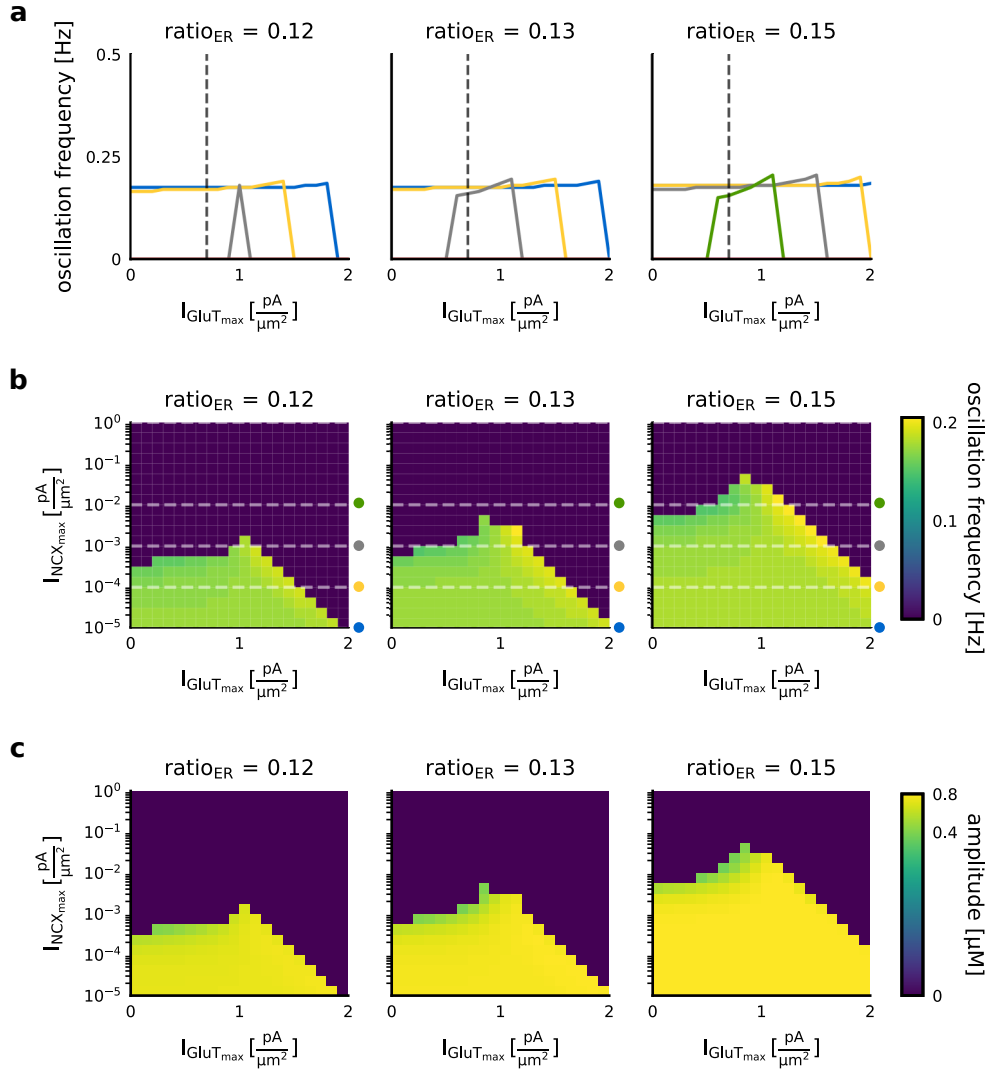


Figure 1.7:  $\text{Ca}^{2+}$  oscillation frequency and amplitude for different values of the volume ratio between the internal  $\text{Ca}^{2+}$  store and the intracellular space ( $\text{ratio}_{\text{ER}}$ ), as well as the maximal pump currents of the  $\text{Na}^{+}\text{-Ca}^{2+}$  exchanger ( $I_{\text{NCX}_{\text{max}}}$ ) and the glutamate transporter ( $I_{\text{GluT}_{\text{max}}}$ ). The astrocytic compartment is stimulated for 200 seconds with a Poisson spike train of 100 Hz. **a**  $\text{Ca}^{2+}$  oscillation frequency for three different values of  $\text{ratio}_{\text{ER}}$  (0.12, 0.13 and 0.15), as a function of  $I_{\text{GluT}_{\text{max}}}$  and  $I_{\text{NCX}_{\text{max}}}$ . The colored lines correspond to  $I_{\text{NCX}_{\text{max}}}$  equal to  $0.00001 \frac{\text{pA}}{\mu\text{m}^2}$  (blue),  $0.0001 \frac{\text{pA}}{\mu\text{m}^2}$  (yellow),  $0.001 \frac{\text{pA}}{\mu\text{m}^2}$  (gray) and  $0.01 \frac{\text{pA}}{\mu\text{m}^2}$  (green). The dashed line corresponds to  $I_{\text{GluT}_{\text{max}}}$  equal to  $0.75 \frac{\text{pA}}{\mu\text{m}^2}$ . **b**  $\text{Ca}^{2+}$  oscillation frequencies for three different values of  $\text{ratio}_{\text{ER}}$  (0.12, 0.13 and 0.15), as a function of  $I_{\text{GluT}_{\text{max}}}$  and  $I_{\text{NCX}_{\text{max}}}$ . The colored symbols denote the values of  $I_{\text{NCX}_{\text{max}}}$  shown in **a**. **c**  $\text{Ca}^{2+}$  oscillation amplitudes for three different values of  $\text{ratio}_{\text{ER}}$  (0.12, 0.13 and 0.15), and as a function of  $I_{\text{GluT}_{\text{max}}}$  and  $I_{\text{NCX}_{\text{max}}}$ . Figure and caption adapted from (Oschmann et al., 2017b).

Moreover, the volume of the internal  $\text{Ca}^{2+}$  store determines the  $\text{Ca}^{2+}$  oscillation amplitude (see Figure 1.7 c). An increase of the volume fraction of the internal  $\text{Ca}^{2+}$  store is accompanied with a decrease of the surface volume ratio and thus also with the increase of the volumes of both the internal  $\text{Ca}^{2+}$  store and the intracellular space. The increased volume of the internal  $\text{Ca}^{2+}$  stores allows an enhanced release of  $\text{Ca}^{2+}$  from internal stores and thus also an increased oscillation amplitude. In summary, taking the  $\text{Ca}^{2+}$  entry from the extracellular space into account shows the expected  $\text{Ca}^{2+}$  fluctuations in astrocytic compartments devoid of the internal  $\text{Ca}^{2+}$  store. However, with increasing activity of the  $\text{Na}^+$ - $\text{Ca}^{2+}$  exchanger  $\text{Ca}^{2+}$  oscillations are suppressed, especially in astrocytic compartments with a high volume fraction of the internal  $\text{Ca}^{2+}$  store. Moreover, an increase of the glutamate transporter activity prevents a suppression of the  $\text{Ca}^{2+}$  oscillations.

### 2.3 Impact of the glutamate transporter activity on the $\text{Ca}^{2+}$ response under synaptic stimulation

During visual experiments in awake ferrets a clear attenuation of the astrocytic  $\text{Ca}^{2+}$  signal was observed when the glutamate transporter was blocked (Schummers et al., 2008). Based on these experimental results I investigate the  $\text{Ca}^{2+}$  signal generation during a blocked glutamate transporter.

In order to determine the influence of the glutamate transporter on the  $\text{Ca}^{2+}$  signal, I stimulate the astrocyte model for an active and a blocked glutamate transporter and I compute the difference between both curves. I perform this experiment for various values of the activity of the  $\text{Na}^+$ - $\text{Ca}^{2+}$  exchanger activity ( $I_{\text{NCX}_{\text{max}}}$ ) as well as the volume fraction of the internal  $\text{Ca}^{2+}$  store ( $\text{ratio}_{\text{ER}}$ ). Figure 1.8 summarizes the results of this experiment.

The impact of the glutamate transporter on the  $\text{Ca}^{2+}$  signal is highest for a high activity of the  $\text{Na}^+$ - $\text{Ca}^{2+}$  exchanger ( $I_{\text{NCX}_{\text{max}}} > 0.1 \frac{\text{pA}}{\mu\text{m}^2}$ ) and a low volume fraction of the internal  $\text{Ca}^{2+}$  store ( $\text{ratio} < 0.1$ ) (see Figure 1.8 b). This impact of the glutamate transporter on the  $\text{Ca}^{2+}$  signal decreases with a decrease of the  $\text{Na}^+$ - $\text{Ca}^{2+}$  exchanger activity and an increase of the volume fraction of the internal  $\text{Ca}^{2+}$  store.

The impact of the glutamate transporter is highest in compartments with a low volume fraction of the internal  $\text{Ca}^{2+}$  store (see Figure 1.8 b and e), because in these compartments  $\text{Ca}^{2+}$  signals are mainly generated by  $\text{Ca}^{2+}$  entry from the extracellular space (see Figure 1.4). A blocked glutamate transporter prevents the accumulation of  $\text{Na}^+$  in the intracellular space (see Figure 1.9) and a switch of the  $\text{Na}^+$ - $\text{Ca}^{2+}$  exchanger into the reverse mode. Therefore, a block of the glutamate transporter inhibits the  $\text{Ca}^{2+}$  entry mediated by the the  $\text{Na}^+$ - $\text{Ca}^{2+}$  exchanger into the astrocyte and evokes an attenuation of the  $\text{Ca}^{2+}$  signals in astrocytic regions with a small volume fraction of the internal  $\text{Ca}^{2+}$  store. An increase of the volume fraction of the internal  $\text{Ca}^{2+}$  store allows  $\text{Ca}^{2+}$  release from internal stores and thus also the impact of the glutamate transporter on the  $\text{Ca}^{2+}$  signal decreases (see Figure 1.8 b, c and d).

In summary, these simulation results suggest that a clear attenuation of the  $\text{Ca}^{2+}$  signal during a block of the glutamate transporter can primarily be observed in

astrocytic compartments with a low volume fraction of the internal  $\text{Ca}^{2+}$  store.

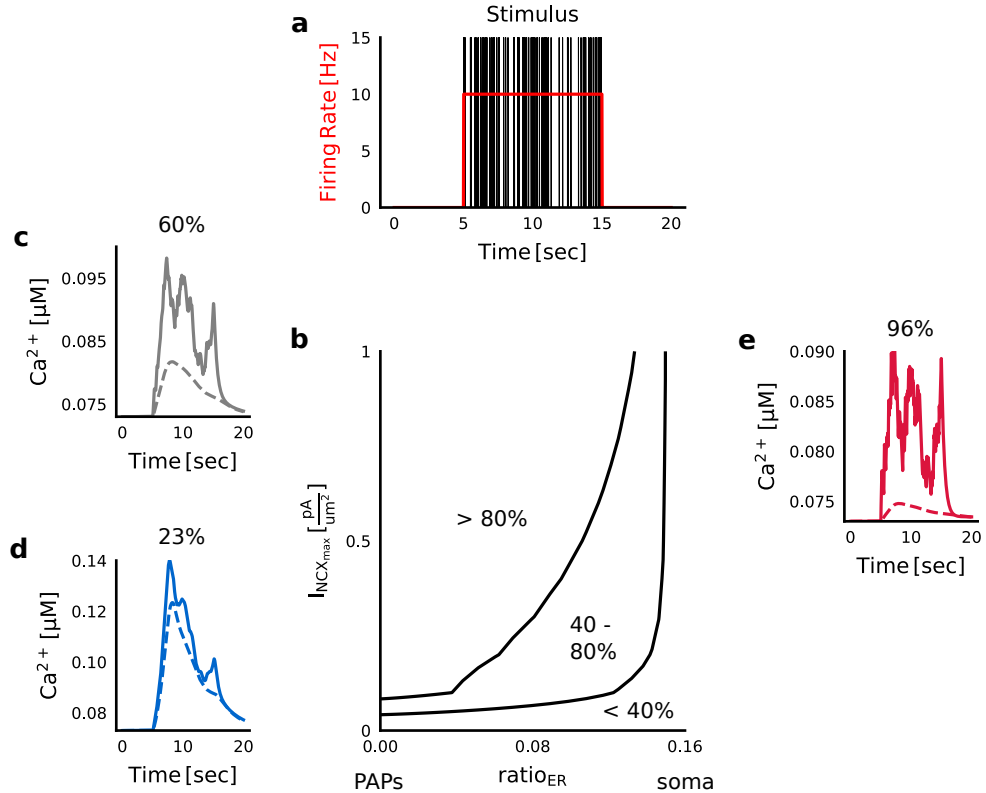


Figure 1.8: **Dynamics of the  $\text{Ca}^{2+}$  concentration in the intracellular compartment under synaptic stimulation for a blocked glutamate transporter (GluT) in comparison to the control condition.** **a** The astrocytic compartment is stimulated for 10 seconds with a Poisson spike train of 10 Hz. The corresponding glutamate concentration in the extracellular compartment as a function of time is calculated using the Tsodyks and Markram model. **b** Reduction of the  $\text{Ca}^{2+}$  response under block of the GluT as a function of the maximal pump current of the  $\text{Na}^+$ - $\text{Ca}^{2+}$  exchanger ( $I_{\text{NCX}_{\text{max}}}$ ) and the volume ratio ( $\text{ratio}_{\text{ER}}$ ) between the internal  $\text{Ca}^{2+}$  store and the intracellular compartment. The reduction was quantified by the difference of the average  $\text{Ca}^{2+}$  concentration under control condition and block normalized by the difference between the  $\text{Ca}^{2+}$  concentration in the control condition and the  $\text{Ca}^{2+}$  concentration without stimulation. Solid lines separate the parameter space concerning the reduction: larger than 80%, between 40% and 80% and under 40%. **c-e**  $\text{Ca}^{2+}$  response as a function of time for different values of  $I_{\text{NCX}_{\text{max}}}$  and  $\text{ratio}_{\text{ER}}$ . These traces correspond to a reduction of the  $\text{Ca}^{2+}$  signal of 29%, 67% and 97%. Solid and dashed lines correspond to control condition and block. The block was simulated by setting  $I_{\text{GluT}_{\text{max}}}$  equal to  $0 \frac{\text{pA}}{\mu\text{m}^2}$ . Figure and caption adapted from (Oschmann et al., 2017b).

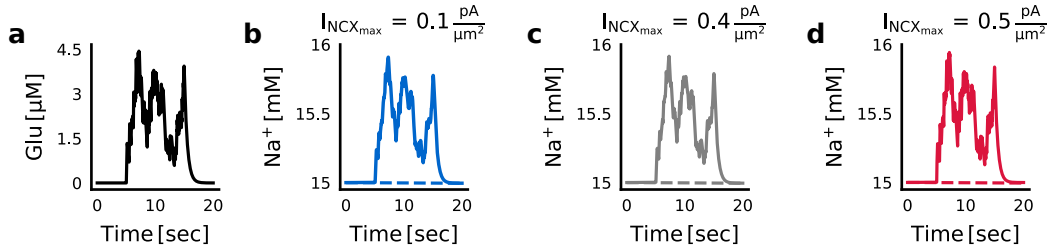


Figure 1.9: **Increase of the intracellular  $\text{Na}^+$  concentration during synaptic stimulation.** Dynamics of the  $\text{Na}^+$  concentration in the intracellular compartment under synaptic stimulation for a blocked glutamate transporter in comparison to the control condition. The astrocytic compartment is stimulated for 10 seconds with a Poisson spike train of 10 Hz (see Figure 1.8). **a** Time course of the glutamate concentration in the extracellular compartment calculated with the Tsodyks and Markram model. **b-d** Time course of the intracellular  $\text{Na}^+$  concentration for three different parameter combinations of the volume ratio between the internal  $\text{Ca}^{2+}$  store and the intracellular space ( $\text{ratio}_{\text{ER}}$ ) and the maximal pump current of the  $\text{Na}^+$ - $\text{Ca}^{2+}$  exchanger ( $I_{\text{NCX}_{\text{max}}}$ ). The intracellular  $\text{Na}^+$  concentration is shown for the same parameter combinations of  $I_{\text{NCX}_{\text{max}}}$  and  $\text{ratio}_{\text{ER}}$  as  $\text{Ca}^{2+}$  in Figure 1.8 c, d and e (**b**:  $\text{ratio}_{\text{ER}} = 0.14$  and  $I_{\text{NCX}_{\text{max}}} = 0.1 \frac{\text{pA}}{\mu\text{m}^2}$ , **c**:  $\text{ratio}_{\text{ER}} = 0.12$  and  $I_{\text{NCX}_{\text{max}}} = 0.4 \frac{\text{pA}}{\mu\text{m}^2}$ , **d**:  $\text{ratio}_{\text{ER}} = 0.03$  and  $I_{\text{NCX}_{\text{max}}} = 0.5 \frac{\text{pA}}{\mu\text{m}^2}$ ). Solid and dashed lines corresponds to the control condition and a block of the glutamate transporter, respectively. Figure and caption adapted from (Oschmann et al., 2017b).

## 2.4 Interaction of the mGluR-dependent and GluT-dependent pathway

Finally, I study the mechanisms underlying the interaction of  $\text{Ca}^{2+}$  release from internal stores and  $\text{Ca}^{2+}$  entry from the extracellular space (see Figure 1.10). For that purpose I change the impact of both pathways by varying the volume ratio of internal  $\text{Ca}^{2+}$  stores ( $\text{ratio}_{\text{ER}}$ ) and the maximal pump current of the  $\text{Na}^+$ - $\text{Ca}^{2+}$  exchanger ( $I_{\text{NCX}_{\text{max}}}$ ) and study the  $\text{Ca}^{2+}$  level in all three spaces.

First, I analyze the impact of  $\text{Ca}^{2+}$  entry on the intracellular  $\text{Ca}^{2+}$  concentration in isolation and neglect  $\text{Ca}^{2+}$  release from internal  $\text{Ca}^{2+}$  stores (see Figure 1.10 a). During external stimulation with glutamate the  $\text{Na}^+$ - $\text{Ca}^{2+}$  exchanger produces  $\text{Ca}^{2+}$  entry into the cell. In this case the steady state of the intracellular  $\text{Ca}^{2+}$  concentration is independent of the maximal pump current of the  $\text{Na}^+$ - $\text{Ca}^{2+}$  exchanger.

During active  $\text{Ca}^{2+}$  release from internal stores and  $\text{Ca}^{2+}$  entry from the extracellular space a high maximal pump current of the  $\text{Na}^+$ - $\text{Ca}^{2+}$  exchanger causes a suppression of  $\text{Ca}^{2+}$  oscillations in all three spaces (see Figure 1.10 d, e and f). The same oscillatory behavior is also reflected in the dynamics of  $\text{IP}_3$  and h. When comparing the  $\text{Ca}^{2+}$  levels in all three spaces during a high activity of the  $\text{Na}^+$ - $\text{Ca}^{2+}$  exchanger ( $I_{\text{NCX}_{\text{max}}} = 1 \frac{\text{A}}{\text{m}^2}$ ) to the resting concentrations, I observe a strong deviation of these levels from the resting concentrations. At rest the concentrations of  $\text{Ca}^{2+}$  in the three spaces are:  $\text{Ca}^{2+}_{\text{i}} = 0.073 \mu\text{M}$ ,  $\text{Ca}^{2+}_{\text{o}} = 1800 \mu\text{M}$  and  $\text{Ca}^{2+}_{\text{ER}} = 19 \mu\text{M}$ . A strong maximal pump current of the  $\text{Na}^+$ - $\text{Ca}^{2+}$  exchanger decreases the the  $\text{Ca}^{2+}$  concentration in the internal  $\text{Ca}^{2+}$  store and increases the  $\text{Ca}^{2+}$  concentration in the intracellular and the extracellular space compared to their resting concentrations (see Table 3.3). Thus, a strong maximal pump current leads to a depletion of the internal  $\text{Ca}^{2+}$  store and by that prevents the generation of  $\text{Ca}^{2+}$  oscillations.

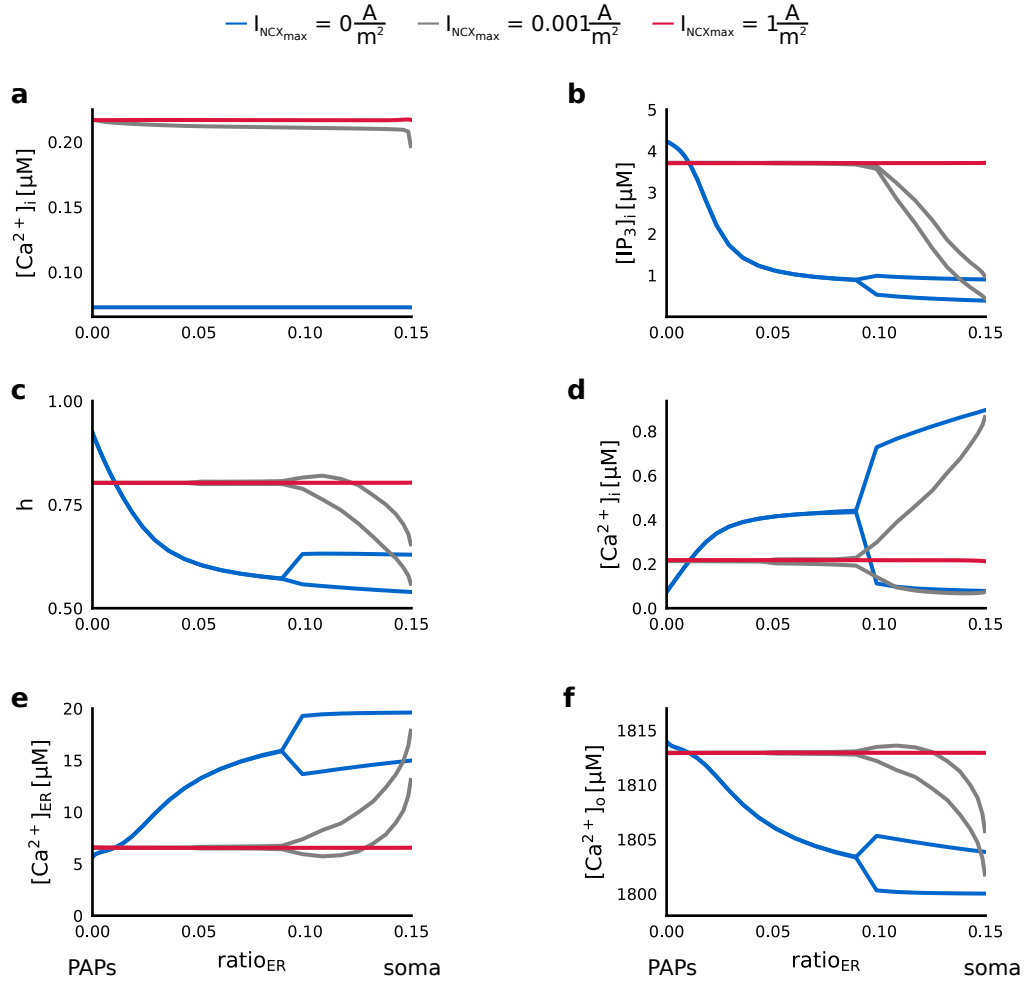


Figure 1.10:  $\text{Ca}^{2+}$  concentrations in the intracellular space, the internal  $\text{Ca}^{2+}$  store and the extracellular space, the  $\text{IP}_3$  concentration in the intracellular space and the ratio  $h$  of active  $\text{IP}_3$  receptor channels as a function of the maximal pump current of the  $\text{Na}^+$ - $\text{Ca}^{2+}$  exchanger ( $I_{\text{NCXmax}}$ ) and the volume ratio between the internal  $\text{Ca}^{2+}$  store and the intracellular space ( $\text{ratio}_{\text{ER}}$ ). The astrocytic compartment is stimulated for 200 seconds with a Poisson spike train of 100 Hz. The corresponding glutamate concentration in the extracellular compartment as a function of time is calculated using the Tsodyks and Markram model. Blue, gray and red lines denote the dynamics of  $[\text{IP}_3]_i$ ,  $h$ ,  $[\text{Ca}^{2+}]_i$ ,  $[\text{Ca}^{2+}]_{\text{ER}}$ ,  $[\text{Ca}^{2+}]_o$  for values of  $I_{\text{NCXmax}}$  equal to  $0 \frac{\text{pA}}{\mu\text{m}^2}$ ,  $0.001 \frac{\text{pA}}{\mu\text{m}^2}$  and  $1 \frac{\text{pA}}{\mu\text{m}^2}$ . **a** Analysis of the  $\text{Ca}^{2+}$  entry from the extracellular space in isolation.  $\text{Ca}^{2+}_i$  is shown as a function of  $\text{ratio}_{\text{ER}}$  and for different values of  $I_{\text{NCXmax}}$ . **b-f** Analysis of both pathways.  $\text{IP}_3$ ,  $h$ ,  $\text{Ca}^{2+}_i$ ,  $\text{Ca}^{2+}_{\text{ER}}$  and  $\text{Ca}^{2+}_o$  are shown as a function of  $\text{ratio}_{\text{ER}}$  and for different values of  $I_{\text{NCXmax}}$ . Figure and caption adapted from (Oschmann et al., 2017b).

# Discussion

Within this first part of my thesis I developed and studied a computational model for calcium signal generation along an astrocytic process. The novelty of this computational model is, the consideration of two different pathways for the generation of calcium signals in astrocytes, and the parametrization for different positions along an astrocytic process by a change of the volume fraction of the internal calcium store.

The analysis of the computational model revealed four main findings: 1) during the isolated consideration of the pathway for calcium release from internal stores calcium oscillations were solely observed for model parametrizations with a high volume fraction of the internal calcium store, 2) during the additional consideration of the pathway for calcium entry from the extracellular space I observed that a high maximal pump current of the sodium-calcium exchanger suppresses calcium oscillations and that the sodium-calcium exchanger generates calcium fluctuations in astrocytic compartments devoid of the internal calcium store, 3) the impact of the calcium entry from the extracellular space on the calcium signal generation was highest for a high activity of the sodium-calcium exchanger and a low volume fraction of the internal calcium store, 4) the suppression of calcium oscillations during a high activity of the sodium-calcium exchanger was caused by an increased efflux of calcium from the internal calcium store into the intracellular as well as extracellular space.

In their study Srinivasan et al. (2015) proposed a spatial separation of calcium signal generation pathways along the astrocytic process. During their experiments they observed that in astrocytic compartments close to the soma calcium signals are mainly induced by calcium release from internal stores through the  $IP_3$  receptor channel. However, a knock-out of this receptor channel did not lead to a clear reduction of calcium signals in astrocytic compartments close the synapse. These experimental results are in great agreement with my simulation results. The consideration of the pathway for calcium release from internal stores in isolation caused long-lasting oscillations for model parametrizations accounting for a high volume fraction of the internal calcium store. For for model parametrizations with an absent internal calcium store the intracellular calcium concentration remained unchanged. Moreover, Srinivasan et al. (2015) showed that in astrocytic compartments close to the synapse a significant proportion of calcium signals is evoked by transmembrane calcium fluxes. Also these experimental results can be reproduced with my model, as the consideration of a transmembrane calcium current allows the generation of

calcium signals in astrocytic compartments devoid of an internal calcium store. However, the presented simulation results also showed that a high activity of the sodium-calcium exchanger suppressed the calcium oscillations generated by calcium release from internal stores. In contrast, a high activity of the sodium-calcium exchanger favored the impact of calcium entry from the extracellular space on the calcium signal generation in astrocytic compartments with a low volume of the internal calcium store. Based on these simulation results I propose that the transporter activity of the sodium-calcium exchanger varies along the astrocytic process with a low activity in astrocytic compartments close to the soma and a high activity in astrocytic compartments close to the synapse. This hypothesis is also supported by experimental results, which report a concentration and colocalization of sodium-calcium exchangers, sodium-potassium pumps and glutamate transporters in perisynaptic astrocytic processes (Minelli et al., 2007; Danbolt, 2001).

The above named findings also hint to different functions of astrocytic processes and the soma regarding the sense and integration of neuronal activity. For example, the high surface volume ratio of perisynaptic astrocytic processes support localized accumulations of sodium and calcium within the intracellular space (Rusakov et al., 2011), which enables these astrocytic compartments to sense individual synaptic events. Store-operated calcium signals, however, respond to larger elevations of calcium or  $IP_3$  within the intracellular space, which suggests that these astrocytic compartments act as integrators of local network activity (Patrushev et al., 2013).

Within this first part of the thesis I developed and studied a computational model for calcium signal generation in astrocytes. Moreover, I discussed the roles of different calcium signal generation pathways and subcellular compartments in the detection of synaptic events. However, as this model only describes the calcium signal generation at one point within an extended astrocyte, the propagation of signals along the astrocytic process is not considered. For the purpose of investigating calcium signal propagation, I also developed a multi-compartment model, which is described and analyzed in part 3.

**Part 2**

**Model reduction**



# Introduction

As already discussed within the previous part of my thesis, astrocytic calcium signals are produced by two mechanisms: calcium release from internal stores and calcium entry from the extracellular space. While the calcium release from internal stores is usually mediated by the calcium efflux through calcium- and  $IP_3$ -sensitive receptor channels at the internal calcium store, the calcium entry from the extracellular space can be mediated by different pathways. These mechanisms either include calcium transporters or calcium-permeable ion channels (Bazargani and Attwell, 2016). Both calcium transporters and calcium-permeable ion channels are indirectly or directly activated by neurotransmitters in the extracellular space. For example glutamate release by neurons activates glutamate transporters and NMDA receptors and promotes sodium elevations in the intracellular space of astrocytes (Rose and Karus, 2013). The increased sodium concentration activates sodium-calcium exchangers within the astrocytic membrane and gives rise to calcium entry into astrocytes (Rojas et al., 2007). Calcium-permeable ion channels, however, are directly activated by the binding of neurotransmitters. These ion channels are for example AMPA, NMDA or P2X receptors, or TRPA1 channels (Hamilton et al., 2008; Shigetomi et al., 2012). Thus, due to the high variety of mechanisms for either calcium release from internal stores or calcium entry from the extracellular space, calcium signal generation in astrocytes is a highly versatile process.

Due to the variety of calcium signal generation mechanisms in astrocytes, mathematical models for calcium signal generation differ very much in their composition of considered ion channels and receptors and are thus difficult to compare. Most mathematical models for calcium signal generation in astrocytes focus on calcium release from internal stores (Nadkarni and Jung, 2007; De Pittà et al., 2009) and neglect the impact of calcium entry from the extracellular space. Recently, various models extended existing models for calcium release from internal stores with calcium entry from the extracellular space (Postnov et al., 2008; Oschmann et al., 2017b; Handy et al., 2017). Thereby, different mechanisms for calcium entry are applied like store operated calcium channels (Handy et al., 2017), voltage-gated calcium channels (Postnov et al., 2008) or sodium-calcium exchangers (Oschmann et al., 2017b). However, the above named models not only differ in their mechanisms for calcium entry from the extracellular space, but also in their considered mathematical description of calcium release from internal stores. In addition, most mathematical models considering both mechanisms are rather complex and do not allow a profound analytic analysis, which also hinders the handling of these mod-

els. Thus, a comparison of the various models and the model parametrization is hardly possible.

On the basis of the above named limitations of current mathematical models concerning their handling, their comparability and their informative value my aim is to develop a reduced model for calcium signal generation in astrocytes. For that purpose I reduce the former published model for calcium signal generation evoked by both calcium release and calcium entry (see part 1 and Oschmann et al. (2017b)). The derivation of the reduced model is based on a separation of time-scales of the dynamical variables. The behavior of the derived reduced model and of the full model coincide quantitatively and qualitatively. Moreover, the stability analysis reveals important insights about the steady state behavior of the reduced model in response to parameter variations.

# Model

The subject of the following section is the derivation and analysis of a reduced model for  $\text{Ca}^{2+}$  signal generation in astrocytes. For this purpose I reduce the full, seven-dimensional model, which was introduced in the previous part (see part 1), to a four-dimensional one. The model reduction is based on a separation of time-scales of the dynamical variables. Finally, I outline how I perform the stability analysis of this four-dimensional model.

## 1 Model reduction

Considering the simulation results of the full model it can easily be seen that the model variables show oscillations with either a high or a very low amplitude (see Figure 2.1). Whereas the model variables  $\text{Ca}^{2+}_i$ ,  $\text{Ca}^{2+}_{\text{ER}}$ ,  $\text{IP}_3$  and  $h$  show long lasting oscillations with an amplitude many times higher than their resting concentration, the model variables  $\text{Na}^+_i$ ,  $\text{K}^+_i$  and  $V$  show small oscillations in the nM and nV range.

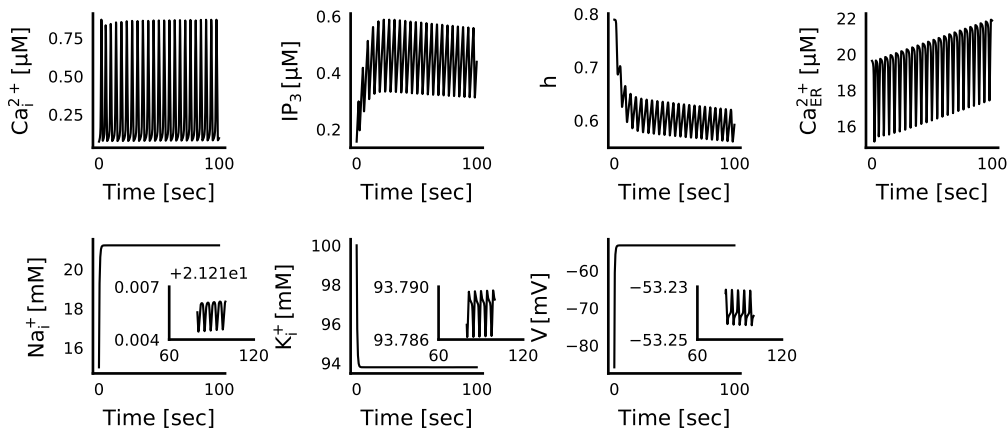


Figure 2.1: **The time-dependent behavior of the dynamical variables of the full model.** The full model is stimulated with a constant glutamate concentration of 0.1 mM. The oscillations of  $\text{Na}^+_i$ ,  $\text{K}^+_i$  and  $V$  are displayed in the image magnification due to their small amplitude. The volume fraction of the internal  $\text{Ca}^{2+}$  store ( $\text{ratio}_{\text{ER}}$ ) is set to 0.15.

The mechanisms at the internal calcium store (including  $I_{\text{IP}_3\text{R}}$ ,  $I_{\text{Serca}}$ ,  $I_{\text{CaERleak}}$ ) and at the plasma membrane (including  $I_{\text{GluT}}$ ,  $I_{\text{NKA}}$ ,  $I_{\text{NCX}}$ , leak currents) act almost

independent of each other. The only similarity is their dependence on  $\text{Ca}^{2+}_i$ . While changes of  $\text{Ca}^{2+}_i$  seemingly have a huge impact on  $\text{Ca}^{2+}_{\text{ER}}$ ,  $\text{IP}_3$  and  $h$ ,  $\text{Ca}^{2+}_i$  has a rather small impact on  $\text{Na}^+_i$ ,  $\text{K}^+_i$  and  $V$ . This point is particularly obvious considering the strengths of the currents crossing the cell membrane (see Figure 2.2). While the  $\text{Ca}^{2+}$ -dependent  $\text{Na}^+$ - $\text{Ca}^{2+}$  exchanger has a current strength between  $-0.5$  and  $0.5 \frac{\mu\text{A}}{\text{m}^2}$ , the  $\text{Ca}^{2+}$ -independent glutamate transporter and the  $\text{Na}^+$ - $\text{K}^+$  pump operate with a current strength between  $0.01$  and  $1 \frac{\text{A}}{\text{m}^2}$ . Thus,  $\text{Na}^+_i$ ,  $\text{K}^+_i$  and  $V$  are mostly determined by the glutamate transporter and the  $\text{Na}^+$ - $\text{K}^+$  pump. For that reason, I assume that the impact of  $\text{Ca}^{2+}_i$  on  $\text{Na}^+_i$ ,  $\text{K}^+_i$  and  $V$  is negligible and that the dynamics of  $\text{Na}^+_i$ ,  $\text{K}^+_i$  and  $V$  can be analyzed separately from those of  $\text{Ca}^{2+}_i$ ,  $\text{Ca}^{2+}_{\text{ER}}$ ,  $\text{IP}_3$  and  $h$ .

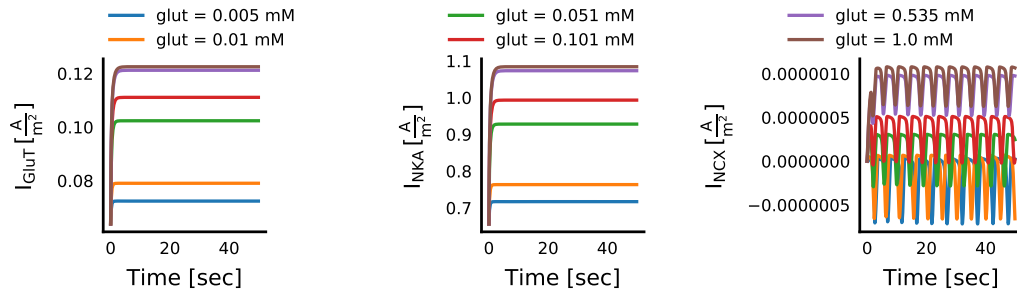


Figure 2.2: **The current strengths of the glutamate transporter ( $I_{\text{GluT}}$ ) and the  $\text{Na}^+$ - $\text{K}^+$  pump ( $I_{\text{NKA}}$ ) exceed the one of the  $\text{Na}^+$ - $\text{Ca}^{2+}$  exchanger ( $I_{\text{NCX}}$ ) by several orders of magnitude.** The current strengths of the glutamate transporter, the  $\text{Na}^+$ - $\text{K}^+$  pump and the  $\text{Na}^+$ - $\text{Ca}^{2+}$  exchanger are simulated for different glutamate concentrations between  $0.005$  mM and  $1$  mM. The colored lines represent the time-dependent behavior of the three membrane currents  $I_{\text{GluT}}$ ,  $I_{\text{NKA}}$  and  $I_{\text{NCX}}$  for these applied glutamate concentrations. The volume fraction of the internal  $\text{Ca}^{2+}$  store ( $\text{ratio}_{\text{ER}}$ ) is set to  $0.15$ .

The simulation results of  $\text{Na}^+_i$ ,  $\text{K}^+_i$  and  $V$  suggest that the steady state values rather than the time-dependent behavior of these variables have the main impact on the model dynamics. During a constant application of glutamate the model variables  $\text{Na}^+_i$ ,  $\text{K}^+_i$  and  $V$  show a rapid increase to a steady state level, which depends on the applied glutamate concentration (see Figure 2.3). For that reason, I aim to derive the steady state solutions of  $\text{Na}^+_i$ ,  $\text{K}^+_i$  and  $V$  in dependence of glutamate and include these time-independent solutions into the model.

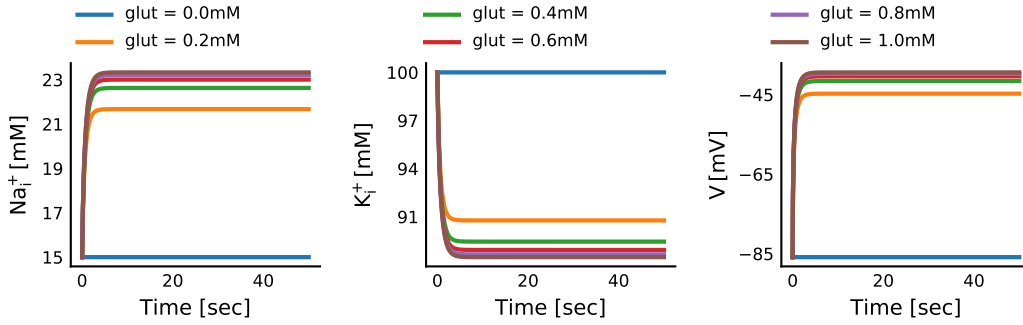


Figure 2.3: **The dynamical variables  $\text{Na}_i^+$ ,  $\text{K}_i^+$  and  $V$  converge to their glutamate-dependent steady-state values within a few seconds.** The three-dimensional system describing  $\text{Na}_i^+$ ,  $\text{K}_i^+$  and  $V$  is simulated for different constant glutamate concentrations (0 - 1 mM). The colored lines represent the time-dependent behavior of the dynamical variables  $\text{Na}_i^+$ ,  $\text{K}_i^+$  and  $V$  for the different applied constant glutamate concentrations.

### 1.0.1 Steady state values of $\text{Na}_i^+$ , $\text{K}_i^+$ and $V$

The dynamics of  $\text{Na}_i^+$ ,  $\text{K}_i^+$  and  $V$  are defined by the following three-dimensional dynamical system:

$$\frac{d\text{Na}_i^+}{dt} = \frac{A}{F \cdot \text{Vol} \cdot (1 - \text{ratio}_{ER})} \cdot (3I_{GluT} - 3I_{NKA} - I_{\text{Na}_{leak}}), \quad (2.1)$$

$$\frac{d\text{K}_i^+}{dt} = \frac{A}{F \cdot \text{Vol} \cdot (1 - \text{ratio}_{ER})} \cdot (-I_{GluT} + 2I_{NKA} - I_{\text{K}_{leak}}), \quad (2.2)$$

$$\frac{dV}{dt} = \frac{1}{C_m} (2I_{GluT} - I_{NKA} - I_{\text{Na}_{leak}} - I_{\text{K}_{leak}}). \quad (2.3)$$

Here, the  $\text{Na}^+$ - $\text{Ca}^{2+}$  exchanger is neglected due to its low impact on  $\text{Na}^+$  and  $V$ . The nonlinear system shown above is under-determined and thus it is not possible to derive a unique solution of the steady state. This statement applies to glutamate concentrations equal to and greater than zero. However, in case the fixed point solution of one of the three variables is known, there is a unique solution for the fixed points of the remaining two variables. Here, I assume the fixed point solution of  $\text{Na}_i^+$  as given and solve the remaining system for the fixed points of  $\text{K}_i^+$  and  $V$ . The resulting fixed point solution of  $V$  reads as follows:

$$V = \frac{1}{g_{\text{Na}_{leak}}} \cdot (3I_{GluT} - 3I_{NKA}) + E_{\text{Na}}.$$

Based on the assumption that the Nernst potential of  $\text{K}^+$  depends on the intra- and extracellular concentrations of  $\text{K}^+$ , the fixed point solution of  $\text{K}^+$  can not be determined analytically. For this reason, I apply the bisection method in order to determine the zeros of the following equation:

$$-I_{GluT} \cdot (3g_{\text{K}_{leak}} + g_{\text{Na}_{leak}}) + I_{NKA} \cdot (3g_{\text{K}_{leak}} + 2g_{\text{Na}_{leak}}) - (g_{\text{Na}_{leak}} \cdot g_{\text{K}_{leak}}) \cdot (E_{\text{Na}} - E_{\text{K}}) = 0$$

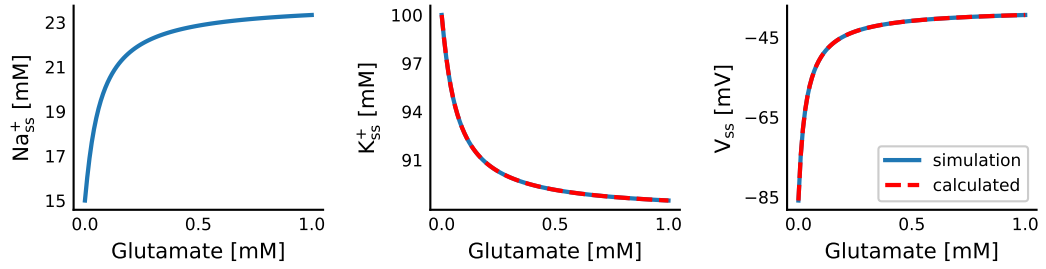


Figure 2.4: The steady states of the dynamic variables  $K^+_i$  and  $V$  in dependence on the applied glutamate concentration can be calculated given that the fixed points of the  $Na^+_i$  concentration ( $Na^+_{ss}$ ) are known. First, the three-dimensional system describing  $Na^+_i$ ,  $K^+_i$  and  $V$  is simulated for different constant glutamate concentrations (0 - 1 mM). The volume fraction of the internal  $Ca^{2+}$  ( $ratio_{ER}$ ) is equal to 0.15. The blue lines denote the simulated fixed point curves of all dynamical variables. Second, the fixed points of  $K^+_i$  and  $V$  ( $K^+_{ss}$  and  $V_{ss}$ ) are determined analytically based on the simulated fixed point curve of  $Na^+_i$  and the applied glutamate concentration. The dashed red lines denote the calculated fixed point curves of  $K^+_i$  and  $V$ .

The calculated fixed points of  $K^+_i$  and  $V$  exactly match the simulated fixed points of these variable (see Figure 2.4).

Moreover, the application of different values of assumed constant glutamate levels and steady state values of  $Na^+$  ( $Na^+_{ss}$ ) to these equations produces different values of computed steady state levels of  $K^+$  and  $V$  (see Figure 2.5).

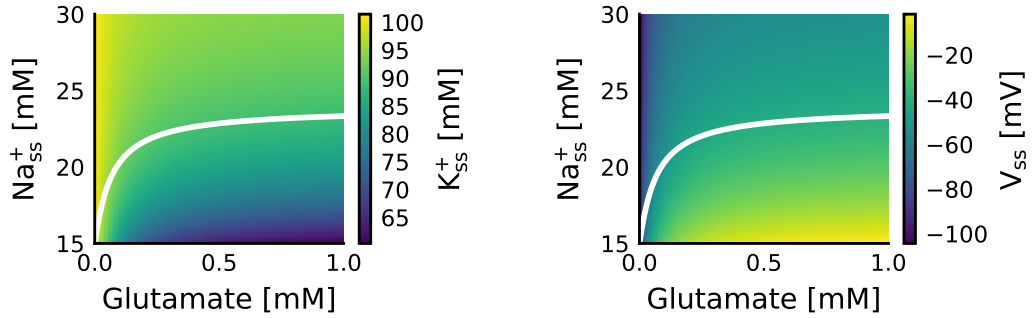


Figure 2.5: The applied values of the steady state values of  $Na^+$  ( $Na^+_{ss}$ ) and the applied glutamate concentration determine the values of the steady state values of  $K^+$  ( $K^+_{ss}$ ) and  $V$  ( $V_{ss}$ ). The steady state values of  $K^+$  and  $V$  are computed assuming different combinations of  $Na^+_{ss}$  (15 mM - 30 mM) and glutamate (0 mM - 1 mM) by applying the equations obtained in Model Section 1.0.1. The white line denotes the steady state curve of  $Na^+$  in dependence on the glutamate concentration.

Given the fact, that the system is under-determined, the system produces an infinite amount of solutions depending on the initial conditions. Moreover, the stability analysis of these steady state solutions reveals that the system is marginally unstable. One of the eigenvalues is close to zero and either positive or negative depending on the chosen initial condition ( $\lambda_2 \in [-10^{-13}, 10^{-13}]$ ). The other two eigenvalues are negative ( $\lambda_1 = -1700$  and  $\lambda_3 = -5$ ). As  $\lambda_2$  is comparable small, I assume the influence of that eigenvalue to be insignificant. Since I am only interested

in the achieved levels of  $\text{Na}^+$ ,  $\text{K}^+$  and  $V$  during constant glutamate applications and an already well-established parametrization, I continue to use the computed steady-state curves and proceed with the model simplification.

In order to obtain simple equations for the fixed points of all three dynamical variables, I choose to fit nonlinear functions to the simulated steady state curves of  $\text{Na}^+_{i,ss}$ ,  $\text{K}^+_{i,ss}$  and  $V$  (see Figure 2.6). These desired functions should only depend on the input, the applied glutamate concentration, as all other parameters of the system are well established. Since the dependence of the fixed point curves of  $\text{Na}^+_{i,ss}$ ,  $\text{K}^+_{i,ss}$  and  $V$  on glutamate shows a saturating curve progression, I describe the fitted curves by a logistic function.

The glutamate-dependent functions for the fixed points of  $\text{Na}^+_{i,ss}$ ,  $\text{K}^+_{i,ss}$  and  $V$  are as follows:

$$\begin{aligned} \text{Na}^+_{i,ss} &= a_{\text{Na}} \cdot \frac{\text{glut}}{\text{glut} + b_{\text{Na}}} + c_{\text{Na}} \\ \text{K}^+_{i,ss} &= a_{\text{K}} \cdot \frac{\text{glut}}{\text{glut} + b_{\text{K}}} + c_{\text{K}} \\ V_{ss} &= a_{\text{V}} \cdot \frac{\text{glut}}{\text{glut} + b_{\text{V}}} + c_{\text{V}}. \end{aligned}$$

Here,  $a_{\text{Na}}$ ,  $a_{\text{K}}$  and  $a_{\text{V}}$  define the slope of the glutamate-dependent function. The parameters  $b_{\text{Na}}$ ,  $b_{\text{K}}$  and  $b_{\text{V}}$  determine the saturation by glutamate. And  $c_{\text{Na}}$ ,  $c_{\text{K}}$  and  $c_{\text{V}}$  correspond to the maximal values  $\text{Na}^+$ ,  $\text{K}^+$  and  $V$  can reach during glutamate application. These parameters are fitted using the python package `scipy.optimize.curve_fit`, which applies non-linear least squares fit. All parameters of these fitted curves can be found in Table 2.1 .

The resulting fit of the fixed point curves of  $\text{Na}^+$ ,  $\text{K}^+$  and  $V$  is in accordance with the simulated fixed point curves for physiological values of  $\text{Na}^+$ ,  $\text{K}^+$  and  $V$  (see Figure 2.6 b and c).

Table 2.1: Model parameters for the steady-state values of  $\text{Na}^+_{i,ss}$ ,  $\text{K}^+_{i,ss}$  and  $V$  (see Section 1.0.1).

Parameter	Value	Description
$a_{\text{Na}}$	-6.72 mM	Scaling of $\text{Na}^+_{i,ss}$ increase
$b_{\text{Na}}$	-8.24 mM	Half-saturation constant of glutamate
$c_{\text{Na}}$	23.14 mM	Maximal $\text{Na}^+_{i,ss}$ concentration
$a_{\text{K}}$	6.72 mM	Scaling of $\text{K}^+_{i,ss}$ increase
$b_{\text{K}}$	8.24 mM	Half-saturation constant of glutamate
$c_{\text{K}}$	91.86 mM	Maximal $\text{K}^+_{i,ss}$ concentration
$a_{\text{V}}$	-28 mV	Scaling of the membrane voltage
$b_{\text{V}}$	11.54 mM	Half-saturation constant of glutamate
$c_{\text{V}}$	48 mV	Maximal membrane voltage

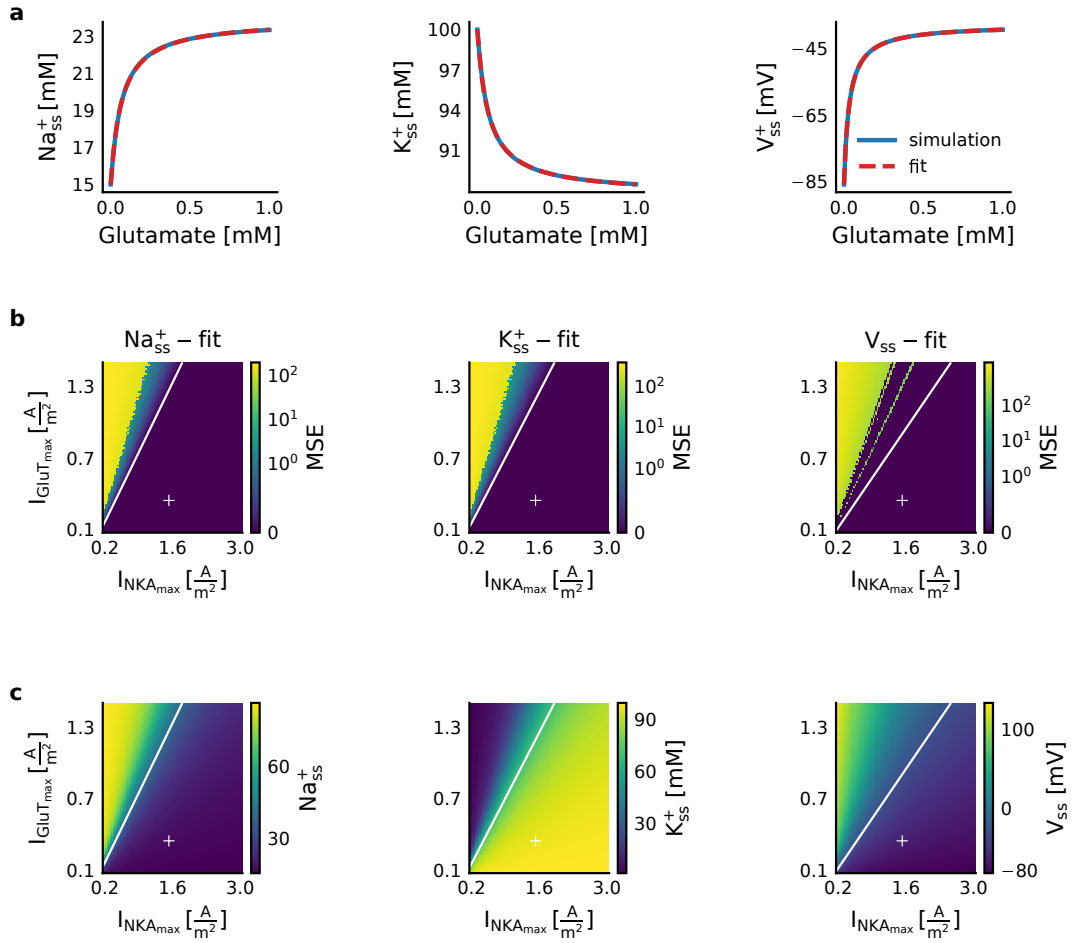


Figure 2.6: **The simulated and analytically calculated steady state values  $\text{Na}_{ss}^+$ ,  $\text{K}_{ss}^+$  and  $V_{ss}$  match in their dependence on the applied glutamate concentration.** **a** The simulated results of  $\text{Na}_{ss}^+$ ,  $\text{K}_{ss}^+$  and  $V_{ss}$  are obtained by simulating the three-dimensional dynamical system describing  $\text{Na}_{i}^+$ ,  $\text{K}_{i}^+$  and  $V$  for constant glutamate concentrations between 0 and 1 mM and for a duration of 200 seconds. The volume fraction of the internal  $\text{Ca}^{2+}$  (ratio<sub>ER</sub>) is equal to 0.15. The values of  $\text{Na}_{i}^+$ ,  $\text{K}_{i}^+$  and  $V$  at the end of the simulation time are defined as the simulated steady state values  $\text{Na}_{ss}^+$ ,  $\text{K}_{ss}^+$  and  $V_{ss}$ . The analytic solution is derived as described in Section 1.0.1. The simulation results are shown in blue and the fit is shown in red. **b** The fitted fixed point curves of  $\text{Na}^+$ ,  $\text{K}^+$  and  $V$  are in accordance with the simulation results for large parts of the parameter space of the maximal pump currents of the  $\text{Na}^+$ - $\text{K}^+$  pump ( $I_{\text{NKA}_{\text{max}}}$ ) and the glutamate transporter ( $I_{\text{GluT}_{\text{max}}}$ ). The fixed points curves of  $\text{Na}^+$ ,  $\text{K}^+$  and  $V$  are simulated and subsequently fitted for different values of  $I_{\text{NKA}_{\text{max}}}$  and  $I_{\text{GluT}_{\text{max}}}$ . The difference between the simulated and the fitted fixed point curves is computed with the mean-squared error. The figure shows the mean-squared error of the fitted fixed point curves in comparison to the simulated ones of  $\text{Na}_{ss}^+$ ,  $\text{K}_{ss}^+$  and  $V_{ss}$ . The white lines denote the boundary between physiological and unphysiological values of  $\text{Na}_{i}^+$ ,  $\text{K}_{i}^+$  and  $V$ . The white cross corresponds to the chosen default parameter combination of  $I_{\text{NKA}_{\text{max}}}$  and  $I_{\text{GluT}_{\text{max}}}$ . **c** Low values of the maximal pump current of the  $\text{Na}^+$ - $\text{K}^+$  pump ( $I_{\text{NKA}_{\text{max}}}$ ) and high values of the the maximal pump current of the glutamate transporter ( $I_{\text{GluT}_{\text{max}}}$ ) produce unphysiological values of  $\text{Na}_{ss}^+$ ,  $\text{K}_{ss}^+$  and  $V_{ss}$ . The fixed points of  $\text{Na}^+$ ,  $\text{K}^+$  and  $V$  are simulated for different values of  $I_{\text{NKA}_{\text{max}}}$  and  $I_{\text{GluT}_{\text{max}}}$ . The figure shows the values of the simulated fixed points of  $\text{Na}^+$ ,  $\text{K}^+$  and  $V$ . The following values are classified as unphysiological values:  $\text{Na}_{ss}^+ > 50$  mM,  $\text{K}_{ss}^+ < 50$  mM and  $V_{ss} > 0$  mV. The white cross corresponds to the chosen default parameter combination of  $I_{\text{NKA}_{\text{max}}}$  and  $I_{\text{GluT}_{\text{max}}}$ .

### 1.0.2 Extracellular $\text{Ca}^{2+}$ concentration ( $\text{Ca}^{2+}_o$ )

Due to the large differences of the  $\text{Ca}^{2+}$  concentration in the intracellular space, on the one side, and in the extracellular space, on the other side, changes of the  $\text{Ca}^{2+}$  concentration in the extracellular space have only a minor effect on the concentration change in the intracellular space (see Figure 2.7). Therefore, I assume the extracellular  $\text{Ca}^{2+}$  concentration to be constant and set it to its resting concentration.

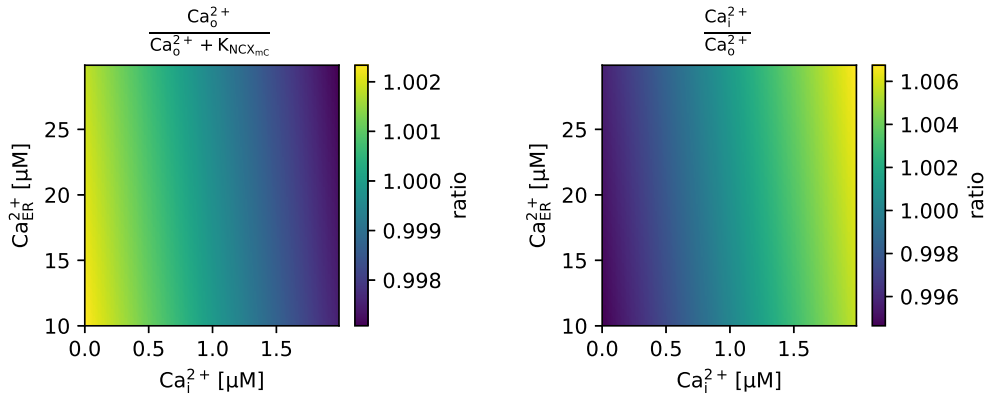


Figure 2.7: A dynamic extracellular  $\text{Ca}^{2+}$  concentration ( $\text{Ca}^{2+}_o$ ) has only little impact on the  $\text{Ca}^{2+}_o$ -dependent terms of the  $\text{Na}^+$ - $\text{Ca}^{2+}$  exchanger. The two  $\text{Ca}^{2+}_o$ -dependent terms of the  $\text{Na}^+$ - $\text{Ca}^{2+}$  exchanger were calculated for either a dynamic or a constant extracellular  $\text{Ca}^{2+}$  concentration and for value ranges of the  $\text{Ca}^{2+}$  concentration in the internal  $\text{Ca}^{2+}$  store ( $\text{Ca}^{2+}_{ER}$ ) and the intracellular space ( $\text{Ca}^{2+}_i$ ). The results for the dynamic and the constant  $\text{Ca}^{2+}_o$  were divided by each other in order to obtain a ratio. The two figures show the ratios calculated for the two  $\text{Ca}^{2+}_o$ -dependent terms. The two different  $\text{Ca}^{2+}_o$ -dependent terms are specified in the title of each figure.

## 1.1 Reduced model

The reduced model consists of the four-dimensional system of differential equations describing the dynamics of the intracellular  $\text{Ca}^{2+}$  concentration, the  $\text{Ca}^{2+}$  concentration in the internal  $\text{Ca}^{2+}$  store, the intracellular  $\text{IP}_3$  concentration and the fraction of activated  $\text{IP}_3$  receptor channels  $h$  within a single astrocytic compartment of an astrocytic process.:

$$\frac{d\text{Ca}^{2+}_i}{dt} = \frac{A}{F \cdot \text{Vol} \cdot (1 - \text{ratio}_{ER})} \cdot I_{NCX} - \frac{d\text{Ca}^{2+}_{ER}}{dt} \cdot \text{ratio}_{ER} \quad (2.4)$$

$$\frac{d\text{Ca}^{2+}_{ER}}{dt} = \frac{A \cdot \sqrt{\text{ratio}_{ER}}}{F \cdot \text{Vol} \cdot \text{ratio}_{ER}} \cdot (-I_{IP_3R} + I_{Serca} - I_{CERleak}) \quad (2.5)$$

$$\frac{d\text{IP}_3}{dt} = \text{prod}_{PLC\beta} + \text{prod}_{PLC\delta} - \text{degr}_{IP_3-3K} - \text{degr}_{IP-5P} \quad (2.6)$$

$$\frac{dh}{dt} = \frac{h_\infty - h}{\tau_h} \quad (2.7)$$

The definitions of the current equations  $I_{\text{NCX}}$ ,  $I_{\text{IP}_3\text{R}}$ ,  $I_{\text{Serca}}$  and  $I_{\text{CERleak}}$ , of the dynamical equation for the intracellular  $\text{IP}_3$  concentration and  $h$  as well as all parameter values are mentioned in the Model Section of part 1.

The intracellular concentrations of  $\text{Na}^+$  and  $\text{K}^+$  as well as the membrane voltage  $V$  are calculated by the fitted steady state curves derived in Section 1.0.1:

$$Na_{i,ss}^+ = a_{Na} \cdot \frac{glut}{glut + b_{Na}} + c_{Na} \quad (2.8)$$

$$K_{i,ss}^+ = a_K \cdot \frac{glut}{glut + b_K} + c_K \quad (2.9)$$

$$V_{ss} = a_V \cdot \frac{glut}{glut + b_V} + c_V \quad (2.10)$$

$$(2.11)$$

The extracellular concentrations of  $\text{Na}^+$  and  $\text{K}^+$  depend on their respective intracellular concentration changes and are described by:

$$Na_{o,ss}^+ - Na_{o,rest}^+ = Na_{i,rest}^+ - Na_{i,ss}^+ \quad (2.12)$$

$$K_{o,ss}^+ - K_{o,rest}^+ = K_{i,rest}^+ - K_{i,ss}^+. \quad (2.13)$$

The extracellular  $\text{Ca}^{2+}$  concentration is determined by its resting concentration:

$$Ca_o^{2+} = Ca_{o,rest}^{2+}. \quad (2.14)$$

## 1.2 Model behavior in response to parameter variations and stability analysis of the reduced model

Parameter variations of the maximal pump current of the  $\text{Na}^+$ - $\text{Ca}^{2+}$  exchanger ( $I_{\text{NCX}_{\text{max}}}$ ) and the volume fraction of the internal  $\text{Ca}^{2+}$  store ( $\text{ratio}_{\text{ER}}$ ) allow a parametrization of the dynamical system for any position along the astrocytic process between the soma and the perisynaptic astrocytic processes. Moreover, by setting either  $I_{\text{NCX}_{\text{max}}}$  or  $\text{ratio}_{\text{ER}}$  equals to zero the astrocyte model is reduced by one  $\text{Ca}^{2+}$  pool and the  $\text{Ca}^{2+}$  signal generation mechanisms can be analyzed separately. Thus, parameter variations of both  $I_{\text{NCX}_{\text{max}}}$  and  $\text{ratio}_{\text{ER}}$  have a huge impact on the dynamics of the system and its stability. For that reason, I analyze the impact of these parameters on the dynamical system, its fixed points and the stability of the fixed points.

### 1.2.1 $I_{\text{NCX}_{\text{max}}} > 0$ and $\text{ratio}_{\text{ER}} > 0$

**Fixed points** For a model parametrization with  $I_{\text{NCX}_{\text{max}}}$  and  $\text{ratio}_{\text{ER}}$  larger than zero the astrocyte model consists of all three  $\text{Ca}^{2+}$  pools: the internal  $\text{Ca}^{2+}$  store, the intracellular space and the extracellular space. Thus, both the  $\text{Ca}^{2+}$  release from internal stores and the  $\text{Ca}^{2+}$  entry from the extracellular space affect the intracellular  $\text{Ca}^{2+}$  concentration.

This model parametrization considering three  $\text{Ca}^{2+}$  pools allows the calculation

of the fixed points of the dynamical system by forward substitution. The steady state solution of a dynamical system does not change with time and all differential equations are equals to zero. As a result the fixed point of the intracellular  $Ca^{2+}$  concentration loses its dependence on  $\frac{dCa_{ER}^{2+}}{dt}$  and solely depends on the  $Ca^{2+}$  entry from the extracellular space. On that condition the analytic solution of the fixed point of  $Ca^{2+}_i$  is:

$$Ca_{i,fp}^{2+} = \frac{Na_{i,ss}^+ \cdot Ca_{o,0}^{2+}}{Na_{o,ss}^+} \cdot \exp\left(\frac{V_{ss} \cdot F}{R \cdot T}\right). \quad (2.15)$$

Since the differential equation for  $IP_3$  only depends on  $Ca^{2+}_i$  and  $IP_3$ , I determine the fixed point of  $IP_3$  ( $IP_{3,fp}$ ) by setting  $Ca^{2+}_{i,fp}$  into the differential equation and calculating the root of this differential equation. Due to the structure of that differential equation the solution can only be derived numerically with the help of a root finding method.

In the next step I determine the fixed point of the fraction of activated  $IP_3$  receptor channels,  $h$ , by again setting the fixed points of  $Ca^{2+}_i$  and  $IP_3$  into the differential equation of  $h$  and determining the zero of this differential equation. The fixed point of  $h$  ( $h_{fp}$ ) is defined by:

$$h_{fp} = \frac{d_2 \cdot \frac{IP_{3,fp} + d_1}{IP_{3,fp} + d_3}}{d_2 \cdot \frac{IP_{3,fp} + d_1}{IP_{3,fp} + d_3} + Ca_{i,fp}^{2+}}. \quad (2.16)$$

In the last step I determine the fixed point of the  $Ca^{2+}$  concentration in the internal  $Ca^{2+}$  store by again applying the above mentioned methods. The fixed point of  $Ca^{2+}_{ER}$  is defined by:

$$Ca_{ER,fp}^{2+} = ratio_{ER} \cdot \left( \frac{I_{Serca}}{r_L + r_C \cdot \frac{IP_{3,fp}^3}{IP_{3,1} + d_1} \cdot \frac{Ca_{i,fp}^{2+3}}{Ca_{i,fp}^{2+} + d_5} \cdot h_{fp}^3} \right) + Ca_{i,fp}^{2+} \quad (2.17)$$

Consequently, none of the fixed points depend on  $I_{NCX_{max}}$  or  $ratio_{ER}$ . Thus, changes of both parameters do not affect the fixed points of the four-dimensional dynamical system.

**Stability of fixed points** The stability of the fixed points is determined by the eigenvalues of the Jacobian matrix. The Jacobian matrix ( $J$ ) consists of the first-order partial derivatives of the dynamical system:

$$J = \begin{bmatrix} \frac{\partial f_1}{\partial Ca_{ER}^{2+}} & \frac{\partial f_1}{\partial Ca_i^{2+}} & \frac{\partial f_1}{\partial IP_3} & \frac{\partial f_1}{\partial h} \\ \frac{\partial f_2}{\partial Ca_{ER}^{2+}} & \frac{\partial f_2}{\partial Ca_i^{2+}} & \frac{\partial f_2}{\partial IP_3} & \frac{\partial f_2}{\partial h} \\ \frac{\partial f_3}{\partial Ca_{ER}^{2+}} & \frac{\partial f_3}{\partial Ca_i^{2+}} & \frac{\partial f_3}{\partial IP_3} & \frac{\partial f_3}{\partial h} \\ \frac{\partial f_4}{\partial Ca_{ER}^{2+}} & \frac{\partial f_4}{\partial Ca_i^{2+}} & \frac{\partial f_4}{\partial IP_3} & \frac{\partial f_4}{\partial h} \end{bmatrix}, \quad (2.18)$$

with

$$f_1 = \frac{dCa_{ER}^{2+}}{dt}, f_2 = \frac{dCa_i^{2+}}{dt}, f_3 = \frac{dIP_3}{dt}, f_4 = \frac{dh}{dt}. \quad (2.19)$$

In consideration of the partial derivatives the Jacobian matrix can be simplified to:

$$J = \begin{bmatrix} \frac{\partial f_1}{\partial Ca_{ER}^{2+}} & \frac{\partial f_1}{\partial Ca_i^{2+}} & \frac{\partial f_1}{\partial IP_3} & \frac{\partial f_1}{\partial h} \\ \frac{\partial f_2}{\partial Ca_{ER}^{2+}} & \frac{\partial f_2}{\partial Ca_i^{2+}} & \frac{\partial f_2}{\partial IP_3} & \frac{\partial f_2}{\partial h} \\ 0 & \frac{\partial f_3}{\partial Ca_i^{2+}} & \frac{\partial f_3}{\partial IP_3} & 0 \\ 0 & \frac{\partial f_4}{\partial Ca_i^{2+}} & \frac{\partial f_4}{\partial IP_3} & \frac{\partial f_4}{\partial h} \end{bmatrix}. \quad (2.20)$$

The fixed points are then classified according to the eigenvalues of the Jacobian matrix.

### 1.2.2 $I_{NCX_{max}} = 0$

A maximal pump current of the  $Na^+-Ca^{2+}$  exchanger equals to zero ( $I_{NCX_{max}} = 0 \frac{A}{m^2}$ ) reduces the astrocyte model by one  $Ca^{2+}$  pool and changes the  $Ca^{2+}$  signal generation in the intracellular space. With  $I_{NCX_{max}}$  equals to zero the  $Ca^{2+}$  entry from the extracellular space is nonexistent. Thus, this model parametrization reduces the model by one  $Ca^{2+}$  pool: the extracellular space. Moreover, in this case the intracellular  $Ca^{2+}$  concentration solely depends on the  $Ca^{2+}$  release from internal stores. Therefore, the differential equation for the intracellular  $Ca^{2+}$  concentration changes to:

$$\frac{dCa_i^{2+}}{dt} = -ratio_{ER} \cdot \frac{dCa_{ER}^{2+}}{dt} \Leftrightarrow \frac{dCa_{ER}^{2+}}{dt} = -\frac{1}{ratio_{ER}} \cdot \frac{dCa_i^{2+}}{dt}. \quad (2.21)$$

Thus, with  $I_{NCX_{max}}$  equals to zero  $\frac{dCa_{ER}^{2+}}{dt}$  is solvable and the solution of this differential equation is:

$$Ca_{ER}^{2+}(t) = (Ca_{i_{rest}}^{2+} - Ca_i^{2+}(t)) \cdot \frac{1}{ratio_{ER}} + Ca_{ER_{rest}}^{2+}. \quad (2.22)$$

The remaining differential equations are not affected by a change of  $I_{NCX_{max}}$  and read as follows:

$$\frac{dCa_i^{2+}}{dt} = \frac{A \cdot \sqrt{ratio_{ER}}}{F \cdot Vol} \cdot (I_{IP_3R} - I_{Serca} + I_{C_{ER}leak}) \quad (2.23)$$

$$\frac{dIP_3}{dt} = prod_{PLC\beta} + prod_{PLC\delta} - degr_{IP_3-3K} - degr_{IP-5P} \quad (2.24)$$

$$\frac{dh}{dt} = \frac{h_\infty - h}{\tau_h}. \quad (2.25)$$

These modified model conditions do not allow a straightforward solution of  $Ca_i^{2+}$ , fp. This also means, that all other fixed points can not be solved by forward substitution. Instead, I determine the solution of all fixed points numerically.

### 1.2.3 ratio<sub>ER</sub> = 0

In case the volume fraction of the internal Ca<sup>2+</sup> store is equals to zero (ratio<sub>ER</sub> = 0) both the Ca<sup>2+</sup> concentration in the internal Ca<sup>2+</sup> store (Ca<sup>2+</sup><sub>ER</sub>) as well as the fraction of activated IP<sub>3</sub> receptor channels (h) lose their meaning and their differential equations can be neglected. This parametrization with ratio<sub>ER</sub> equals to zero sets the volume of the internal Ca<sup>2+</sup> store equals to zero and the astrocyte model consists of only two Ca<sup>2+</sup> pools. Thus, solely the Ca<sup>2+</sup> entry from the extracellular space determines the intracellular Ca<sup>2+</sup> concentration. Therefore, the dynamical system reduces to two dynamical variables: the intracellular concentrations of Ca<sup>2+</sup> and IP<sub>3</sub>. At the same time the differential equation for the intracellular Ca<sup>2+</sup> concentration changes compared to the four-dimensional model:

$$\frac{dCa_i^{2+}}{dt} = \frac{A}{F \cdot Vol} \cdot I_{NCX} = a \cdot (b - d \cdot Ca_i^{2+}), \quad (2.26)$$

$$a = \frac{A \cdot I_{NCX_{max}} \cdot \frac{Na_o^{+3}}{K_{NCX_{mN}}^3 + Na_o^{+3}} \cdot \frac{Ca_o^{2+}}{K_{NCX_{mC}} + Ca_o^{2+}}}{F \cdot Vol \cdot (1 + k_{sat} \cdot \exp((\eta - 1) \cdot \frac{V \cdot F}{R \cdot T}))}, \quad (2.27)$$

$$b = \frac{Na_i^{+3}}{Na_o^{+3}} \cdot \exp(\eta \cdot \frac{V \cdot F}{R \cdot T}), \quad (2.28)$$

$$d = \frac{1}{Ca_o^{2+}} \cdot \exp((\eta - 1) \cdot \frac{V \cdot F}{R \cdot T}). \quad (2.29)$$

The solution of this changed differential equations is:

$$Ca_i^{2+}(t) = \frac{b}{d} + (Ca_{i_{rest}}^{2+} - \frac{b}{d}) \cdot e^{-adt} \quad (2.30)$$

The differential equation for the intracellular IP<sub>3</sub> concentration remains the same compared to the four-dimensional model.

The fixed point of Ca<sup>2+</sup><sub>i</sub> is determined by taking the limit of time to infinity. Thus the fraction  $\frac{b}{d}$  defines the fixed point of Ca<sup>2+</sup><sub>i</sub>. Applying the definitions of b and d reveals that the fixed point of Ca<sup>2+</sup><sub>i</sub> do not change compared to the four-dimensional model. Thus, also the fixed point of IP<sub>3</sub> remains the same.

Due to the altered model structure the model does not produce unstable behavior like oscillations any more. For the volume fraction of the internal Ca<sup>2+</sup> (ratio<sub>ER</sub>) equals to zero the dynamical system reduces to only two dimensions. Moreover, one of the two differential equations solely depends on itself and can be solved. A dynamical system can only produce oscillations if both differential equations depend on each other. Since this is not the case here, the model solely produces stable behavior.

## 1.3 Initialization of the dynamical system

The initial values of the intracellular and extracellular concentrations of Ca<sup>2+</sup>, Na<sup>+</sup> and K<sup>+</sup> are known from literature and can be found in Table 3.3 (part 1). The initial values of IP<sub>3</sub> and h are determined by deriving the zero of  $\frac{dIP_3}{dt}$  and  $\frac{dh}{dt}$ , respectively.

The zero of the current equation  $I_{NCX}$  reveals the initial value of the membrane voltage  $V$ , since an inactive current ensures a stable steady state at time point zero. The parameter values  $g_{Na\text{leak}}$  and  $g_{K\text{leak}}$  were calculated by solving  $\frac{dNa^+}{dt}$  and  $\frac{dK^+}{dt}$  for the respective parameters.

#### 1.4 Computational methods

All simulations were performed with Python 2.7 using the packages NumPy, SciPy and Matplotlib. The function `odeint` of the SciPy package was used for the numerical integration of the non-linear differential equations.

# Results

## 1 Comparison of the full and the reduced model

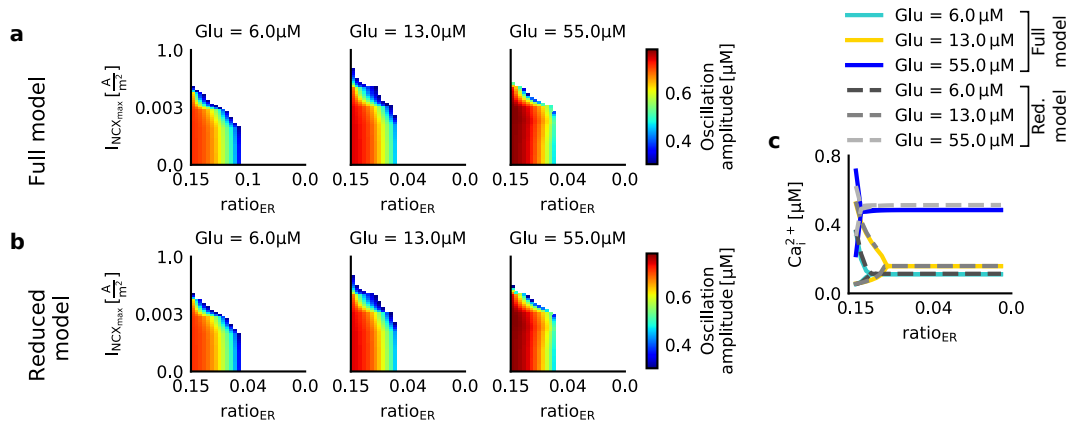


Figure 2.8: **The oscillatory behaviors of the full and the reduced model coincide with each other.** **a - b** The full model (in **a**) and the reduced model (in **b**) are simulated for constant glutamate concentrations of  $6\mu M$ ,  $13\mu M$  and  $55\mu M$  as well as for different values of the maximal pump current of the  $Na^+-Ca^{2+}$  exchanger ( $I_{NCX_{max}}$ ) and the volume fraction of the internal calcium store ( $ratio_{ER}$ ). The two different model variations were simulated for a duration of 200 seconds each. The color plots present the amplitudes of the full model (in **a**) and the reduced model (in **b**) for the different parameter combinations of the applied glutamate concentration,  $I_{NCX_{max}}$  and  $ratio_{ER}$ . The white areas correspond to the non-oscillatory ranges. **c** The figure shows the bifurcation curves of the intracellular  $Ca^{2+}$  concentration for three different applied glutamate concentrations ( $6\mu M$ ,  $13\mu M$  and  $55\mu M$ ), for one specific value of the maximal pump current of the  $Na^+-Ca^{2+}$  exchanger ( $I_{NCX_{max}}=0.01\frac{A}{m^2}$ ) and as a function of the volume fraction of the internal  $Ca^{2+}$  store ( $ratio_{ER}$ ). The solid and the dashed lines correspond to the bifurcation curves of the full and the reduced model, respectively.

A comparison of the full and the reduced model reveals that both model variations coincide very well in their steady-state behaviors and that the reduced model is sufficient for the analysis of the  $Ca^{2+}$  signal generation in astrocytes (see Figure 2.8). In order to compare the oscillatory behaviors of the full and the reduced model I simulate both model variations for a variety of parameter combinations and compare the results regarding the  $Ca^{2+}$  oscillation amplitudes, the upper and lower points of the  $Ca^{2+}$  oscillations as well as the bifurcation points (see Figure 2.8 a and b). The upper and lower points of the  $Ca^{2+}$  oscillations differ on average around  $0.007\mu M$  between the two model types. This difference corresponds to a change of

0.01 % as measured by an oscillation amplitude of  $0.6\mu\text{M}$ . Moreover, the bifurcation points of the full and the reduced model coincide for all parameter combinations (see Figure 2.8 c). Thus, the steady-state behavior of the reduced model is in accordance with that one of the full model. Therefore, I conclude that the reduced model is sufficient for the analysis of  $\text{Ca}^{2+}$  signal generation in astrocytes without losing qualitative or quantitative information generated by the full model.

### 1.1 Analysis of the reduced model

The analysis of the reduced model regarding its fixed points and its fixed point stabilities allows a detailed investigation of the  $\text{Ca}^{2+}$  signal generation in astrocytes. The fixed points of the intracellular  $\text{Ca}^{2+}$  concentration during an inactive ( $I_{\text{NCX}_{\text{max}}} = 0 \frac{\text{A}}{\text{m}^2}$ ) or an active  $\text{Ca}^{2+}$  influx ( $I_{\text{NCX}_{\text{max}}} > 0 \frac{\text{A}}{\text{m}^2}$ ) from the extracellular space are either determined by  $\text{Ca}^{2+}$  release from internal stores or by  $\text{Ca}^{2+}$  influx from the extracellular space, respectively (see Figure 2.9a-b). During an inactive  $\text{Ca}^{2+}$  influx from the extracellular space the fixed point of the intracellular  $\text{Ca}^{2+}$  concentration decreases with the volume of the internal  $\text{Ca}^{2+}$  store (decrease of  $\text{ratio}_{\text{ER}}$ ) and increases with the applied glutamate concentration (see Figure 2.9a). During an active  $\text{Ca}^{2+}$  influx from the extracellular space, however, the fixed point of the intracellular  $\text{Ca}^{2+}$  concentration solely depends on the applied glutamate concentration and is independent of the volume of the internal  $\text{Ca}^{2+}$  store (see Model Section 1.2.1 and Figure 2.9b). From these semi-analytic results I conclude that an inactive  $\text{Ca}^{2+}$  influx from the extracellular space promotes the  $\text{Ca}^{2+}$  release from internal stores whereas an active  $\text{Ca}^{2+}$  influx from the extracellular space primarily favors the  $\text{Ca}^{2+}$  transport into the astrocyte mediated by the  $\text{Na}^+$ - $\text{Ca}^{2+}$  exchanger. Moreover, during a finite  $\text{Ca}^{2+}$  influx from the extracellular space the fixed point of the intracellular  $\text{Ca}^{2+}$  concentration reaches higher concentration values ( $1.6\mu\text{M}$ ) compared to the inactive  $\text{Ca}^{2+}$  transport ( $0.4\mu\text{M}$ ).

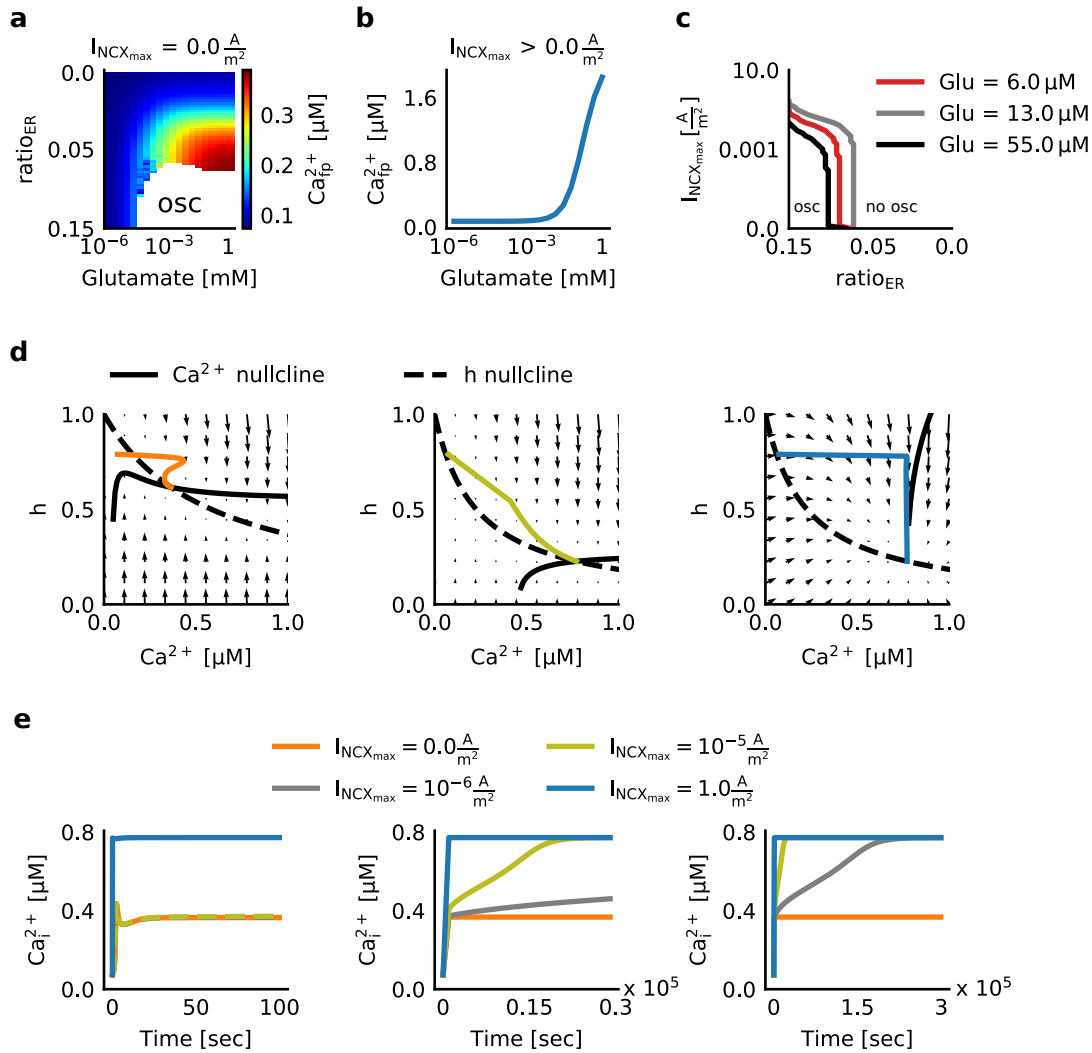


Figure 2.9: The applied glutamate concentration, the maximal pump current of the Na<sup>+</sup>-Ca<sup>2+</sup> exchanger ( $I_{\text{NCX}_{\text{max}}}$ ) and the volume fraction of the internal Ca<sup>2+</sup> store (ratio<sub>ER</sub>) determine the stability behavior of the reduced model. **a,b** The fixed points of the intracellular Ca<sup>2+</sup> (Ca<sup>2+</sup><sub>ip</sub>) concentration for either an inactive ( $I_{\text{NCX}_{\text{max}}}=0 \frac{\text{A}}{\text{m}^2}$ ) or an active Ca<sup>2+</sup> influx ( $I_{\text{NCX}_{\text{max}}}>0 \frac{\text{A}}{\text{m}^2}$ ) from the extracellular space. For  $I_{\text{NCX}_{\text{max}}}=0 \frac{\text{A}}{\text{m}^2}$  the colored area denotes the values of Ca<sup>2+</sup><sub>ip</sub> and the white area corresponds to the oscillatory range of the reduced model. For  $I_{\text{NCX}_{\text{max}}}>0 \frac{\text{A}}{\text{m}^2}$  (here:  $I_{\text{NCX}_{\text{max}}}=1 \frac{\text{A}}{\text{m}^2}$ ) Ca<sup>2+</sup><sub>ip</sub> is shown as a function of the applied glutamate concentration. **c** The stability behavior of the reduced model as a function of the applied glutamate concentration, of  $I_{\text{NCX}_{\text{max}}}$  and of ratio<sub>ER</sub>. The colored lines denote the boundary between the oscillatory and the non-oscillatory range for three different values of glutamate (6 μM, 13 μM and 55 μM), and for parameter combinations of  $I_{\text{NCX}_{\text{max}}}$  as well as of ratio<sub>ER</sub>. **d** The nullclines of the Ca<sup>2+</sup> concentration and h, the intersection of the nullclines and the vector field as a function of  $I_{\text{NCX}_{\text{max}}}$ . The three figures denote the nullclines with their corresponding vector fields and trajectories for  $I_{\text{NCX}_{\text{max}}}$  equals to 0  $\frac{\text{A}}{\text{m}^2}$  (orange), 10<sup>-5</sup>  $\frac{\text{A}}{\text{m}^2}$  (yellow) and 1  $\frac{\text{A}}{\text{m}^2}$  (blue), respectively. Here, the applied glutamate concentration is equal to 100 μM and ratio<sub>ER</sub> is equal to 0.05. The two other dynamical variables (IP<sub>3</sub> and Ca<sup>2+</sup><sub>ER</sub>) are held fixed at their fixed points. **e** The time course of the intracellular Ca<sup>2+</sup> concentration for different values of  $I_{\text{NCX}_{\text{max}}}$  and three different time durations (100 seconds, 30 000 seconds, and 300 000 seconds). The colored lines present the time course of Ca<sup>2+</sup><sub>i</sub> for  $I_{\text{NCX}_{\text{max}}}$  equals to 0  $\frac{\text{A}}{\text{m}^2}$  (orange), 10<sup>-6</sup>  $\frac{\text{A}}{\text{m}^2}$  (grey), 10<sup>-5</sup>  $\frac{\text{A}}{\text{m}^2}$  (yellow) and 1  $\frac{\text{A}}{\text{m}^2}$  (blue). Here, the applied glutamate concentration is equal to 100 μM and ratio<sub>ER</sub> is equal to 0.05.

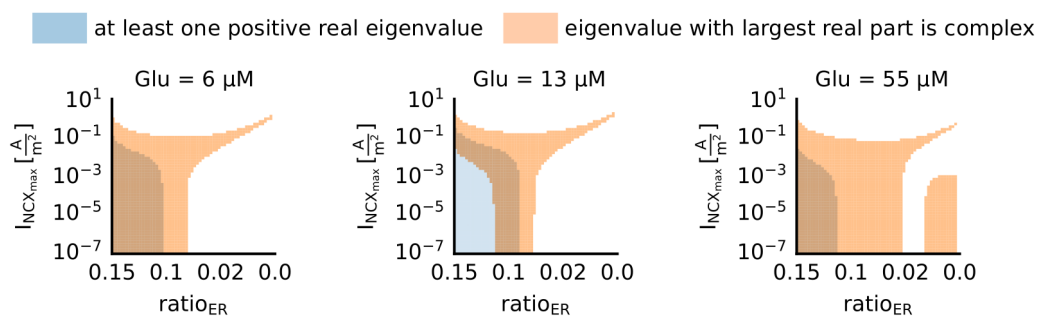


Figure 2.10: **The real parts of the eigenvalues mainly predict the transition between oscillatory and non-oscillatory model behavior.** The eigenvalues of the four-dimensional system were computed as a function of the applied glutamate concentration, the maximal pump current of the  $Na^+Ca^{2+}$  exchanger ( $I_{NCX_{max}}$ ) and the volume fraction of the internal  $Ca^{2+}$  store ( $ratio_{ER}$ ). The real parts of the eigenvalues were divided into two groups representing either the appearance of at least one positive real eigenvalue and the appearance of no positive real eigenvalue (blue areas). The eigenvalues were also divided according to the fact if the eigenvalue with the largest real part is also complex.

Although neither the maximal pump current of the  $Na^+Ca^{2+}$  exchanger nor the volume of the internal  $Ca^{2+}$  store affect the fixed points of the intracellular  $Ca^{2+}$  concentration during an active  $Ca^{2+}$  influx from the extracellular space, they affect the oscillation behavior of the model and thus the stability of the fixed points (see Figure 2.9c and Fig 2.10). Figure 2.9 c shows the border between parameter combinations, for which oscillations occur, and combinations, which do not produce oscillations. This model behavior in response to parameter variations is also reflected by the real and imaginary parts of the eigenvalues (see Figure 2.10). The real parts of the eigenvalues show a clear transition from at least one positive eigenvalue to solely negative eigenvalues and by that build the boundary between unstable to stable model behavior (see Figure 2.10). The oscillatory range of the reduced and the full model shrink for an increase of the  $Ca^{2+}$  influx from the extracellular space and a decrease of the volume of the internal  $Ca^{2+}$  store (see Figure 2.8 and Figure 2.9c). Moreover, the applied glutamate concentration increases the oscillatory range for values up to  $13 \mu M$  and decreases the oscillatory range for larger values (see Figure 2.9 b). The applied glutamate concentration determines the concentrations of  $Ca^{2+}$  and  $IP_3$  in the intracellular space (see Figure 2.9a,c) and thus also the opening probability of  $IP_3$  receptor channels at the internal  $Ca^{2+}$  store (Li and Rinzel, 1994). The opening probability of these channels in dependence on the intracellular  $Ca^{2+}$  concentration has a bell-shaped course and reaches its maximal value for intracellular  $Ca^{2+}$  concentrations around  $0.2 \mu M$ . Thus, by enhancing the intracellular  $Ca^{2+}$  concentration due to an increase of the glutamate concentration the opening probability exceeds its maximal value and less  $Ca^{2+}$  is released from internal  $Ca^{2+}$  stores. Therefore, glutamate concentrations larger than  $13 \mu M$  evoke less  $Ca^{2+}$  release from internal stores. For that reason,  $Ca^{2+}$  oscillations vanish and the size of the oscillatory range decreases. Consequently, for the generation of  $Ca^{2+}$  oscillations within the intracellular space the cooperation of  $Ca^{2+}$  release from internal stores and  $Ca^{2+}$  influx from the extracellular space is essential.

An inactive or active  $\text{Ca}^{2+}$  influx from the extracellular space does not only determine the fixed points of the intracellular  $\text{Ca}^{2+}$  concentration, but also the time scale of the  $\text{Ca}^{2+}$  dynamics (see Figure 2.9d-e). During an inactive  $\text{Ca}^{2+}$  influx from the extracellular space the intracellular  $\text{Ca}^{2+}$  concentration reaches its steady state within several seconds. In this case, the vector field is comparably small. The fixed point of  $\text{Ca}^{2+}$  is close to its resting value and only small changes are needed to reach the fixed point. The onset of the  $\text{Ca}^{2+}$  entry from the extracellular space changes the  $\text{Ca}^{2+}$  nullcline, the intersection of the nullclines and also the vector field (see Fig 2.9d). Moreover, the strength of the  $\text{Ca}^{2+}$  influx from the extracellular space ( $I_{\text{INCX}_{\text{max}}}$ ) determines the time-dependent dynamics of the  $\text{Ca}^{2+}$  concentration (see Fig 2.9e). A low  $\text{Ca}^{2+}$  influx from the extracellular space ( $I_{\text{INCX}_{\text{max}}} = 10^{-6} \frac{\text{A}}{\text{m}^2}$ ) results in a small vector field. This means that the  $\text{Ca}^{2+}$  concentration moves slowly from the resting value to its fixed point. Thus, a low  $I_{\text{INCX}_{\text{max}}}$  decelerates the model dynamics drastically and it takes up to 300 000 seconds until the  $\text{Ca}^{2+}$  concentration reaches its steady state. An increase of the  $\text{Ca}^{2+}$  influx from the extracellular space increases the vector field and the  $\text{Ca}^{2+}$  concentration moves fast from the resting value to its fixed point. Thus a high  $I_{\text{INCX}_{\text{max}}}$  accelerates the  $\text{Ca}^{2+}$  dynamics again and the  $\text{Ca}^{2+}$  concentration reaches its fixed point within several seconds (see Figure 2.9 d-e).

## 1.2 Prediction of the model behavior based on the eigenvalues of the Jacobian matrix

The eigenvalues of the Jacobian matrix of the reduced model predict the model behavior. The eigenvalues of the Jacobian matrix determine the stability of the fixed points. A transition from positive to negative real parts of an eigenvalue corresponds to the change from unstable to stable behavior of the model. Thus, the real parts of the eigenvalues predict the boundary between unstable and stable model behavior (see Figure 2.10 and Figure 2.11 a). For the reduced model two out of four eigenvalues show such a transition from positive to negative values and thus predict a transition from unstable to stable model behavior. The real parts of other two eigenvalues are solely negative.

The boundary between positive and negative real parts of the eigenvalues also predicts the model behavior in response to parameter variations (see Figure 2.11 b). The previous analysis of the reduced model revealed that during an increase of the  $\text{Ca}^{2+}$  influx the oscillatory range shrinks due to increased  $\text{Ca}^{2+}$  release from internal stores. This raises the question whether an altered  $\text{Ca}^{2+}$  release and uptake at internal  $\text{Ca}^{2+}$  stores could reverse the effect of a high  $\text{Ca}^{2+}$  influx. For that reason I compute the eigenvalues of the Jacobian matrix for variations of those parameters which determine the  $\text{Ca}^{2+}$  release and uptake at the internal  $\text{Ca}^{2+}$  store. The computed eigenvalues predict that the oscillatory range increases for a decrease of  $\text{Ca}^{2+}$  release and an increase of  $\text{Ca}^{2+}$  uptake.

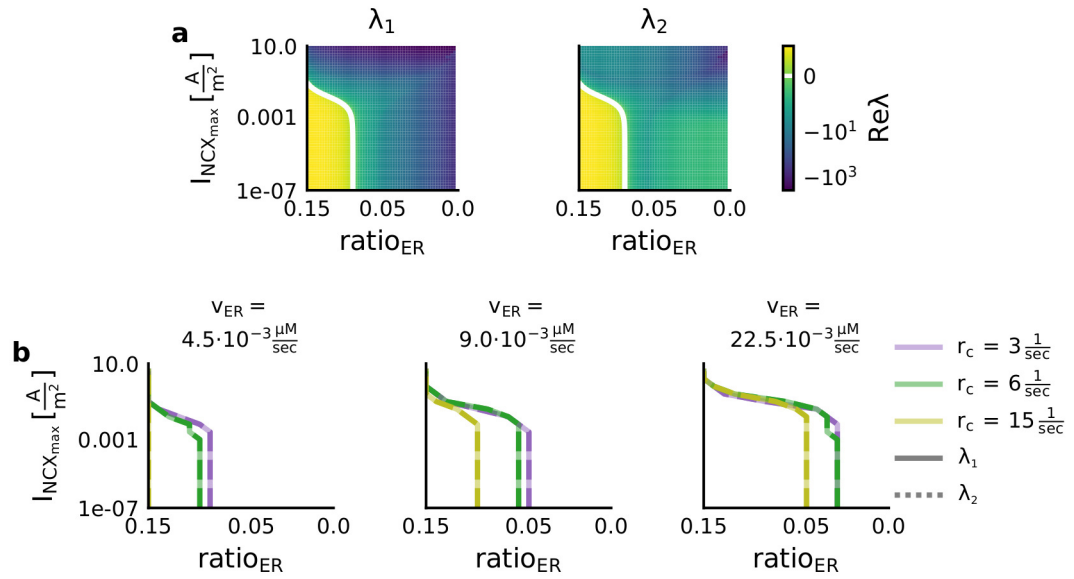


Figure 2.11: **The eigenvalues of the Jacobian matrix predict the boundary between the oscillatory and the non-oscillatory range of the reduced model.** **a** The figure shows the real part of two out of four eigenvalues ( $\lambda_1$  and  $\lambda_2$ ) of the Jacobian matrix for different values of the maximal pump current of the  $Na^+$ - $Ca^{2+}$  exchanger ( $I_{NCX_{max}}$ ) and the volume fraction of the internal  $Ca^{2+}$  store ( $ratio_{ER}$ ). The white lines denote the boundary between positive and negative values and hence also between the oscillatory and non-oscillatory range. The real parts of the other two eigenvalues are negative for all parameter combinations. **b** The figure shows the boundary between positive and negative real parts of the eigenvalues for different values of the rates for  $Ca^{2+}$  uptake ( $v_{ER}$ ) and  $Ca^{2+}$  release ( $r_c$ ) at the internal  $Ca^{2+}$  store as well as for parameter combinations of  $I_{NCX_{max}}$  and  $ratio_{ER}$ . The colored lines denote the boundaries between the positive and the negative eigenvalues for  $r_c$  equals to  $3 \frac{1}{sec}$  (grey),  $6 \frac{1}{sec}$  (green) and  $15 \frac{1}{sec}$  (yellow). The solid and dashed lines correspond to the boundaries between positive and negative values of  $\lambda_1$  and  $\lambda_2$ , respectively.

# Discussion

Within this second part of my thesis I showed that first a reduced model for calcium signal generation in astrocytes is in high accordance with the considered full model, and that second the reduced model allows a profound analytic analysis and gives in-depth insights into the model behavior.

The comparison of the full and the reduced model for calcium signal generation in astrocytes revealed that the reduced model reproduces the model behavior of the full model quite well. Both the comparisons of oscillation amplitudes and bifurcation points showed that the reduced and the full model coincide. This result illustrates that the time-dependent behavior of sodium, potassium and the membrane voltage is irrelevant for the calcium entry from the extracellular space. The calcium entry is only determined by the steady-state solutions of these variables. This dependency also emphasizes the difference of the fast time-scale of sodium, potassium and the membrane voltage and the slow time-scale of the other dynamical variables.

The mathematical structure of the reduced model allowed me to compute the fixed points and their stabilities. The reduced model consists of four differential equations describing the intracellular concentrations of calcium and  $IP_3$ , the concentration of calcium in the internal calcium store and the opening probability of calcium channels at the internal calcium store. The dependencies of the single differential equations allowed the computation of the steady-state solutions of all dynamical variables by forward-substitution. The stabilities of these fixed points were then determined by the eigenvalues of the Jacobian matrix. Thus, the reduced model allowed the derivation of the equilibrium solution of the dynamical system as well as the investigation of its steady-state behavior. Consequently, the analysis of the reduced model is much more simplified compared to the full model since it does not require the numerical simulation of the system.

Moreover, based on the reduced model I could study the two borderline cases for either a nonexistent internal calcium store or an inactive calcium entry from the extracellular space (see part 2, Model Section 1.2). In both cases the amount of considered calcium pools reduced from three to two. This reduction is accompanied by a simplification of the model. Considering the volume of the internal calcium store equals to zero also means that the intracellular calcium concentration solely depends on the calcium entry from the extracellular space. In the case of an inactive calcium entry from the extracellular space the calcium signal is only determined by calcium release from internal stores. In addition, these two mentioned borderline

cases can directly be associated with different subcellular compartments of the astrocyte. Astrocytic endfeet and perisynaptic astrocytic processes are devoid of internal calcium stores (Patrushev et al., 2013). Thus, by setting the volume of the internal calcium store equal to zero the calcium signal generation in these subcellular compartments can be studied. In the astrocytic soma the calcium release from internal stores is the predominant mechanisms for calcium signal generation (Srinivasan et al., 2015; Stobart et al., 2016; Bazargani and Attwell, 2016; Bindocci et al., 2017). This is also demonstrated by the model results showing that calcium oscillations are only observed for a high volume fraction of the internal calcium store and a low maximal pump current of the sodium-calcium exchanger. Both the high volume fraction of the internal calcium store and the low maximal pump current of the sodium-calcium exchanger are characteristic for the soma.

Based on the fixed points and their stability I could predict the model behavior in response to parameter variations. Here, I have addressed the question whether altered calcium release and uptake mechanisms at the internal calcium store can reverse the suppression of calcium oscillations during an increased calcium entry from the extracellular space (Oschmann et al., 2017b). The computed eigenvalues of the Jacobian matrix predicted that an increase of calcium transport back into the internal calcium store as well as a decrease of calcium release from internal stores led to an increase of the oscillatory range. These simulation results support the impact of store-operated calcium channels on calcium signal generation in astrocytes (Pizzo et al., 2001; Sergeeva et al., 2003). Store-operated calcium channels are in close proximity to the internal calcium store (Golovina, 2005). Depletion of internal stores activates calcium influx mediated by store-operated calcium channels and refilling of internal calcium stores (Boulay et al., 1999). In experiments it has been shown that a block of store-operated calcium entry prevents calcium oscillations in astrocytes (Pizzo et al., 2001; Sergeeva et al., 2003). Thus, although my model does not contain store-operated calcium channels I could show that a refilling of internal calcium stores is essential to sustain calcium oscillations in astrocytes.

The reduced model also serves as a general framework for the study of calcium signal generation in astrocytes. Besides the sodium driven sodium-calcium exchanger also other transporters can account for calcium entry from the extracellular space. Since most of these transporters solely depend on calcium itself (like store-operated calcium channels) or on one of the reduced dynamical variables sodium, potassium or the membrane voltage (like NMDA receptors or voltage-gated ion channels) these mechanisms can easily be applied to the reduced model without increasing its complexity. Moreover, the extension of the reduced model with these transporters still allows a profound analytic analysis. As long as the applied mathematical descriptions of the calcium transporters solely depend on calcium, the fixed point and the fixed point stability of the intracellular calcium concentration and also of all other dynamical variables can easily be computed.

In summary, I developed a reduced model for calcium signal generation in astrocytes which could serve as a general framework to investigate the interaction of calcium signaling mechanisms in astrocytes as well as the different mechanisms for calcium entry from the extracellular space. The advantages of such a reduced model are

that it allows the computation of its equilibrium solution and thus supersede a numerical integration of the dynamical system, and that based on the steady-state solution of the system predictions about the model behavior as well as about the biological system in response to parameter variations can be made.



## **Part 3**

# **Multi-compartment model for the signal propagation**



# Introduction

Calcium, sodium and potassium signals in astrocytes are not local events, but propagate through the whole astrocyte and even to neighboring astrocytes via gap junctions. The propagation of calcium, sodium and potassium signals differ in their propagation mechanisms and propagation radius. On the one side, the calcium signal propagates by both the renewal through the all-or-none-like release of calcium from internal stores as well as by calcium diffusion. On the other side, the propagation of sodium and potassium is solely driven by diffusion. This circumstance also allows calcium signals to travel larger distances than sodium and potassium signals.

The propagation of calcium signals also differs between subcellular compartments. In those subcellular compartments containing internal calcium stores, the calcium signal propagation requires the diffusion of calcium and inositol-triphosphate (IP<sub>3</sub>). The diffusion of both components then evokes an intracellular amplification of the calcium signal by calcium release from internal stores (Golovina and Blaustein, 2000; Scemes, 2000; Sheppard et al., 1997). However, perisynaptic astrocytic processes are devoid of internal calcium stores (Patrushev et al., 2013), which makes it impossible to amplify the calcium signal by intracellular mechanisms. Therefore, the propagation of calcium signals in astrocytic processes is driven by diffusion (Rusakov et al., 2011).

Moreover, calcium signals do not only spread throughout single astrocytes, but also propagate into neighboring astrocytes and by that create an intercellular calcium wave. These intercellular waves of calcium signals propagating via gap junctions spread over long distances (300 - 400  $\mu\text{m}$ ) with a speed ranging between 15-20  $\mu\text{m}/\text{s}$  and are able to excite up to hundreds of cells (Giaume and Venance, 1998; Scemes and Giaume, 2006).

In contrast to calcium signals, sodium and potassium signals are not affected by intracellular amplification and are solely driven by diffusion. Since the sodium and potassium signals spread exclusively by diffusion they propagate much faster than calcium signals. Moreover, the different subcellular compartments also play a considerable role in the propagation speed of sodium and potassium signals. For example, the diffusion speed of sodium is about 60  $\mu\text{m}/\text{s}$  in somatic regions (Langer et al., 2012), and probably even higher in astrocytic processes due to their elaborate morphology (Nedergaard et al., 2003). In astrocytic endfeet the diffusion speed is even higher and the maximum velocity is 120  $\mu\text{m}/\text{s}$  (Langer et al., 2016).

Although the propagation of the different ion signals within individual astrocytes

and astrocyte networks has already been studied, only little is known about the interaction of the individual propagating signals. For example, an interaction of sodium and calcium signals in astrocytic processes could be of great importance. Since the sodium and the calcium signals are directly linked via the sodium-calcium exchanger (Goldman et al., 1994; Kirischuk and Kettenmann, 1997; Reyes et al., 2012), the calcium signal propagation in astrocytic processes could also be driven by the fast sodium signal propagation and its effect on the sodium-calcium exchanger. In order to study the interaction of traveling ion signals in astrocytes I develop a multi-compartment model which allows to investigate the propagation of calcium, sodium and potassium signals in different subcellular compartments of the astrocyte.

# Model

The subject of this last part of my thesis is the development of a multi-compartment model for the computation of signal propagation in astrocytes. This model accounts for the movement of ions ( $\text{Ca}^{2+}$ ,  $\text{Na}^+$ ,  $\text{K}^+$ ) and molecules ( $\text{IP}_3$ ) in the astrocytic process.

## 1 Astrocyte morphology

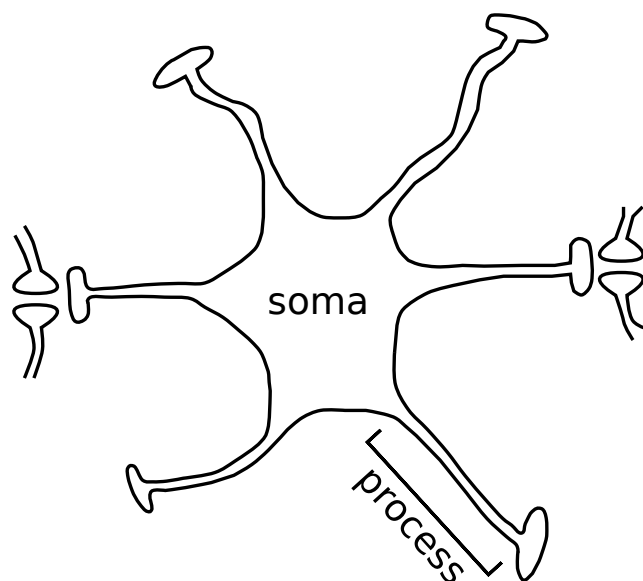


Figure 3.1: **Scheme of the astrocyte morphology.** Scheme depicting the division of astrocytes into subcellular compartments (soma and processes).

Each astrocyte consists of several subcellular compartments: one soma and several processes originating at the soma and splitting up into smaller processes (see Figure 3.1). These single subcellular compartments can be represented by basic geometric bodies. Thus, for example, a sphere represents the soma and cylinders of different lengths and diameters represent processes of different sizes.

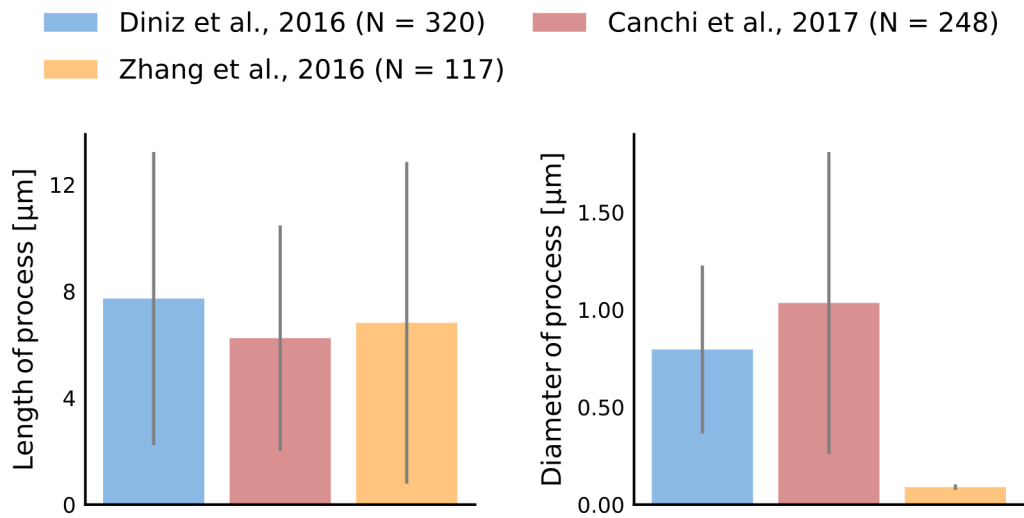


Figure 3.2: **Morphological parameters of the astrocytic process.** Mean values and the standard deviation for the length and diameter of astrocytic processes based on experimental data (Diniz et al., 2016; Canchi et al., 2017; Zhang et al., 2016).

The geometrical parameters like the length and the diameter of these subcellular compartments applied in the model are based on experimental data. Due to the fact, that more and more experimentalists pay more attention to the generation and propagation of  $\text{Ca}^{2+}$  signals in different subcellular compartments, the published results also contain detailed information about the geometry of the considered astrocytes. The geometric parameters of the processes are based on experimental data published on the open-source platform *NeuroMorpho.org* (Diniz et al., 2016; Canchi et al., 2017; Zhang et al., 2016). This platform contains publicly accessible three-dimensional reconstructions of astrocytes. Here, the morphology of each cell is given by points within a three-dimensional cartesian coordinate system. Thus, for example the length of a single astrocytic process can be obtained by summing up the euclidean distances between all points of an astrocytic process (see Figure 3.2 and Table 3.1). Noticeable is the big difference in the diameter of the processes between the individual studies. This difference could be explained by the use of different species and brain regions in the experiments. While Diniz et al. (2016) and Canchi et al. (2017) investigate astrocytes in the hippocampus of rats and mice, Zhang et al. (2016) use the corpus callosum of rabbits for their experiments. Based on the average diameter across all studies, I assume the diameter of the processes as  $1 \mu\text{m}$ . I assume the length of the process to be  $40 \mu\text{m}$  in order to be able to investigate the signal propagation along process unhindered of the ends of the process.

Table 3.1: **Morphological parameters of astrocyte.** Morphological parameters of an astrocytic process applied in the multi-compartment model.

Parameter	Value
length	40 $\mu\text{m}$
diameter	1 $\mu\text{m}$
length of single compartment	0.5 $\mu\text{m}$

In order to obtain a multi-compartment model, each subcellular compartment has to be divided into several parts. In the case of the processes, implementation is relatively simple, as the cylinder only needs to be dismantled into smaller cylinders with a shorter length and the same diameter.

Since the movement of ions and molecules in the extracellular space is also to be calculated, the extracellular space is divided into individual compartments in the same way as the intracellular space. The considered volume of the extracellular space makes up only a fraction of the volume of the intracellular space. The assumed ration between the volumes of the intra- and the extracellular space is 0.5 and is adopted from (Halnes et al., 2013).

## 2 Multi-compartment model

### 2.1 General form of the diffusion equation

The diffusion of ions and molecules within a subcellular compartment like the soma or the processes is approximated by a multi-compartment model. For this purpose the subcellular compartments are divided into a number of segments. The movement of ions and molecules within the whole subcellular compartment is then defined by the diffusion of ions and molecules between the single segments.

The movement of ions between neighboring segments is defined by the diffusion equation which consists of the product of the diffusion coefficient ( $D_{ion}$ ) and the partial derivative of the respective ion concentration:

$$diff = \frac{D_{ion}}{\lambda^2} \cdot \frac{\partial^2[ion](x, t)}{\partial x^2}. \quad (3.1)$$

Here, the diffusion coefficient is scaled by the parameter  $\lambda$ , which is a measure for the tortuosity. The diffusion coefficient is calculated relative to the cross-section areas between the individual segments. This reduces the diffusion coefficient for a smaller cross-section area and increases the coefficient for a larger cross-section area. As in the following experiments cylinders with a constant diameter are used, the diffusion constant is the same for all segments of a cylinder.

The concentration change within a single segment is determined by the sum of all ion currents carrying the respective ion ( $\sum I_{ion}$ ) multiplied with the area ( $A$ ) all currents are going through:

$$I_{comp} = A \cdot \sum I_{ion}(x, t). \quad (3.2)$$

Consequently, the change of the ion concentrations in time and space consists of the sum of the changes within a single segment as well as the ion movement between

the segments:

$$\frac{\partial[\text{ion}](x, t)}{\partial t} = \frac{A}{F \cdot \text{Vol}} \sum I_{\text{ion}}(x, t) + \frac{D_{\text{ion}}}{\lambda^2} \cdot \frac{\partial^2[\text{ion}](x, t)}{\partial x^2}. \quad (3.3)$$

Here,  $I_{\text{comp}}$  is divided by the product of the Faraday constant and the volume of the segment ( $F \cdot \text{Vol}$ ) in order to convert the current into a concentration change.

## 2.2 Time- and space-dependent changes of $\text{Ca}^{2+}$ , $\text{Na}^+$ , $\text{K}^+$ and $\text{IP}_3$

**Intracellular concentrations of  $\text{Ca}^{2+}$ ,  $\text{Na}^+$ ,  $\text{K}^+$  and  $\text{IP}_3$**  For the purpose of computing the time- and space-dependent changes of the intracellular concentrations of  $\text{Ca}^{2+}$ ,  $\text{Na}^+$ ,  $\text{K}^+$  and  $\text{IP}_3$ , I extend the differential equations for the time-dependent change within a single compartment (see Equations 1.15, 1.16, 1.17 and 1.2 in the Model Section of part 1) by the diffusion equation. The time-dependent concentration change within a single compartment is defined by the sum of those ion currents contributing to a change of the respective ion ( $\sum I_{\text{ion}}$ ). The intracellular  $\text{Ca}^{2+}$  concentration forms a special case, since it is determined by  $\text{Ca}^{2+}$  currents at the outer membrane ( $I_{\text{Ca}_M^{2+}}$ ) as well as at the internal  $\text{Ca}^{2+}$  store ( $I_{\text{Ca}_{ER}^{2+}}$ ). The intracellular concentrations of  $\text{Na}^+$  and  $\text{K}^+$  are solely defined by the sum of the respective ion currents at the plasma membrane,  $\sum I_{\text{Na}_M^+}$  and  $\sum I_{\text{K}_M^+}$ . Only the intracellular concentration of  $\text{IP}_3$  is not determined by membrane currents, but by the production ( $\text{prod}_{\text{IP}_3}$ ) and degradation ( $\text{degr}_{\text{IP}_3}$ ) of this molecule. Thus, the time- and space-dependent change of the intracellular  $\text{IP}_3$  concentration is defined by the  $\text{IP}_3$ -production and degradation as well as the diffusion of  $\text{IP}_3$  between neighboring compartments:

$$\frac{d[\text{Ca}^{2+}]_i(x, t)}{dt} = \frac{A}{F \cdot \text{Vol}_{\text{ICS}}} \cdot I_{\text{Ca}_M^{2+}} + \frac{A_{\text{ER}}}{F \cdot \text{Vol}_{\text{ICS}}} \cdot \sum I_{\text{Ca}_{ER}^{2+}} + \frac{D_{\text{Ca}^{2+}}}{\lambda^2} \cdot \frac{\partial^2[\text{Ca}^{2+}]_i(x, t)}{\partial x^2}, \quad (3.4)$$

$$\frac{d[\text{Na}^+]_i(x, t)}{dt} = \frac{A}{F \cdot \text{Vol}_{\text{ICS}}} \cdot \sum I_{\text{Na}_M^+} + \frac{D_{\text{Na}^+}}{\lambda^2} \cdot \frac{\partial^2[\text{Na}^+]_i(x, t)}{\partial x^2}, \quad (3.5)$$

$$\frac{d[\text{K}^+]_i(x, t)}{dt} = \frac{A}{F \cdot \text{Vol}_{\text{ICS}}} \cdot \sum I_{\text{K}_M^+} + \frac{D_{\text{K}^+}}{\lambda^2} \cdot \frac{\partial^2[\text{K}^+]_i(x, t)}{\partial x^2}, \quad (3.6)$$

$$\frac{d[\text{IP}_3]_i(x, t)}{dt} = \text{prod}_{\text{IP}_3} - \text{degr}_{\text{IP}_3} + \frac{D_{\text{IP}_3}}{\lambda^2} \cdot \frac{\partial^2[\text{IP}_3]_i(x, t)}{\partial x^2}. \quad (3.7)$$

The subscript  $i$  refers to the considered volume of the concentration change, the intracellular space.

**$\text{Ca}^{2+}$  concentration in the internal  $\text{Ca}^{2+}$  store** The time- and space-dependent change of the  $\text{Ca}^{2+}$  concentration in the internal  $\text{Ca}^{2+}$  store is defined in the same manner. The  $\text{Ca}^{2+}$  currents at the internal  $\text{Ca}^{2+}$  store ( $I_{\text{Ca}_{ER}^{2+}}$ ) are scaled by the area ( $A_{\text{ER}}$ ) and the volume ( $\text{Vol}_{\text{ER}}$ ) of the internal  $\text{Ca}^{2+}$  store (see Equation 1.13 in the Model Section of part 1). The diffusion of  $\text{Ca}^{2+}$  between neighboring compartments

determines the propagation of  $\text{Ca}^{2+}$  events in the internal  $\text{Ca}^{2+}$  store:

$$\frac{d[\text{Ca}^{2+}]_{ER}(x, t)}{dt} = \frac{A_{ER}}{F \cdot \text{Vol}_{ER}} \cdot \sum I_{\text{Ca}^{2+}_{ER}} + \frac{D_{\text{Ca}^{2+}}}{\lambda^2} \cdot \frac{\partial^2[\text{Ca}^{2+}]_{ER}(x, t)}{\partial x^2}. \quad (3.8)$$

**Extracellular concentration** In order to allow ion diffusion in the extracellular space, the extracellular ion concentrations are computed explicitly. In the first part of this thesis I determined the extracellular ion concentrations implicitly by linking them to the change of the respective intracellular ion concentrations (see Model Section part 1). Since this implicit computation is not sufficient for the analysis of ion diffusion in the extracellular space, an explicit computation of the extracellular ion concentration is required. I define the extracellular ion concentrations in the same way as the intracellular ion concentrations with the exceptions that the sign of the ion currents is reversed and the volume of the extracellular space ( $\text{Vol}_{ECS}$ ) differs from the volume of the intracellular space ( $\text{Vol}_{ICS}$ ):

$$\frac{d[\text{Ca}^{2+}]_o(x, t)}{dt} = \frac{A}{F \cdot \text{Vol}_{ECS}} \cdot (-I_{\text{Ca}^{2+}_M}) + \frac{D_{\text{Ca}^{2+}}}{\lambda^2} \cdot \frac{\partial^2[\text{Ca}^{2+}]_o(x, t)}{\partial x^2}, \quad (3.9)$$

$$\frac{d[\text{Na}^+]_o(x, t)}{dt} = \frac{A}{F \cdot \text{Vol}_{ECS}} \cdot (-\sum I_{\text{Na}^+}) + \frac{D_{\text{Na}^+}}{\lambda^2} \cdot \frac{\partial^2[\text{Na}^+]_o(x, t)}{\partial x^2}, \quad (3.10)$$

$$\frac{d[\text{K}^+]_o(x, t)}{dt} = \frac{A}{F \cdot \text{Vol}_{ECS}} \cdot (-\sum I_{\text{K}^+}) + \frac{D_{\text{K}^+}}{\lambda^2} \cdot \frac{\partial^2[\text{K}^+]_o(x, t)}{\partial x^2}. \quad (3.11)$$

The subscript  $o$  refers to the considered volume of the concentration change, the extracellular space.

### 2.3 Time- and space-dependent changes of the membrane potential

The spatial dependency of the membrane voltage is usually defined by the cable equation (Koch, 1999, p. 25):

$$C_m \frac{\partial V}{\partial t} = \frac{1}{2ar_L} (a^2 \cdot \frac{\partial^2 V}{\partial x^2}) - I_m + I_e. \quad (3.12)$$

The cable equation is composed of one term describing the longitudinal flow of currents ( $\frac{1}{2ar_L} (a^2 \cdot \frac{\partial^2 V}{\partial x^2})$ ), one term describing those membrane currents crossing one piece of the membrane ( $I_m$ ) and one term specifying the external input ( $I_e$ ). This first term of the cable equation consist of the second-order partial derivative of the membrane potential multiplied with the radius  $a$  and the inverse of the intracellular resistivity  $r_L$ . The currents  $I_m$  and  $I_e$  are expressed as currents per unit area. The multiplication of both currents with the surface area of the segment is canceled during the derivation of the cable equation. The parameter  $C_m$  is the specific membrane capacitance.

One of the assumptions the cable equation is based on, states that diffusive ion currents are neglected. Thus, this standard cable equation is not applicable for a model which considers diffusive currents in the intra- and extracellular space.

Instead, the time- and space-dependent change of the membrane potential can be derived from the charge density. The following derivation of the space- and time-dependent change of the membrane potential is taken from the publication of Halnes et al. (2013). The membrane of a cell functions like a parallel-plate capacitor. Proceeding from this assumption, a capacitor with capacitance  $\partial C$  separates two opposite charges ( $\partial Q$  and  $-\partial Q$ ) and by that generates a voltage difference:

$$V = \frac{\partial Q}{\partial C}. \quad (3.13)$$

The charge within a piece of membrane of length  $\partial x$  and with volume  $Vol = a^2 \pi \cdot \partial x$  is then defined by:

$$\partial Q = \rho \cdot Vol. \quad (3.14)$$

The charge can be calculated for both the intracellular space ( $\partial Q_i$ ) as well as for the extracellular space ( $\partial Q_o$ ). In this case, either the intracellular charge density ( $\rho_i$ ) or the extracellular ( $\rho_o$ ) charge density is then taken into account. For simplicity, the index  $n$  will from now on stand for both the intracellular ( $i$ ) and the extracellular case ( $o$ ).

The charge density ( $\rho_n$ ) of either the intra- or the extracellular space is composed of the sum of all ion concentrations multiplied with their valence  $z_{ion}$ :

$$\rho_n(x, t) = F \sum_{ion} z_{ion} [ion]_n(x, t). \quad (3.15)$$

The capacitance of a piece of membrane of length  $\partial x$  and with area  $A = 2\pi a \cdot \partial x$  is defined by the product of the membrane capacitance per membrane area ( $C_m$ ) and the membrane area:

$$\partial C = C_m \cdot A. \quad (3.16)$$

If one now inserts the definitions of the charge (Equation 3.14) and the capacitance (Equation 3.16) into the aforementioned equation of the membrane potential (Equation 3.13), one obtains an equation for the membrane potential based on the charge density.  $V$  can be expressed in terms of the ion concentrations in the intra- or extracellular space:

$$V = \frac{\partial Q_i}{\partial C} = \frac{\rho_i \cdot Vol_{ICS}}{C_m \cdot A} = \frac{\rho_i}{C_m \cdot SVR_{ICS}}, \quad (3.17)$$

and

$$V = -\frac{\partial Q_o}{\partial C} = \frac{\rho_o \cdot Vol_{ECS}}{C_m \cdot A} = \frac{\rho_o}{C_m \cdot SVR_{ECS}}. \quad (3.18)$$

Here, the negative sign follows from the convention, that  $V$  is positive when the intracellular space has a positive charge. Moreover, by demanding consistency between Equations 3.17 and 3.18, Halnes et al. (2013) derived the charge symmetry condition. This condition states that the charge on the inside of a piece of membrane has the same magnitude but opposite sign compared to the outside of that piece of membrane. Since the ion concentrations considered in Equations 3.17 and 3.18 are both time- and space-dependent, the resulting definition of the membrane potential has the same properties. Moreover, the diffusive currents in the intra- or extracellular space are taken into account.

### 3 Morphology of the multi-compartment model

#### 3.1 Connectivity matrix for open and sealed end condition

The partial derivatives of the diffusion term are approximated by finite differences. The partial derivative defining the concentration change between neighboring compartments is defined by:

$$\frac{\partial^2 [ion](x, t)}{\partial x^2} = \frac{[ion](x+h, t) - 2 \cdot [ion](x, t) + [ion](x-h, t)}{h^2}. \quad (3.19)$$

Thus, the concentration of an ion at a specific position and time ( $[ion](x, t)$ ) is determined by those particles entering the compartment ( $[ion](x+h, t)$  and  $[ion](x-h, t)$ ) as well as those particles leaving the compartment ( $2 \cdot [ion](x, t)$ ). All compartments have the same length,  $h$ .

For the purpose of obtaining the space-dependent partial derivative of the ion concentrations (Equation 3.19), a matrix defining the finite differences ( $D$ ) is multiplied with a vector containing the concentration of the respective ion for a specific time point and all compartments:

$$\frac{\partial [ion](x, t)}{\partial x} = \frac{D_{ion}}{\lambda^2} \cdot \overrightarrow{[ion]}(t) \cdot D, \quad (3.20)$$

with

$$D = \begin{bmatrix} -1 & 1 & 0 & 0 & \dots & 0 & 0 & 0 \\ 1 & -2 & 1 & 0 & \dots & 0 & 0 & 0 \\ 0 & 1 & -2 & 1 & \dots & 0 & 0 & 0 \\ \vdots & \vdots & \vdots & \vdots & \ddots & \vdots & \vdots & \vdots \\ 0 & 0 & 0 & 0 & \dots & 1 & -2 & 1 \\ 0 & 0 & 0 & 0 & \dots & 0 & 1 & -1 \end{bmatrix}. \quad (3.21)$$

Thus, the finite difference matrix specifies the connectivity of single compartments within an extended cell. Moreover, it also defines whether an subcellular compartment has an open or a sealed end. In case of a sealed end condition (Equation 3.21) the ends of the subcellular compartment are capped and no currents flow across the ends of the subcellular compartment. The open end condition can be thought of a cut cable without any seal of the ends. In this condition currents can flow freely out of the ends of the subcellular compartment and the extracellular solution is in direct contact with the intracellular space.

These two types of termination also result in different finite difference matrices. For the sealed end condition (Equation 3.21) the end compartments solely receive input from one neighboring compartment. This fact is represented by the number -1 instead of -2 as the first and last entries of the main diagonal. Moreover, the ending compartments give input to only one neighboring compartment, which is why the first and last entries of the main diagonal have only one adjoining field. The finite difference matrix for the open end condition (Equation 3.22) has one additional column compared to the one of the sealed end condition. This additional column

allows the consideration of currents crossing the ends of the subcellular compartment. Moreover, each compartment not only receives input from two neighboring compartments but also gives input to two neighboring compartments.

$$D = \begin{bmatrix} 1 & -2 & 1 & 0 & 0 & \dots & 0 & 0 & 0 & 0 \\ 0 & 1 & -2 & 1 & 0 & \dots & 0 & 0 & 0 & 0 \\ 0 & 0 & 1 & -2 & 1 & \dots & 0 & 0 & 0 & 0 \\ \vdots & \vdots & \vdots & \vdots & \vdots & \ddots & \vdots & \vdots & \vdots & \vdots \\ 0 & 0 & 0 & 0 & 0 & \dots & 1 & -2 & 1 & 0 \\ 0 & 0 & 0 & 0 & 0 & \dots & 0 & 1 & -2 & 1 \end{bmatrix}. \quad (3.22)$$

### 3.2 Connectivity matrix for a branching process

With the intention of creating structures which represent the astrocyte geometry, single subcellular compartments are combined. As a basic structure I choose the branching of one process into two smaller processes. The connections between the individual subcellular compartments are defined using a Hines matrix (Hines, 1984). Prerequisite for the creation of a Hines matrix is that the individual compartments of a branch are numbered continuously (see Figure 3.3). The structure of the matrix itself is similar to the one of the connectivity matrix: each entry of the matrix corresponds to a connection between two compartments. The continuous numbering of all compartments now allows a branching or connection of subcellular compartments like two processes. The following figure is intended to illustrate the structure of the Hines matrix for a simplified branching. Here, each process solely consists of three compartments.

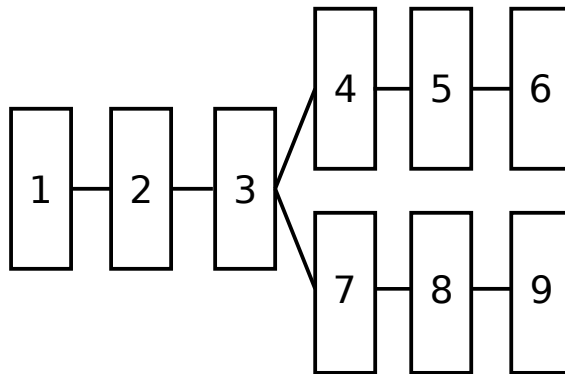


Figure 3.3: **Scheme of a branching process.** Scheme depicting the division of a branching astrocytic process into single compartments of the multi-compartment model.

$$D = \begin{bmatrix} D_{1,1} & D_{1,2} & 0 & 0 & 0 & 0 & 0 & 0 & 0 \\ D_{2,1} & D_{2,2} & D_{2,3} & 0 & 0 & 0 & 0 & 0 & 0 \\ 0 & D_{3,2} & D_{3,3} & D_{3,4} & 0 & 0 & D_{3,7} & 0 & 0 \\ 0 & 0 & D_{4,3} & D_{4,4} & D_{4,5} & 0 & 0 & 0 & 0 \\ 0 & 0 & 0 & D_{5,4} & D_{5,5} & D_{5,6} & 0 & 0 & 0 \\ 0 & 0 & 0 & 0 & D_{6,5} & D_{6,6} & 0 & 0 & 0 \\ 0 & 0 & D_{7,3} & 0 & 0 & 0 & D_{7,7} & D_{7,8} & 0 \\ 0 & 0 & 0 & 0 & 0 & 0 & D_{8,7} & D_{8,8} & D_{8,9} \\ 0 & 0 & 0 & 0 & 0 & 0 & 0 & D_{9,8} & D_{9,9} \end{bmatrix}. \quad (3.23)$$

## 4 Model parameter values

The following table shows those parameters, which were introduced within this third part. All other parameter values are taken from the first part of the thesis.

Some of these parameters are obtained during parameter explorations. The corresponding figures can be found in the Results Section.

Unless otherwise stated, the default parameter values mentioned here are used in all subsequent simulations.

Table 3.2: Parameters for the propagation of  $\text{Ca}^{2+}$ ,  $\text{Na}^+$ ,  $\text{IP}_3$  and  $\text{K}^+$ .

Paramet	Value	Source
$D_{\text{Ca}^{2+}}$	$5 \cdot 10^{-11} \frac{\text{m}^2}{\text{sec}}$	see Results Section
$D_{\text{IP}_3}$	$5 \cdot 10^{-12} \frac{\text{m}^2}{\text{sec}}$	see Results Section
$D_{\text{Na}^+}$	$1.33 \cdot 10^{-9} \frac{\text{m}^2}{\text{sec}}$	Qian and Sejnowski (1989)
$D_{\text{K}^+}$	$1.96 \cdot 10^{-9} \frac{\text{m}^2}{\text{sec}}$	Qian and Sejnowski (1989)
$\lambda_i$	3.2	Halnes et al. (2013)
$\lambda_o$	1.6	Halnes et al. (2013)
$I_{\text{Glut}_{max}}$	$6.8 \frac{\text{A}}{\text{m}^2}$	see Results Section
$I_{\text{NKA}_{max}}$	$5.8 \frac{\mu\text{A}}{\text{m}^2}$	see Results Section

Table 3.3: Morphological parameters of the multi-compartment model.

Paramet	Value
$\text{SVR}_{\text{ICS}}$	$4 \frac{1}{\mu\text{m}}$
$\text{SVR}_{\text{ECS}}$	$8 \frac{1}{\mu\text{m}}$
$\text{SVR}_{\text{ER}}$	$10.32 \frac{1}{\mu\text{m}}$
$\text{ratio}_{\text{ER}}$	0.15



# Results

Subject of the results section is first the parametrization of the multi-compartment model, followed by the analysis of the multi-compartment model. As it has been shown in the first and second part of this thesis the  $\text{Ca}^{2+}$  and  $\text{Na}^+$  dynamics act independently of each other. Therefore, I first investigate those model parameters shaping the propagation of the  $\text{Na}^+$  signal. Then, I perform the model parametrization for the  $\text{Ca}^{2+}$  propagation. Subsequently, I study the propagation and interaction of the  $\text{Ca}^{2+}$  and  $\text{Na}^+$  dynamics in single astrocytic processes with either a sealed or an open end, in branching astrocytic processes and at the perisynaptic astrocytic process.

## 1 $\text{Na}^+$ diffusion in astrocytic processes

First, I parameterize the multi-compartment model in order to fit the propagation of the  $\text{Na}^+$  signals to experimental data. As it has already been shown in the first and second part of the thesis, the  $\text{Na}^+$  dynamics act almost independently of the  $\text{Ca}^{2+}$  dynamics. Therefore, I determine the parameter set for the propagation of the  $\text{Na}^+$  signals considering solely the dynamics of  $\text{Na}^+$ ,  $\text{K}^+$  and the membrane voltage ( $V$ ) at the outer membrane. The dynamics of  $\text{Na}^+$ ,  $\text{K}^+$  and  $V$  are determined by the glutamate transporter (GluT), the  $\text{Na}^+$ - $\text{K}^+$  pump as well as the  $\text{Na}^+$  and  $\text{K}^+$  leak currents. The  $\text{Ca}^{2+}$  dynamics at the outer membrane or the internal  $\text{Ca}^{2+}$  store are neglected. Moreover, as the  $\text{Na}^+$  diffusion coefficient is known from experiments (Qian and Sejnowski, 1989), I solely investigate the effect of the maximal pump currents of the glutamate transporter ( $I_{\text{GluTmax}}$ ) and the  $\text{Na}^+$ - $\text{K}^+$  pump ( $I_{\text{NKAmx}}$ ) on the  $\text{Na}^+$  propagation by a parameter exploration. For these parameter explorations, I study the  $\text{Na}^+$  signal propagation along a cylinder with a length of  $40 \mu\text{m}$ , a diameter of  $1 \mu\text{m}$  and with sealed ends. As a stimulus for the parameter exploration, I choose to stimulate the middle compartment of the astrocytic process with a constant glutamate concentration of  $1 \text{ mM}$  for a duration of  $0.5 \text{ second}$ .

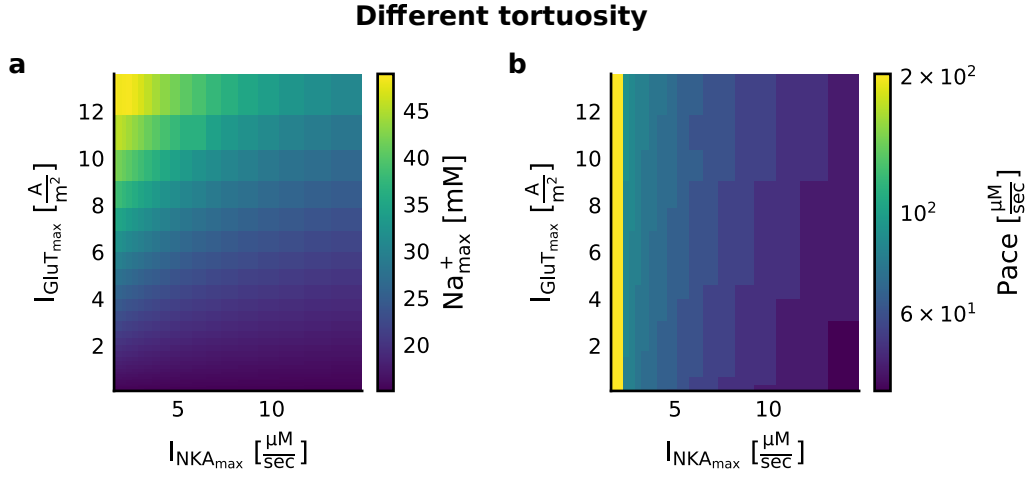


Figure 3.4: **Amplitude and pace of the Na<sup>+</sup> signal propagation within an astrocytic process for different values of the maximal pump currents of the glutamate transporter ( $I_{\text{GluT}_{\text{max}}}$ ) and the Na<sup>+</sup>-K<sup>+</sup> pump ( $I_{\text{NKA}_{\text{max}}}$ ).** An astrocytic process with the length of 40  $\mu\text{m}$ , diameter of 1  $\mu\text{m}$  and sealed ends is stimulated in the middle compartment (length: 0.5  $\mu\text{m}$ ) with a constant glutamate concentration of 1 mM for a duration of 0.5 seconds. The tortuosities of the intra- and extracellular space are set to their default values. **a** The maximal amplitude of the Na<sup>+</sup> signal at the stimulation site for parameter combinations of the maximal pump currents of the glutamate transporter ( $I_{\text{GluT}_{\text{max}}}$ ) and the Na<sup>+</sup>-K<sup>+</sup> pump ( $I_{\text{NKA}_{\text{max}}}$ ). **b** The pace of the Na<sup>+</sup> signal propagation for parameter combinations of maximal pump currents of the glutamate transporter ( $I_{\text{GluT}_{\text{max}}}$ ) and the Na<sup>+</sup>-K<sup>+</sup> pump ( $I_{\text{NKA}_{\text{max}}}$ ). The pace is determined by the amplitude and the traveled distance of the Na<sup>+</sup> signal within the first 100 milliseconds after the begin of the stimulation.

First, I study the Na<sup>+</sup> signal propagation assuming the default values for the tortuosity of the intra- and extracellular space ( $\lambda_i = 3.2$ ,  $\lambda_o = 1.6$ ). In this case, both a high activity of the glutamate transporter and a low activity of the Na<sup>+</sup>-K<sup>+</sup> pump enhance the amplitude of the Na<sup>+</sup> signal (see Figure 3.4 a). The glutamate transporter mediates the cotransport of glutamate together with three Na<sup>+</sup> ions. Thus, the higher the maximal pump activity of the glutamate transporter ( $I_{\text{GluT}_{\text{max}}}$ ) is, the more Na<sup>+</sup> is transported into the cell. The Na<sup>+</sup>-K<sup>+</sup> pump counteracts the glutamate transporter by transporting Na<sup>+</sup> out of the cell. Therefore, a low activity of the Na<sup>+</sup>-K<sup>+</sup> pump favors the accumulation of Na<sup>+</sup> within the astrocyte. The propagation speed of the Na<sup>+</sup> signal is mainly determined by the activity of the Na<sup>+</sup>-K<sup>+</sup> pump and decreases with an increase of the maximal pump current of the Na<sup>+</sup>-K<sup>+</sup> pump (see Figure 3.4 b). Since the subcellular compartment is only stimulated at one point in the middle, the glutamate transporter, which transports Na<sup>+</sup> into the cell, has only a small effect on the propagation speed. The strength of the Na<sup>+</sup>-K<sup>+</sup> pump, however, does not only determine the amplitude of the Na<sup>+</sup> signal, but also the propagation speed. A low maximal pump current of the Na<sup>+</sup>-K<sup>+</sup> pump favors a high amplitude and a high propagation speed, as less Na<sup>+</sup> is pumped out of the cell.

According to experimental results, the amplitude of the Na<sup>+</sup> signal at the stimulation site is between 25 and 30 mM and the propagation speed within an astrocytic process is around 60  $\frac{\mu\text{m}}{\text{sec}}$  (Langer et al., 2012). In comparison to these experimental results I

choose the values for the maximal pump currents to be  $I_{\text{GluT}_{\text{max}}} = 6.8 \frac{\text{A}}{\text{m}^2}$  and  $I_{\text{NKA}_{\text{max}}} = 5.8 \cdot 10^{-6} \frac{\text{A}}{\text{m}^2}$ .

Interestingly, assuming the same tortuosity in the intra- and extracellular ( $\lambda_i = \lambda_o = 3.2$ ) space changes the speed of the  $\text{Na}^+$  signal propagation, but not the amplitude of the signal. The tortuosity scales the diffusion coefficient. Thus, by assuming different values for the tortuosity in the intra- and extracellular space, the diffusion coefficients of the intra- and extracellular space differ as well. In contrast, assuming the same tortuosity in the intra- and extracellular space also results in the same diffusion coefficients. In this case the maximal pump activities of the glutamate transporter and the  $\text{Na}^+$ - $\text{K}^+$  pump have no influence on the propagation speed, the propagation speed is the same for all parameter combinations (see Figure 3.5 b). The amplitude of the  $\text{Na}^+$  signal, however, is not affected by variations of the tortuosity. The impact of the membrane transporters during conditions assuming either the same or different tortuosities will be explained in detail in a following section.

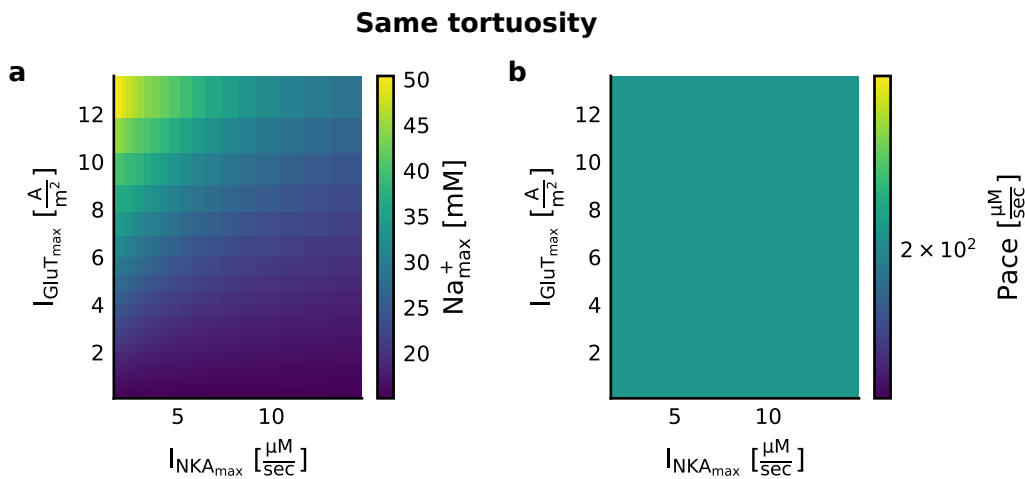


**Figure 3.5: Amplitude and pace of the  $\text{Na}^+$  signal propagation within an astrocytic process assuming the same tortuosity ( $\lambda_i = \lambda_o = 3.2$ ) in the intra- and extracellular space for different values of the maximal pump currents of the glutamate transporter ( $I_{\text{GluT}_{\text{max}}}$ ) and the  $\text{Na}^+$ - $\text{K}^+$  pump ( $I_{\text{NKA}_{\text{max}}}$ ).** An astrocytic process with the length of  $40 \mu\text{m}$ , diameter of  $1 \mu\text{m}$  and sealed ends is stimulated in the middle compartment (length:  $0.5 \mu\text{m}$ ) with a constant glutamate concentration of  $1 \text{mM}$  for a duration of  $0.5$  seconds. **a** The maximal amplitude at the stimulation site for parameter combinations of the maximal pump currents of the glutamate transporter ( $I_{\text{GluT}_{\text{max}}}$ ) and the  $\text{Na}^+$ - $\text{K}^+$  pump ( $I_{\text{NKA}_{\text{max}}}$ ). **b** The pace of the  $\text{Na}^+$  signal propagation for parameter combinations of maximal pump currents of the glutamate transporter ( $I_{\text{GluT}_{\text{max}}}$ ) and the  $\text{Na}^+$ - $\text{K}^+$  pump ( $I_{\text{NKA}_{\text{max}}}$ ). The pace is determined by the amplitude and the traveled distance of the  $\text{Na}^+$  signal within the first  $100$  milliseconds after the begin of the stimulation.

Moreover, the consideration of either different or the same tortuosities in the intra- and extracellular space determines whether the  $\text{Na}^+$  concentration undershoots its resting concentration. Assuming different tortuosities in the intra- and extracellular space, the  $\text{Na}^+$  signal undershoots the  $\text{Na}^+$  resting concentration at a distance of about  $10 \mu\text{m}$  from the stimulation site (see Figure 3.6 a and Figure 3.7 a). In case of the same tortuosities in the intra- and extracellular space, however, I

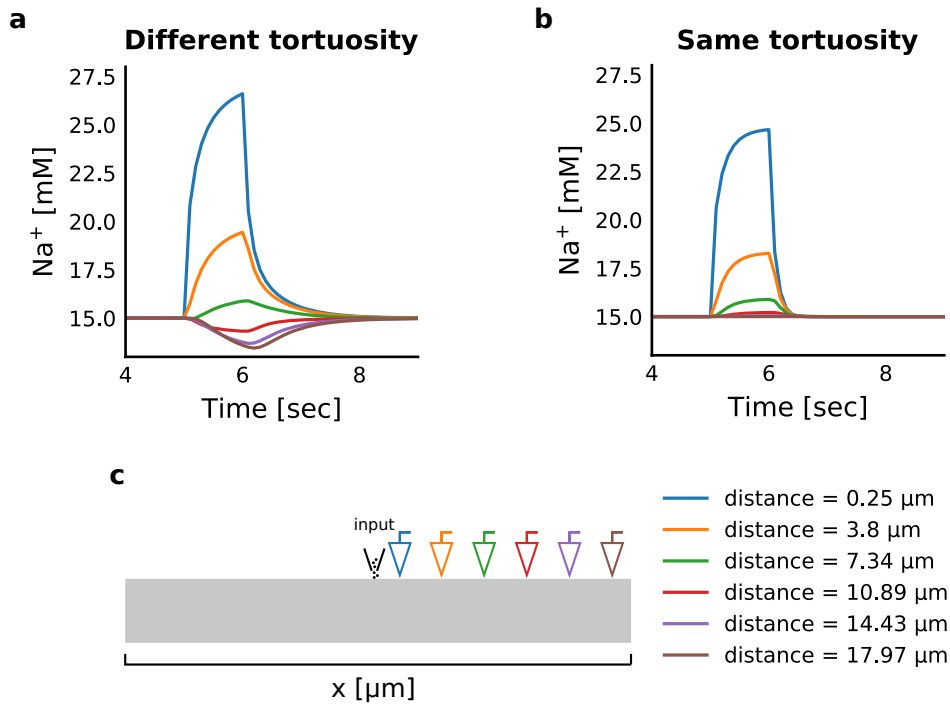


Figure 3.6: **The propagation of  $\text{Na}^+$  along the astrocytic process for the chosen parameter combination of the maximal pump currents of the glutamate transporter and the  $\text{Na}^+$ - $\text{K}^+$  pump.** The stimulated astrocytic process has a length of  $40 \mu\text{m}$ , a diameter of  $1 \mu\text{m}$  and sealed ends. The process is stimulated in the middle compartment (length:  $0.5 \mu\text{m}$ ) with a constant glutamate concentration of  $1 \text{ mM}$  for a duration of  $0.5$  seconds. **a** The time course of the  $\text{Na}^+$  concentration shown for six different distances from the stimulation site along the astrocytic process. In this case, the tortuosities in the intra- and extracellular space are set to their default values. **b** The time course of the  $\text{Na}^+$  concentration shown for six different distances from the stimulation site along the astrocytic process. In this case, the tortuosities in the intra- and extracellular space are the same ( $\lambda_i = \lambda_o = 3.2$ ). **c** Scheme depicting the stimulation and recording sites along the astrocytic process.

do not observe this phenomenon and the  $\text{Na}^+$  signal never undershoots the  $\text{Na}^+$  resting concentration (see Figure 3.6 b and Figure 3.7 b). This observed effect can be explained by comparing the transmembrane and diffusive fluxes for these two conditions (see Figure 3.8). When comparing the difference of the diffusive fluxes for either assuming a different or a same tortuosity ( $J_{D_{\text{Na}}\text{diff}} - J_{D_{\text{Na}}\text{same}}$ ) huge differences between the strength of the diffusive fluxes around the stimulation site can be observed (see Figure 3.8 b). In case of different tortuosities, the diffusive flux in the intracellular space is weaker around the stimulation site compared to the diffusive fluxes for same tortuosities (see Figure 3.8 b (left)). Moreover, the diffusive flux in the extracellular space for different tortuosities is higher around the stimulation site compared to the diffusive flux for same tortuosities (see Figure 3.8 b (right)). These results suggest that in the intracellular space in case of different tortuosities less  $\text{Na}^+$  diffuses to neighboring compartments. This also results in a higher amplitude of the  $\text{Na}^+$  signal (see Figure 3.8 a (left)). At the same time in the extracellular space the diffusive flux around the stimulation site is way higher for different tortuosities compared to same tortuosities (see Figure 3.8 b (right)). Thus, in case of different

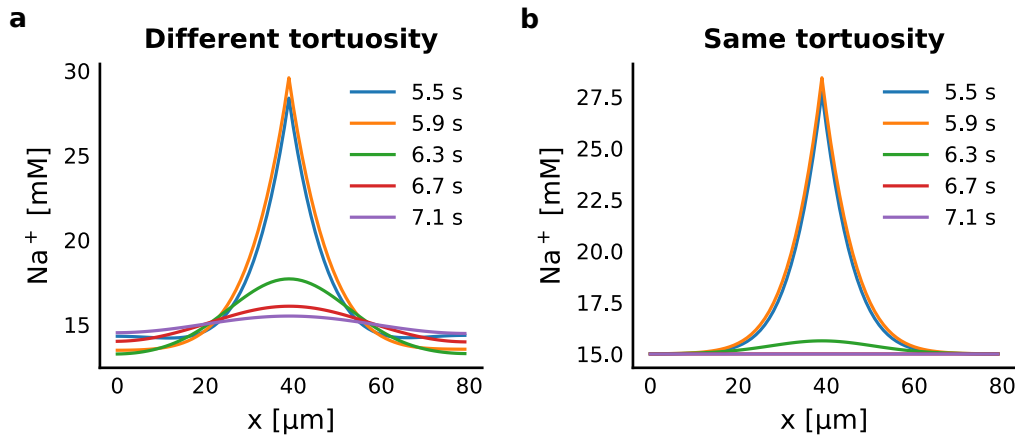


Figure 3.7: **The propagation of the  $\text{Na}^+$  signal along the astrocytic process for the chosen parameter combination of the maximal pump currents of the glutamate transporter and the  $\text{Na}^+$ - $\text{K}^+$  pump.** The stimulated astrocytic process has a length of  $40 \mu\text{m}$ , a diameter of  $1 \mu\text{m}$  and sealed ends. The process is stimulated in the middle compartment (length:  $0.5 \mu\text{m}$ ) with a constant glutamate concentration of  $1 \text{ mM}$  for a duration of  $0.5$  seconds. **a** The spatial profile of the  $\text{Na}^+$  concentration along the astrocytic process shown for five different time points after the start of the stimulation. In this case, the tortuosities in the intra- and extracellular space are set to their default values. **b** The time course of the  $\text{Na}^+$  concentration along the astrocytic process shown for five different time points after the start of the stimulation. In this case, the tortuosity in the intra- and extracellular space are the same ( $\lambda_i = \lambda_o = 3.2$ ).

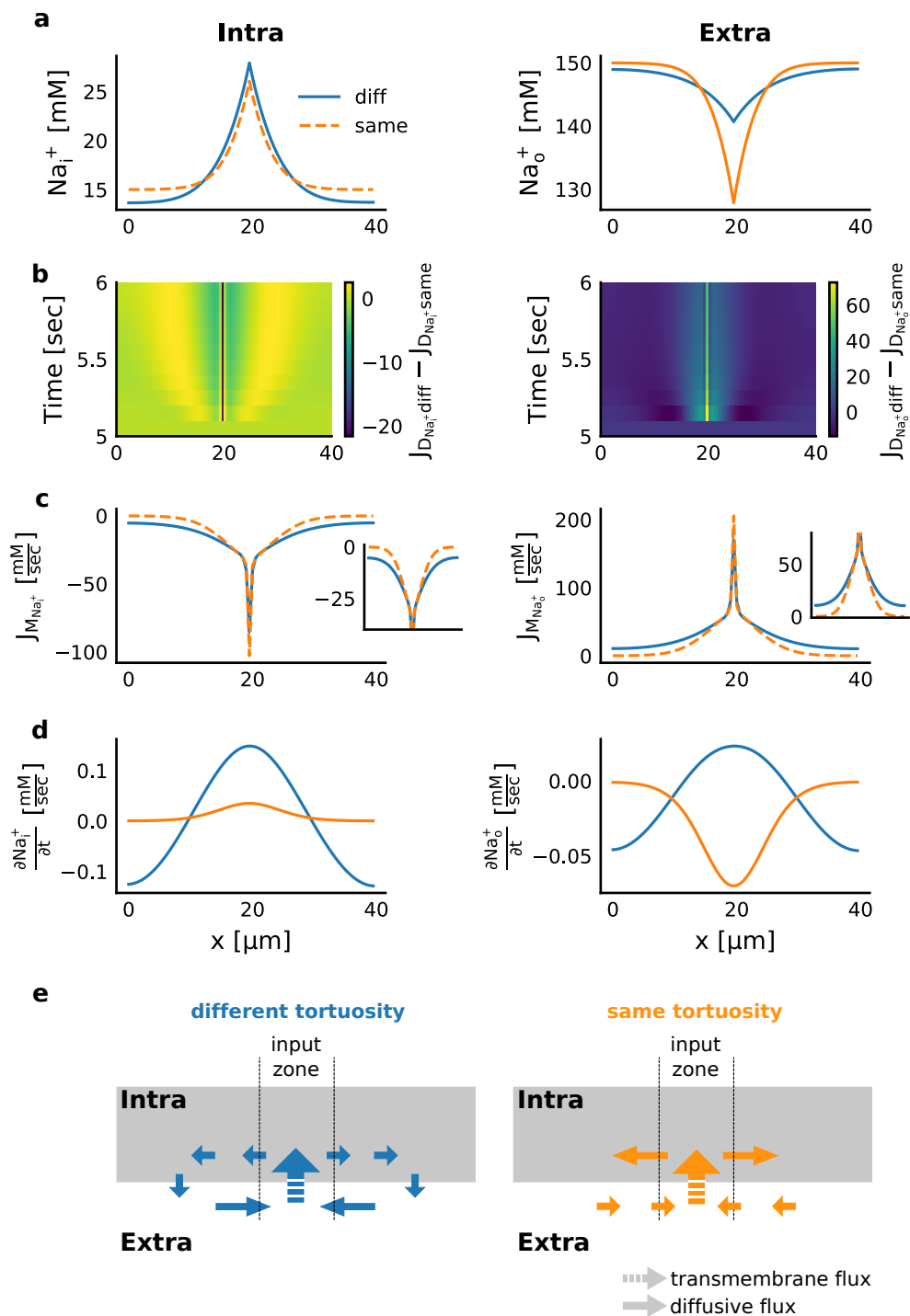
tortuosities this imbalance between diffusive fluxes in the intra- and extracellular space leads to a high efflux of  $\text{Na}^+$  from the intracellular space (see Figure 3.8 c). This high  $\text{Na}^+$  efflux is also illustrated by the time derivatives of the  $\text{Na}^+$  concentration in the intra- and extracellular space ( $\frac{\partial N_{a_i^+}}{\partial t}$  and  $\frac{\partial N_{a_o^+}}{\partial t}$ ) (see Figure 3.8 d). With additional consideration of the equation for the time derivative of the  $\text{Na}^+$  concentration in the intra- and extracellular space, it becomes clear that whenever the time derivative is negative the transmembrane flux is stronger than the diffusive flux and  $\text{Na}^+$  is transported out of the cell. Moreover, the weaker diffusive flux of  $\text{Na}^+$  for different tortuosities within the extracellular space is also illustrated very well by the time derivatives (see Figure 3.8 d (right)). In summary, for different tortuosities the  $\text{Na}^+$  diffusion in the extracellular space is too strong compared to the one of the intracellular space and pulls  $\text{Na}^+$  out of the cell. In case of the same tortuosity in the intra- and extracellular space, the  $\text{Na}^+$  diffusion in both spaces is the same and no imbalance occurs. Moreover, as during this condition no  $\text{Na}^+$  crosses the membrane, except at the stimulation site, the membrane transporters do not affect the  $\text{Na}^+$  signal propagation (see Figure 3.5).

In summary, the  $\text{Na}^+$  signal amplitude increases with an increasing maximal pump current of the glutamate transporter and a decreasing maximal pump current of the  $\text{Na}^+$ - $\text{K}^+$  pump (see Figure 3.4). Moreover, the maximal pump current of the  $\text{Na}^+$ - $\text{K}^+$  pump mainly determines the propagation speed of the  $\text{Na}^+$  signal as it transports  $\text{Na}^+$  out of the cell along the astrocytic process. Also the tortuosity of the intra- and extracellular space affect the  $\text{Na}^+$  signal propagation (see Figure 3.5). In case of assuming the same tortuosity in the intra- and extracellular space, the  $\text{Na}^+$  signal

propagates with a speed of  $200 \frac{\mu M}{sec}$  independent of the maximal pump currents of the glutamate transporter or the  $Na^+ - K^+$  pump. In addition, the tortuosity determines the occurrence of an undershoot of the  $Na^+$  concentration due to changes in the  $Na^+$  diffusion in the intra- and extracellular space (see Figure 3.8).

---

Figure 3.8 (*facing page*): **Effect of the tortuosity on the  $Na^+$  diffusion in the intra- and extracellular space.** Spatial profiles of the  $Na^+$  concentration, the diffusion fluxes, the transmembrane fluxes and the time derivative of the  $Na^+$  concentration for either assuming different (blue lines) or same (dashed orange lines, here:  $\lambda_i = \lambda_o = 3.2$ ) tortuosities in the intra- and extracellular space. The stimulated astrocytic process has a length of  $40 \mu m$ , a diameter of  $1 \mu m$ , sealed ends and is stimulated in the middle compartment (length:  $0.5 \mu m$ ) for a duration of 0.5 seconds. All curves are shown for the time of stimulus offset (5.5 seconds). This corresponds to the same time points for stimulus onset and offset as in Figure 3.6. **a** Traces depicting the spatial profile of the  $Na^+$  concentration in the intracellular (left) and in the extracellular space (right). **b** Spatial profile of the difference between diffusive fluxes for either assuming different or same tortuosities ( $J_{D_{Na^+} diff} - J_{D_{Na^+} same}$ ) in the interval between stimulus onset (5 seconds) and 0.5 seconds after stimulus offset (6 seconds). The differences are shown for the intracellular (left) and the extracellular space (right). **c** Spatial profile of the transmembrane  $Na^+$  flux in the intracellular (left) and in the extracellular space (right). **d** Spatial profile of the time derivative of the  $Na^+$  concentration in the intracellular (left) and in the extracellular space (right). **e** Scheme illustrating the transmembrane as well as the diffusive  $Na^+$  flux either assuming a different or the same tortuosity.



## 2 $\text{Ca}^{2+}$ signal propagation within an astrocytic process

For the purpose of investigating the  $\text{Ca}^{2+}$  signal propagation along the astrocytic process, I first study the  $\text{Ca}^{2+}$  dynamics in isolation for different combinations of the diffusion coefficients of  $\text{Ca}^{2+}$  and  $\text{IP}_3$ . An exclusive study of the  $\text{Ca}^{2+}$  dynamics includes solely the release of  $\text{Ca}^{2+}$  from internal stores. The  $\text{Ca}^{2+}$  entry from the extracellular space as well as the  $\text{Na}^+$  and  $\text{K}^+$  dynamics are neglected. As a next step, I investigate the interaction between the  $\text{Na}^+$  and the  $\text{Ca}^{2+}$  signal propagation. Thereby I mainly focus on how the maximal pump currents of the membrane transporters influence the  $\text{Ca}^{2+}$  signal propagation.

For these parameter explorations, I study the  $\text{Ca}^{2+}$  signal propagation along a cylinder with a length of  $40 \mu\text{m}$ , a diameter of  $1 \mu\text{m}$  and with sealed ends. As a stimulus for the parameter exploration, I choose to stimulate the astrocytic process with a constant glutamate concentration of  $1 \text{ mM}$  for a duration of  $100 \text{ seconds}$ . Here, I assume the default values for the tortuosity of the intra- and extracellular space.

First, I study the impact of the diffusion coefficients of  $\text{Ca}^{2+}$  and  $\text{IP}_3$  on the  $\text{Ca}^{2+}$  signal propagation (see Figure 3.9). Since  $\text{IP}_3$  is known to drive the  $\text{Ca}^{2+}$  signal propagation and favors the renewal of the signal at the internal  $\text{Ca}^{2+}$  store, the diffusion coefficient of  $\text{IP}_3$  plays a central role in the  $\text{Ca}^{2+}$  signal propagation and is therefore subject of the parameters exploration. The  $\text{Ca}^{2+}$  signal propagation is examined by means of the maximal reached  $\text{Ca}^{2+}$  oscillation frequency, the oscillation propagation radius and the oscillation amplitude (see Figure 3.9).

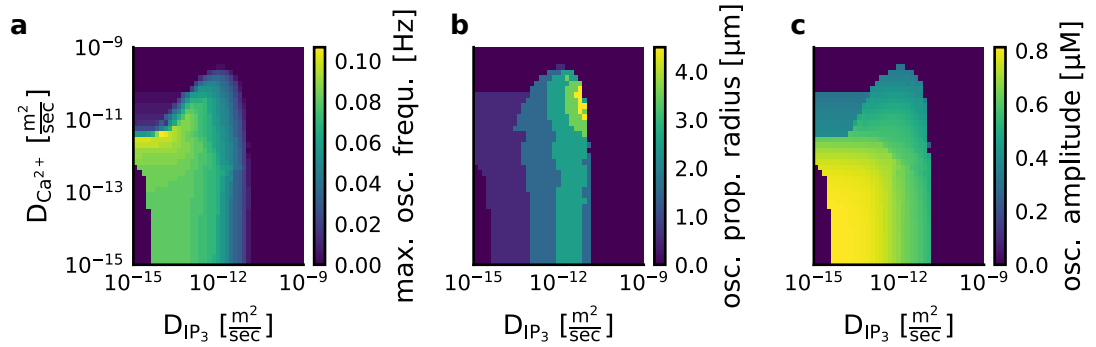


Figure 3.9:  $\text{Ca}^{2+}$  signal propagation as a function of the  $\text{IP}_3$  and  $\text{Ca}^{2+}$  diffusion coefficients. Maximal frequency, propagation radius and amplitude of the  $\text{Ca}^{2+}$  oscillations for different combinations of the  $\text{IP}_3$  and  $\text{Ca}^{2+}$  diffusion coefficients. The  $\text{Ca}^{2+}$  oscillation propagation is studied along an astrocytic process with the length of  $40 \mu\text{m}$ , diameter of  $1 \mu\text{m}$  and sealed ends. The middle compartment (compartment length =  $0.5 \mu\text{m}$ ) is stimulated for a duration of  $100 \text{ seconds}$  with a constant glutamate concentration of  $1 \text{ mM}$  glutamate. The tortuosities of the intra- and extracellular space are set to their default values. **a** The maximal observed  $\text{Ca}^{2+}$  oscillation frequency for parameter combinations of the diffusion coefficients of  $\text{IP}_3$  and  $\text{Ca}^{2+}$ . **b** Propagation radius of the  $\text{Ca}^{2+}$  oscillations for parameter combinations of the diffusion coefficients of  $\text{IP}_3$  and  $\text{Ca}^{2+}$ . **c** Amplitude of the  $\text{Ca}^{2+}$  oscillations for parameter combinations of the diffusion coefficients of  $\text{IP}_3$  and  $\text{Ca}^{2+}$ .

The parameter exploration reveals that moderate values of both the  $\text{Ca}^{2+}$  diffusion coefficient ( $D_{\text{Ca}^{2+}}$ :  $10^{-15} \frac{\text{m}^2}{\text{sec}}$  -  $10^{-10} \frac{\text{m}^2}{\text{sec}}$ ) and the  $\text{IP}_3$  diffusion coefficient ( $D_{\text{IP}_3}$ :

$10^{-14} \frac{m^2}{sec} - 10^{-14} \frac{m^2}{sec}$ ) allow the generation and propagation of  $Ca^{2+}$  oscillations. The maximal oscillation frequency and the oscillation amplitude decrease with increasing values of both diffusion coefficients (see Figure 3.9 a and b). As the figure shows, primarily high values of the  $D_{IP_3}$  seem to suppress the generation of  $Ca^{2+}$  oscillations. Since  $IP_3$  has no blocking effect on the receptor channels at the internal  $Ca^{2+}$  store, I assume that the fast diffusion of  $IP_3$  leads to a  $Ca^{2+}$  release at several locations simultaneously along the internal store. As a result, the internal  $Ca^{2+}$  store is depleted and the oscillations are suppressed. Thus, the higher  $D_{IP_3}$  is, the more receptors along the internal  $Ca^{2+}$  store are simultaneously activated, which leads to a lower amplitude of the oscillations (see Figure 3.9 c). In contrast, low values of  $D_{IP_3}$  lead to a too slow propagation of  $IP_3$  signals, so that less  $IP_3$  receptors are activated along the astrocytic process and the  $Ca^{2+}$  release from internal stores is too low to generate  $Ca^{2+}$  oscillations.

As a next step, I investigate the impact of the membrane transporters (glutamate transporter,  $Na^+$ - $K^+$  pump and  $Na^+$ - $Ca^{2+}$  exchanger) on the  $Ca^{2+}$  signal propagation (see Figures 3.10, 3.11 and 3.12). Here, each figure shows the model behavior in response to parameter variations of the maximal pump currents of the glutamate transporter ( $I_{GluT_{max}} = [4.8 \frac{A}{m^2}, 6.8 \frac{A}{m^2}, 8.8 \frac{A}{m^2}]$ ) and the  $Na^+$ - $K^+$  pump ( $(I_{NKA_{max}}) = [4.8 \cdot 10^{-6} \frac{A}{m^2}, 5.8 \cdot 10^{-6} \frac{A}{m^2}, 6.8 \cdot 10^{-6} \frac{A}{m^2}]$ ). The three different figures (3.10, 3.11 and 3.12) illustrate the model behavior for three different values of the maximal pump current of the  $Na^+$ - $Ca^{2+}$  exchanger ( $I_{NCX_{max}} = [0.0001 \frac{A}{m^2}, 0.001 \frac{A}{m^2}, 0.01 \frac{A}{m^2}]$ ). In general, I observe that an increase of the glutamate transporter activity ( $I_{GluT_{max}}$ ) enhances both the  $Ca^{2+}$  oscillation frequency and the  $Ca^{2+}$  oscillation propagation radius (see Figure 3.10). Moreover, too high values of the maximal pump current of the glutamate transporter ( $I_{GluT_{max}}$ ) lead to a suppression of the  $Ca^{2+}$  oscillations and solely an increase of the intracellular  $Ca^{2+}$  concentration can be observed (see Figures 3.10 or 3.11). The amplitude of this intracellular  $Ca^{2+}$  raise increases with increasing maximal pump current of the glutamate transporter ( $I_{GluT_{max}}$ ) due to the enhanced  $Na^+$  accumulation within the intracellular space. While the maximal pump activity of the  $Na^+$ - $K^+$  pump ( $I_{NKA_{max}}$ ) has a relatively small effect on the frequency and the propagation radius of the  $Ca^{2+}$  oscillations (see Figures 3.10 and 3.11), it is decisive for the amplitude of the intracellular  $Ca^{2+}$  raise. The activity of the  $Na^+$ - $Ca^{2+}$  exchanger ( $I_{NCX_{max}}$ ), however, strongly affects the  $Ca^{2+}$  signal propagation and suppresses the  $Ca^{2+}$  oscillation generation and propagation for high values of its maximal pump activity ( $I_{NCX_{max}} > 0.001 \frac{A}{m^2}$ ) (see Figures 3.11 or 3.12). In summary, the isolated study of the  $Ca^{2+}$  signal propagation reveals that moderate values of the diffusion coefficients of  $Ca^{2+}$  and  $IP_3$  allow the generation and propagation of  $Ca^{2+}$  oscillations (see Figure 3.9). The analysis of the  $Ca^{2+}$  signal propagation in combination with the  $Na^+$  signal propagation reveals that primarily the glutamate transporter and the  $Na^+$ - $Ca^{2+}$  exchanger affect the  $Ca^{2+}$  signal propagation (see Figures 3.10, 3.11 or 3.12). Too high values of the maximal pump currents of both transporters suppress the  $Ca^{2+}$  signal generation and propagation.

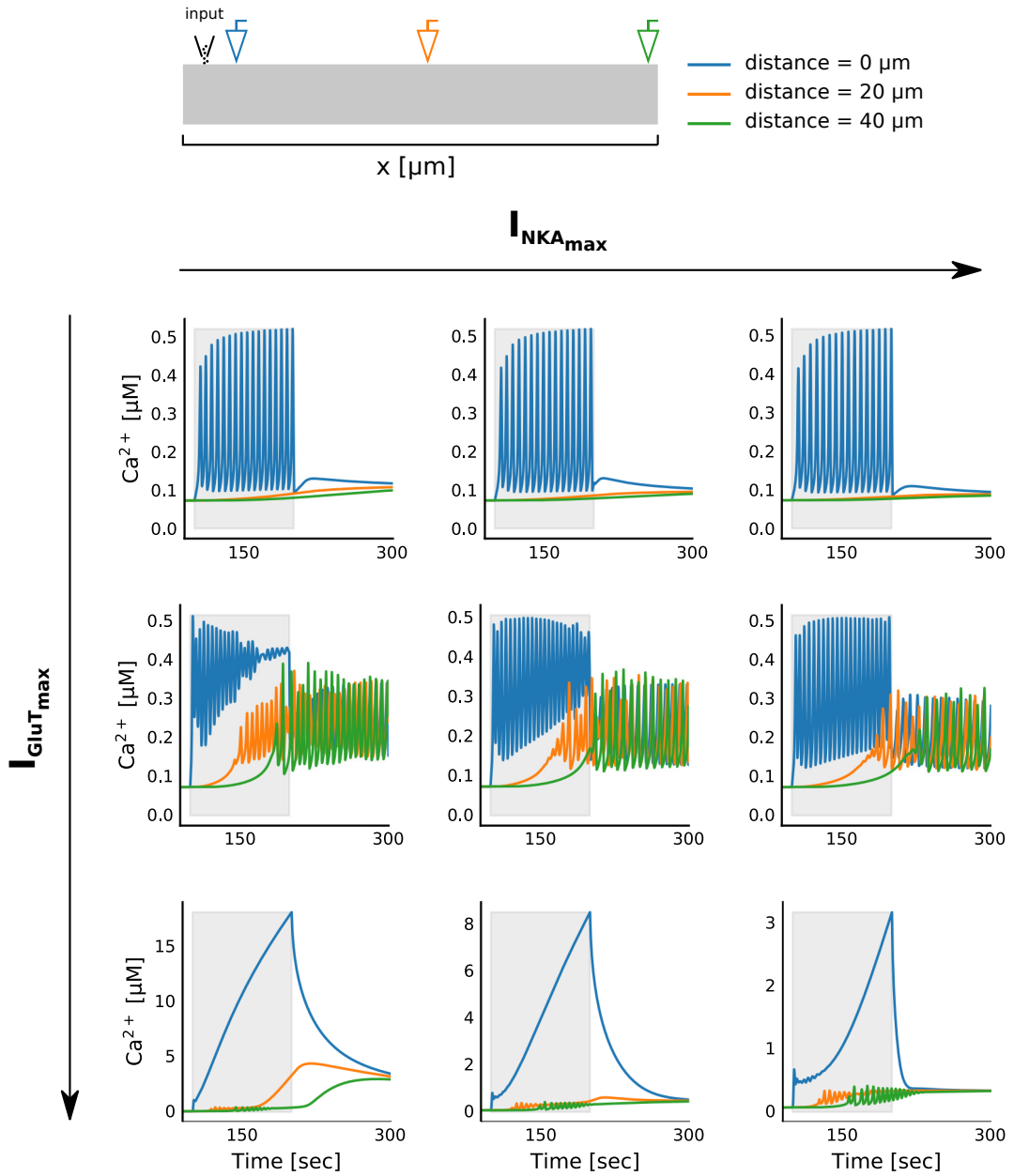


Figure 3.10:  $\text{Ca}^{2+}$  signal propagation as a function of the maximal pump activities of the glutamate transporter ( $I_{\text{GluT}_{\text{max}}}$ ), the  $\text{Na}^+ - \text{K}^+$  pump ( $I_{\text{NKA}_{\text{max}}}$ ) and the  $\text{Na}^+ - \text{Ca}^{2+}$  exchanger ( $I_{\text{NCX}_{\text{max}}}$ ). The considered astrocytic process has a length of  $40 \mu\text{m}$ , a diameter of  $1 \mu\text{m}$  and sealed ends. The astrocytic process is stimulated at the first compartment with a constant glutamate concentration of  $1 \text{ mM}$  for a duration of 100 seconds (see colored gray area). The tortuosities of the intra- and extracellular space are set to their default values. **a** Scheme illustrating the stimulation and recording sites along an astrocytic process of length  $40 \mu\text{m}$ . **b** The propagation of the  $\text{Ca}^{2+}$  signals is depicted for parameter combinations of  $I_{\text{GluT}_{\text{max}}}$  ( $4.8 \frac{\text{A}}{\text{m}^2}$ ,  $6.8 \frac{\text{A}}{\text{m}^2}$ ,  $8.8 \frac{\text{A}}{\text{m}^2}$ ) as well as of  $I_{\text{NKA}_{\text{max}}}$  ( $5.3 \cdot 10^{-6} \frac{\text{A}}{\text{m}^2}$ ,  $5.8 \cdot 10^{-6} \frac{\text{A}}{\text{m}^2}$ ,  $6.3 \cdot 10^{-6} \frac{\text{A}}{\text{m}^2}$ ) and  $I_{\text{NCX}_{\text{max}}}$  equal to  $0.0001 \frac{\text{A}}{\text{m}^2}$ . Each figure shows the intracellular  $\text{Ca}^{2+}$  concentration at three different positions ( $0 \mu\text{m}$ ,  $20 \mu\text{m}$ ,  $40 \mu\text{m}$ ) along an astrocytic process.

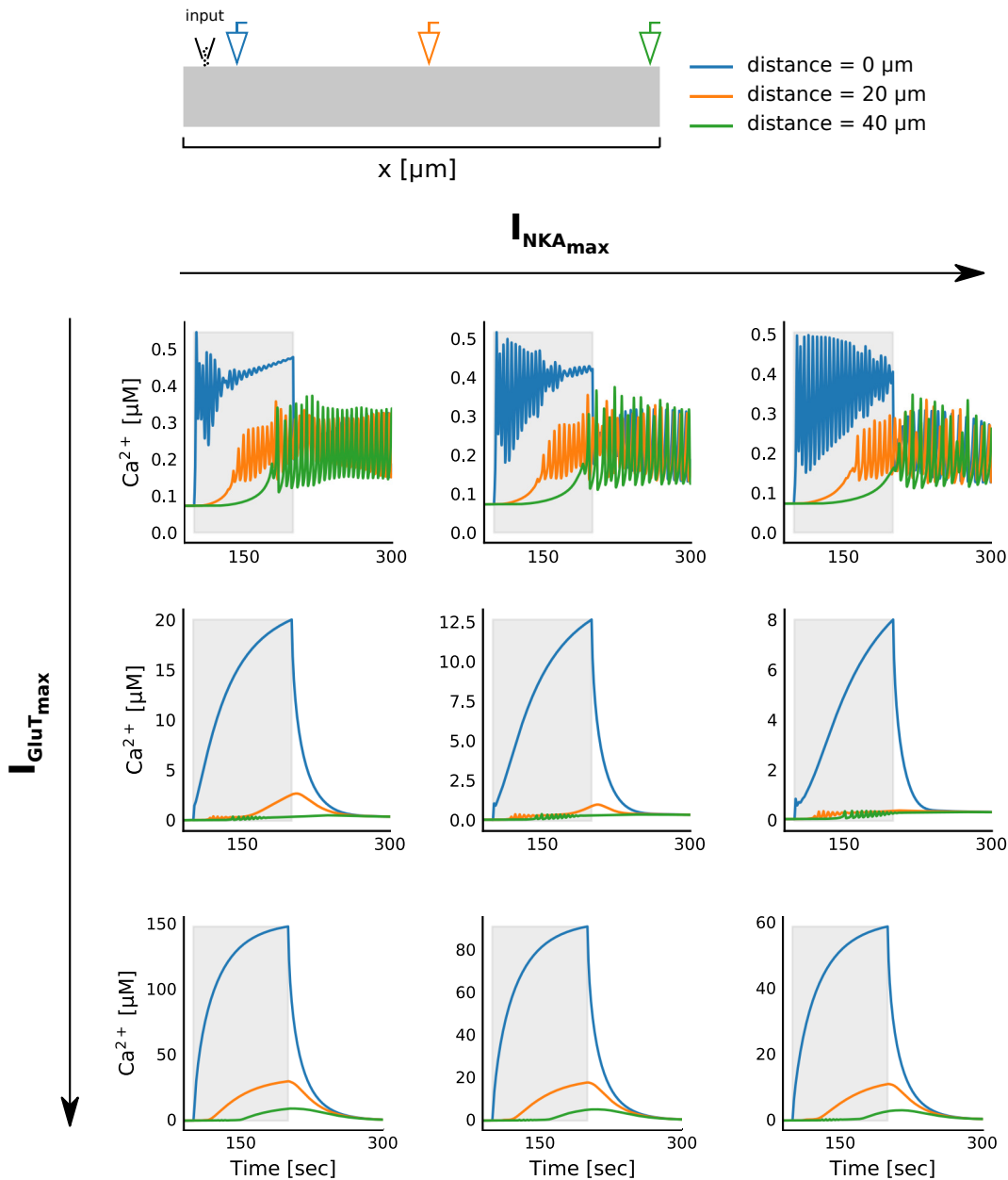


Figure 3.11:  $\text{Ca}^{2+}$  signal propagation as a function of the maximal pump activities of the glutamate transporter ( $I_{\text{GluT}_{\text{max}}}$ ), the  $\text{Na}^+$ - $\text{K}^+$  pump ( $I_{\text{NKA}_{\text{max}}}$ ) and the  $\text{Na}^+$ - $\text{Ca}^{2+}$  exchanger ( $I_{\text{NCX}_{\text{max}}}$ ). The considered astrocytic process has a length of  $40 \mu\text{m}$ , a diameter of  $1 \mu\text{m}$  and sealed ends. The astrocytic process is stimulated at the first compartment with a constant glutamate concentration of  $1 \text{ mM}$  for a duration of  $100$  seconds (see colored gray area). The tortuosities of the intra- and extracellular space are set to their default values. **a** Scheme illustrating the stimulation and recording sites along an astrocytic process of length  $40 \mu\text{m}$ . **b** The propagation of the  $\text{Ca}^{2+}$  signals is depicted for parameter combinations of  $I_{\text{GluT}_{\text{max}}}$  ( $4.8 \frac{\text{A}}{\text{m}^2}$ ,  $6.8 \frac{\text{A}}{\text{m}^2}$ ,  $8.8 \frac{\text{A}}{\text{m}^2}$ ) as well as of  $I_{\text{NKA}_{\text{max}}}$  ( $5.3 \cdot 10^{-6} \frac{\text{A}}{\text{m}^2}$ ,  $5.8 \cdot 10^{-6} \frac{\text{A}}{\text{m}^2}$ ,  $6.3 \cdot 10^{-6} \frac{\text{A}}{\text{m}^2}$ ) and  $I_{\text{NCX}_{\text{max}}}$  equal to  $0.001 \frac{\text{A}}{\text{m}^2}$ . Each figure shows the intracellular  $\text{Ca}^{2+}$  concentration at three different positions ( $0 \mu\text{m}$ ,  $20 \mu\text{m}$ ,  $40 \mu\text{m}$ ) along an astrocytic process.

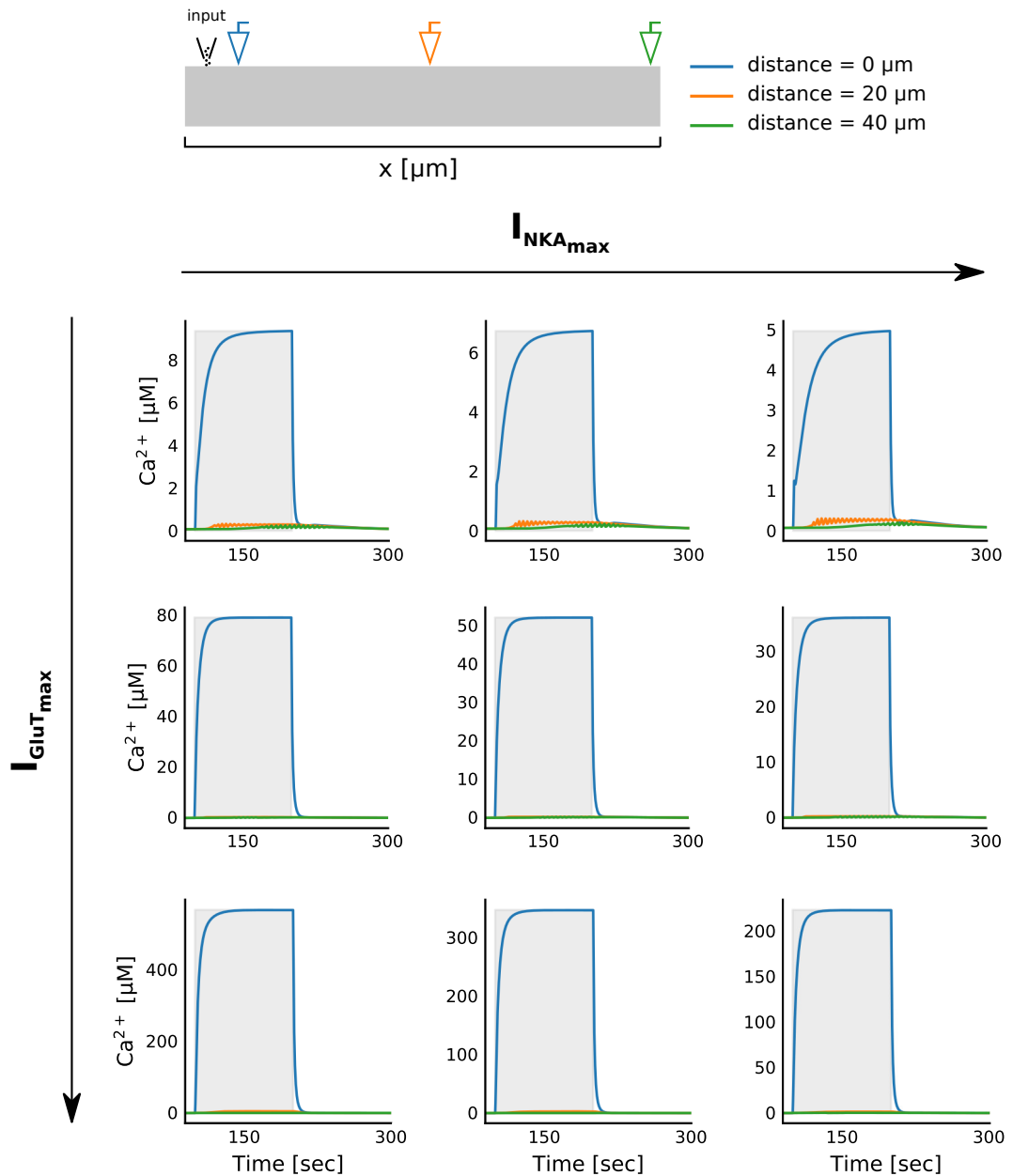


Figure 3.12:  $\text{Ca}^{2+}$  signal propagation as a function of the maximal pump activities of the glutamate transporter ( $I_{\text{Glut}_{\text{max}}}$ ), the  $\text{Na}^+$ - $\text{K}^+$  pump ( $I_{\text{NKA}_{\text{max}}}$ ) and the  $\text{Na}^+$ - $\text{Ca}^{2+}$  exchanger ( $I_{\text{NCX}_{\text{max}}}$ ). The considered astrocytic process has a length of  $40 \mu\text{m}$ , a diameter of  $1 \mu\text{m}$  and sealed ends. The astrocytic process is stimulated at the first compartment with a constant glutamate concentration of  $1 \text{ mM}$  for a duration of  $100$  seconds (see colored gray area). The tortuosities of the intra- and extracellular space are set to their default values. **a** Scheme illustrating the stimulation and recording sites along an astrocytic process of length  $40 \mu\text{m}$ . **b** The propagation of the  $\text{Ca}^{2+}$  signals is depicted for parameter combinations of  $I_{\text{Glut}_{\text{max}}}$  ( $4.8 \frac{\text{A}}{\text{m}^2}$ ,  $6.8 \frac{\text{A}}{\text{m}^2}$ ,  $8.8 \frac{\text{A}}{\text{m}^2}$ ) as well as of  $I_{\text{NKA}_{\text{max}}}$  ( $5.3 \cdot 10^{-6} \frac{\text{A}}{\text{m}^2}$ ,  $5.8 \cdot 10^{-6} \frac{\text{A}}{\text{m}^2}$ ,  $6.3 \cdot 10^{-6} \frac{\text{A}}{\text{m}^2}$ ) and  $I_{\text{NCX}_{\text{max}}}$  equal to  $0.01 \frac{\text{A}}{\text{m}^2}$ . Each figure shows the intracellular  $\text{Ca}^{2+}$  concentration at three different positions ( $0 \mu\text{m}$ ,  $20 \mu\text{m}$ ,  $40 \mu\text{m}$ ) along an astrocytic process.

### 3 Model morphologies

This part of the results section aims to provide examples for different morphologies, which can be applied with the developed computational model. The model allows besides the application of a single astrocytic process either the investigation of a branching process or a process with an open end.

#### 3.1 Branching of the astrocytic process

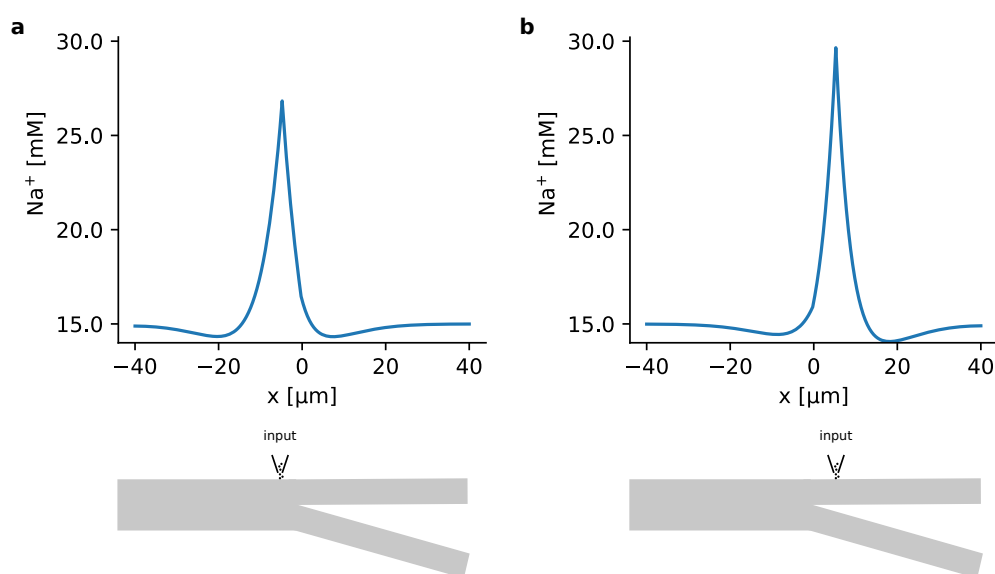


Figure 3.13: **Na<sup>+</sup> signal propagation in a branching astrocytic process.** The branching process is stimulated either at the bigger or the smaller branch with a constant glutamate concentration of 1 mM for a duration of 500 ms. The bigger branch has a diameter of 1  $\mu\text{m}$ , the smaller branches have a diameter of 0.5  $\mu\text{m}$ . All branches have the same length of 40  $\mu\text{m}$ . The outer ends of the branching process are sealed. The tortuosities of the intra- and extracellular space are set to their default values. **a** Spatial profile of the Na<sup>+</sup> concentration along the bigger and one smaller branch of the astrocytic process at the time point of the stimulation offset. Here, the bigger branch of the astrocytic process is stimulated. The scheme below depicts the stimulation site in relation to the branching node. **b** Spatial profile of the Na<sup>+</sup> concentration along the bigger and one smaller branch of the astrocytic process at the time point of the stimulation offset. Here, the smaller branch of the astrocytic process is stimulated. The scheme below depicts the stimulation site in relation to the branching node.

Here, I study the Na<sup>+</sup> signal propagation in a branching astrocytic process (see Figure 3.13, bottom). The bigger branch of the astrocytic process has a diameter of 1  $\mu\text{m}$ , the smaller branches have a diameter of 0.5  $\mu\text{m}$ . All branches have the same length of 40  $\mu\text{m}$  and the outer ends of the branching process are sealed. Moreover, I assume the default values for the tortuosities of the intra- and extracellular space. For the purpose of studying the signal propagation at a branching node, I stimulate the process right before the branching site at either the branch with the larger or the smaller diameter and record the Na<sup>+</sup> concentration.

The main difference between the stimulation of either the bigger or the smaller

branch is the amplitude of the generated  $\text{Na}^+$  signal (see Figure 3.13). While the stimulation of the branch with the larger diameter produces a  $\text{Na}^+$  signal with a lower amplitude (see Figure 3.13 a), the stimulation of the branch with the smaller diameter produces a signal with a larger amplitude (see Figure 3.13 b). Since the stimulated compartment of the bigger branch has a higher volume compared to the one of the smaller branch, the temporal change of the  $\text{Na}^+$  concentration within the bigger branch is smaller and the amplitude is lower. The  $\text{Na}^+$  traces in the two smaller branches are the same.

### 3.2 Open and sealed end of the astrocytic process

As a further variation of the astrocyte morphology I assume the ends of the astrocytic process to be open and investigate the influence of this change on the signal propagation. For this study, I apply a cylinder with a length of  $40 \mu\text{m}$ , a diameter of  $1 \mu\text{m}$  and with either open or sealed ends. Here, I assume the default values for the tortuosity of the intra- and extracellular space. In order to study the signal propagation under these conditions, I stimulate the astrocytic process at its middle compartment and record the  $\text{Na}^+$  and  $\text{Ca}^{2+}$  concentrations at three different positions along the astrocytic process (see Figure 3.14).

The open end condition leads to a higher increase of the  $\text{Na}^+$  concentration at the stimulation site. Moreover, it narrows the signal around the stimulation site and prevents the large undershoot of the  $\text{Na}^+$  concentration (see Figure 3.14 a and b). Due to the open end condition an infinite bath of ions is attached to both ends of the astrocytic process. This also allows an infinite influx of ions through the ends into the astrocytic process. For this reason, not only the diffusion of  $\text{Na}^+$  ions from the stimulation site towards the ends of the astrocytic process is weaker and causes a narrower spatial profile of the  $\text{Na}^+$  concentration, but also prevents the  $\text{Na}^+$  undershoot.

Moreover, the open end condition reduces the propagation radius of the  $\text{Ca}^{2+}$  oscillations (see Figure 3.14 c). While the sealed end condition favors the propagation of long-lasting  $\text{Ca}^{2+}$  oscillations within the whole astrocytic process, the open end condition only allows the propagation of the  $\text{Ca}^{2+}$  oscillation within  $10 \mu\text{m}$  away from the stimulation site. The attached infinite bath functions like a leak current and forces the outer compartments of the astrocytic process, those adjacent to the ends of the process, to keep their  $\text{Ca}^{2+}$  resting concentration. The  $\text{Ca}^{2+}$  resting concentration is too low for the generation of  $\text{Ca}^{2+}$  oscillations and thus the open end condition lets oscillations vanish in compartments close to the ends of the astrocytic process.

In summary, the open end condition functions like an infinite bath of ions attached to the ends of the process. This condition prevents the undershoot of the  $\text{Na}^+$  concentration, but at the same time decreases the  $\text{Ca}^{2+}$  signal propagation radius.

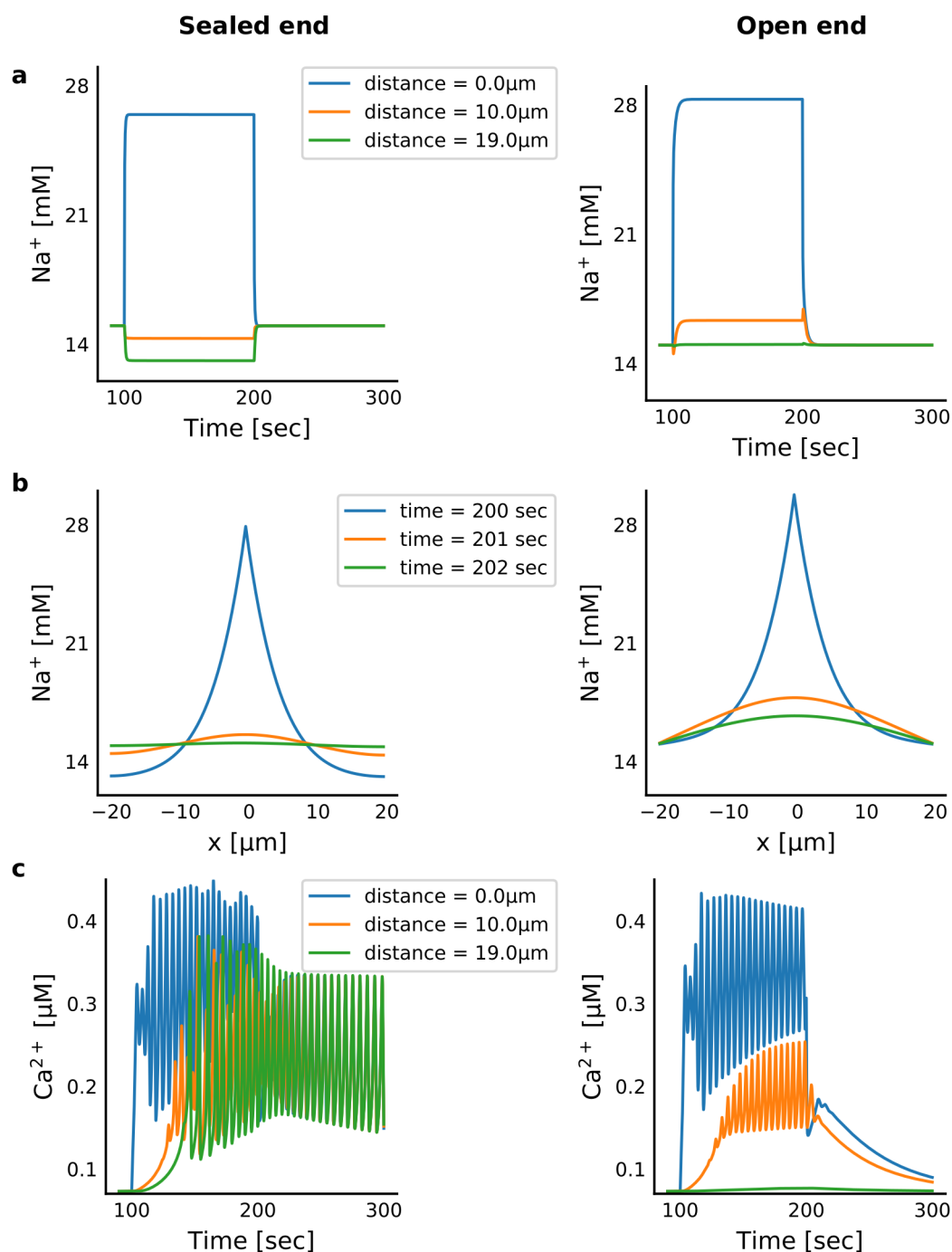


Figure 3.14: **Ca<sup>2+</sup> and Na<sup>+</sup> signal propagation along an astrocytic process with either a sealed or an open end.** The astrocytic process has either a sealed or an open end, a length of 40  $\mu$ m and a diameter of 1  $\mu$ m. The astrocytic process is stimulated at the middle compartment (compartment length = 0.5  $\mu$ m) for a duration of 100 seconds with a constant glutamate concentration of 1 mM. The tortuosities of the intra- and extracellular space are set to their default values. **a** Na<sup>+</sup> signal propagation along an astrocytic processes with either a sealed end (left) or an open end (right). The Na<sup>+</sup> signal is shown for three different distances from the stimulation site (at the stimulation site (distance = 0  $\mu$ m), 10  $\mu$ m away from the stimulation site and 20  $\mu$ m away from the stimulation site.). **b** Spatial profile of the Na<sup>+</sup> concentration along the astrocytic process with either a sealed end (left) or an open end (right). The spatial profile is shown for three different time points (200 seconds, 201 seconds and 202 seconds). The astrocytic process is stimulated at time point 100 seconds and the stimulation lasts 100 seconds. **c** Ca<sup>2+</sup> signal propagation along an astrocytic processes with either a sealed end (left) or an open end (right). The Ca<sup>2+</sup> signal is shown for three different distances from the stimulation site (at the stimulation site (distance = 0  $\mu$ m), 10  $\mu$ m away from the stimulation site and 20  $\mu$ m away from the stimulation site.).

## 4 Modeling of the perisynaptic astrocytic process

This part of the results section aims to give an example for experiments which can be conducted with the multi-compartment model. In this case I model and analyze the  $\text{Ca}^{2+}$  signal propagation at the perisynaptic astrocytic process.  $\text{Ca}^{2+}$  signals in astrocytes can be evoked on several pathways. In general, these pathways can be divided into either a  $\text{Ca}^{2+}$  release from internal stores or a  $\text{Ca}^{2+}$  entry from the extracellular space. Experimental evidence also hints to a spatial separation of these pathways with a primary  $\text{Ca}^{2+}$  entry from the extracellular space at the perisynaptic astrocytic processes and a strong  $\text{Ca}^{2+}$  release from internal stores in the soma (Srinivasan et al., 2015). Moreover, perisynaptic astrocytic processes are assumed to be devoid of internal stores, which does not allow a  $\text{Ca}^{2+}$  release in these subcellular compartments. Based on these experimental results the question arises whether  $\text{Ca}^{2+}$  elevations induced at perisynaptic astrocytic processes can travel along the astrocytic process all the way to subcellular compartments containing internal  $\text{Ca}^{2+}$  stores and induce  $\text{Ca}^{2+}$  release from internal stores and thus also  $\text{Ca}^{2+}$  oscillations. The activation of  $\text{Ca}^{2+}$  release from internal stores in subcellular compartments far away from the synapse is of special interest, since the activation of  $\text{Ca}^{2+}$  release would ensure long-lasting and self-sustained  $\text{Ca}^{2+}$  oscillations which are able to travel all the way to the soma. This form of  $\text{Ca}^{2+}$  propagation would play an important role in the integration of synaptic information within the astrocyte.

For the purpose of modeling the ion dynamics at the perisynaptic astrocytic process, I apply a cylinder with a length of  $40 \mu\text{m}$ , a diameter of  $1 \mu\text{m}$  and with sealed ends. The first  $5 \mu\text{m}$  of the astrocytic process are assumed to be devoid of the internal  $\text{Ca}^{2+}$  store ( $\text{ratio}_{\text{ER}} = 0$ ). This part of the astrocytic process is stimulated and the  $\text{Ca}^{2+}$  and  $\text{Na}^+$  signals are recorded at four different sites along the astrocytic process. The  $\text{Ca}^{2+}$  signal measured at the end of the process is assumed to be equivalent to a  $\text{Ca}^{2+}$  signal, which reaches the soma. If the  $\text{Ca}^{2+}$  signal reaches this point of the process, it is assumed that it would also further propagate to a soma directly following the process. Here, I assume the default values for the tortuosity of the intra- and extracellular space.

I study the ion dynamics at the perisynaptic astrocytic process for different values of the maximal pump current of the  $\text{Na}^+$ - $\text{Ca}^{2+}$  exchanger. The diffusion of  $\text{Ca}^{2+}$  is very slow compared to the one of  $\text{Na}^+$ . Therefore, it is assumed, that mainly the propagating  $\text{Na}^+$  signal and the associated switch of the  $\text{Na}^+$ - $\text{Ca}^{2+}$  exchanger drives the  $\text{Ca}^{2+}$  signal along the astrocytic process to subcellular compartments containing the internal  $\text{Ca}^{2+}$  store. Therefore, I study the effect of the maximal pumping strength of the  $\text{Na}^+$ - $\text{Ca}^{2+}$  exchanger on the  $\text{Ca}^{2+}$  propagation at the perisynaptic astrocytic process.

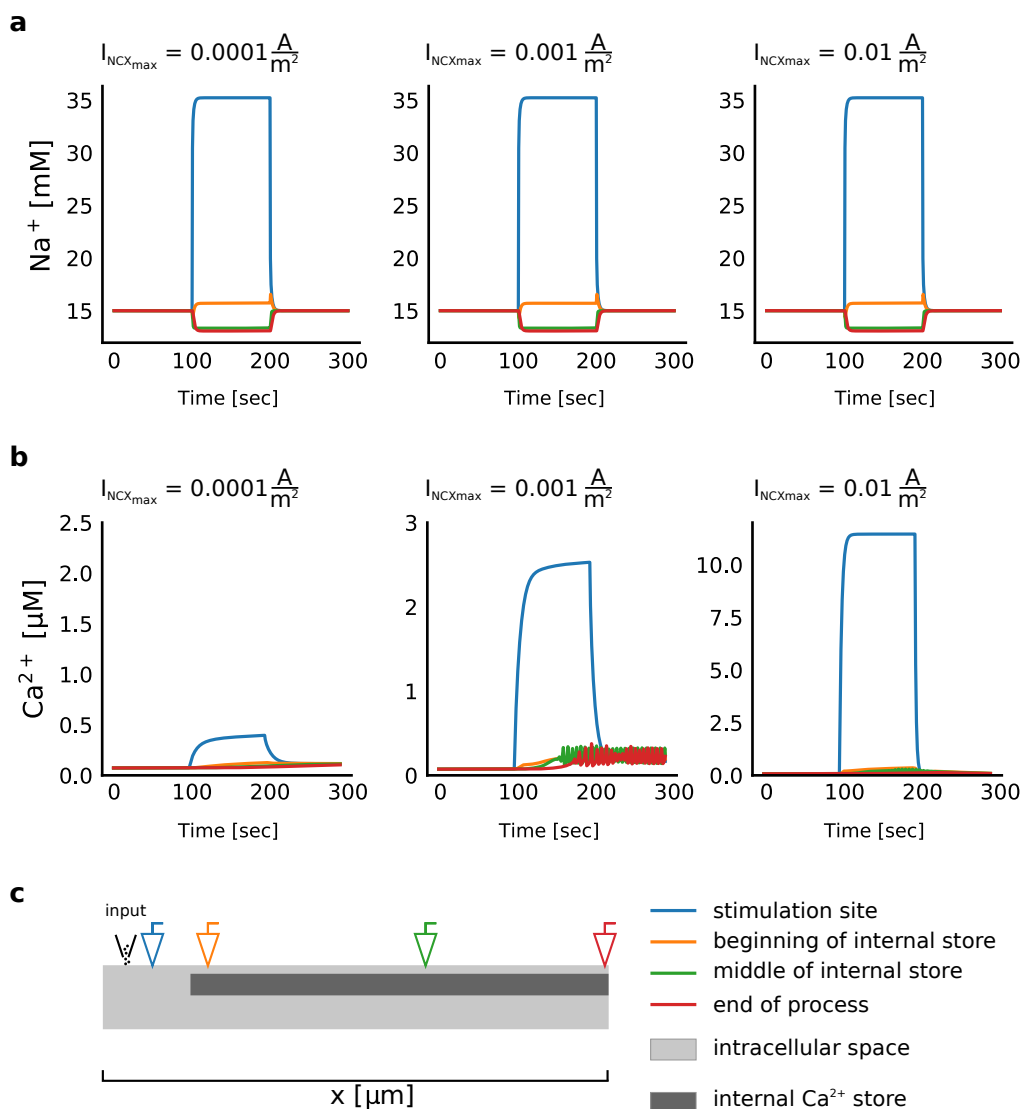


**Figure 3.15: Intracellular Na<sup>+</sup> signals drive the Ca<sup>2+</sup> signal propagation at perisynaptic astrocytic processes.** The time course of the intracellular Na<sup>+</sup> and Ca<sup>2+</sup> concentration for three different positions along the astrocytic process. The time courses of Na<sup>+</sup> and Ca<sup>2+</sup> are shown for three different values for the maximal pump current of the Na<sup>+</sup>-Ca<sup>2+</sup> exchanger ( $I_{\text{NCXmax}} = [0.0001 \frac{\text{A}}{\text{m}^2}, 0.001 \frac{\text{A}}{\text{m}^2}, 0.01 \frac{\text{A}}{\text{m}^2}]$ ). The astrocytic process has a length of 40 μm, a diameter of 1 μm and lacks the internal Ca<sup>2+</sup> store within the first 5 μm of the process. The ends of the process are sealed. The Na<sup>+</sup> and Ca<sup>2+</sup> concentrations are recorded at four different positions along the astrocytic process: at the stimulation site, at the position where the internal Ca<sup>2+</sup> store begins, at the middle of the process and at the end of the process. The tortuosities of the intra- and extracellular space are set to their default values. **a** Time course of the intracellular Na<sup>+</sup> concentration for three different values of the maximal pump current of the Na<sup>+</sup>-Ca<sup>2+</sup> exchanger and four different positions along the astrocytic process. **b** Time course of the intracellular Ca<sup>2+</sup> concentration for three different values of the maximal pump current of the Na<sup>+</sup>-Ca<sup>2+</sup> exchanger and four different positions along the astrocytic process. **c** Scheme depicting the spatial arrangement of the internal Ca<sup>2+</sup> store within the astrocytic process and the recording sites.

The maximal pump current of the  $\text{Na}^+$ - $\text{Ca}^{2+}$  exchanger scales the increase of the intracellular  $\text{Ca}^{2+}$  concentration in compartments devoid of the internal  $\text{Ca}^{2+}$  store. It also determines whether  $\text{Ca}^{2+}$  oscillations are generated and propagate to the end of the process. Different strengths of the  $\text{Na}^+$ - $\text{Ca}^{2+}$  exchanger do not affect the amplitude nor the time course of the intracellular  $\text{Na}^+$  concentration (see Figure 3.15 a). However, the maximal pump activity of the  $\text{Na}^+$ - $\text{Ca}^{2+}$  exchanger strongly affects the  $\text{Ca}^{2+}$  signal generation and propagation along the astrocytic process (see Figure 3.15 b). A low maximal pump current of the  $\text{Na}^+$ - $\text{Ca}^{2+}$  exchanger ( $I_{\text{NCX}_{\text{max}}} = 0.0001 \frac{\text{A}}{\text{m}^2}$ ) merely leads to an increase of the intracellular  $\text{Ca}^{2+}$  concentration, but not to  $\text{Ca}^{2+}$  oscillations. A moderate maximal pump current ( $I_{\text{NCX}_{\text{max}}} = 0.001$ ) allows the generation and propagation of  $\text{Ca}^{2+}$  oscillations up to the end of the astrocytic process. A high maximal pump current in turn suppresses the generation and propagation of  $\text{Ca}^{2+}$  oscillations.

In summary, based on these simulation results I assume, that the high increase of the  $\text{Na}^+$  concentration and the resulting increase of the intracellular  $\text{Ca}^{2+}$  concentration leads to a  $\text{Na}^+$ -driven propagation of  $\text{Ca}^{2+}$  in astrocytic regions devoid if internal stores.

# Discussion

Within this last part of my thesis I developed and studied a multi-compartment model for the propagation of ion signals in astrocytic subsellular compartments. In order to develop the multi-compartment model, I assumed the astrocyte point-model, presented in part 1 of this thesis, to describe the signal generation at one point of an extended astrocyte and coupled the single point-models by diffusion. By that I was able to study signal propagation within an extended astrocytic sub-cellular compartment, like the astrocytic process. The novelty of this model is the consideration of the propagation of calcium, on the one side, and the propagation of sodium and potassium, on the other side.

The key finding of this last part is the strong impact of the sodium on the calcium signal propagation. Since the propagation of sodium and calcium is coupled via the sodium-calcium exchanger, the maximal pump current of the sodium-calcium exchanger has a huge impact on the calcium signal generation. It determines whether the calcium entry from the extracellular space promotes or suppresses the calcium signal generation and propagation. In addition, those parameters shaping the sodium signal propagation, the glutamate transporter and the sodium-potassium pump, also determine the calcium signal propagation. In general, an increase of the glutamate transporter activity and a decrease of the sodium-potassium pump activity led to an increase in both the frequency and the propagation radius of the calcium oscillations. Moreover, a too high calcium influx into the astrocyte, favored by a high activity of the glutamate transporter and the sodium-calcium exchanger, led to a suppression of the calcium oscillations. This observed effect of the glutamate transporter and the sodium-calcium exchanger in the multi-compartment model was similar to the one observed in the single-compartment model (see part 1). Also in the single-compartment model a high activity of these transporters led to the suppression of the calcium oscillations. The reason for this effect was an increased efflux of calcium from the internal calcium store. Thus, the calcium concentration in the internal store decreased to a concentration level, which did not allow the generation of calcium oscillations by calcium release from internal stores any more.

Moreover, I used the developed multi-compartment model to investigate questions that were difficult to address with biological experiments. One example was the signal propagation in small perisynaptic processes as imaging methods did not allow the exact measurement of signals in these small processes. Therefore, I used the multi-compartment model in order to study the calcium and sodium signal

propagation in perisynaptic astrocytic processes. These subcellular regions were devoid of internal calcium stores. The question to investigate was whether the sodium signal propagation is sufficient to transport calcium signals up to a point of the astrocytic process containing an internal calcium store, where they induce calcium release from internal stores. This experiment revealed that especially the strength of the sodium-calcium exchanger affected the calcium signal propagation along the astrocytic process. While the sodium signal was not affected by the strength of the sodium-calcium exchanger, the exchanger primarily determined the amount and time scale of transported calcium into the cell. For all considered maximal pump currents of the sodium-calcium exchanger calcium is transported into the cell, but not in all cases the time-scale of the calcium transport allowed the generation of calcium oscillations. While during a too low transporter activity calcium was transported not fast enough into the cell to activate the IP<sub>3</sub> receptor channels, a too high transporter activity led to a depletion of the calcium store and a suppression of the calcium oscillations. The medium strength of the sodium-calcium exchanger enabled the generation of calcium oscillations. These simulation results showed that especially the sodium signal propagation contributed to the calcium signal propagation at perisynaptic astrocytic processes.

It was noticeable that the calcium signal propagation observed in the simulations had a much smaller propagation radius than it was observed in experiments. Intra- and intercellular calcium waves propagate via gap junctions and spread over long distances (300 - 400  $\mu\text{m}$ ) (Giaume and Venance, 1998; Scemes and Giaume, 2006). When I developed the multi-compartment model I did not adjust the maximal pump currents of the calcium currents at the internal store. As the generation of long-ranging calcium waves requires the release of a lot of calcium from internal stores, it is quite likely that the maximal pump currents change to other values in the multi-compartment model. During the additional consideration of the sodium dynamics, however, the propagation range increased to longer distances. This could imply that the sodium signal propagation has a promoting effect on the propagation of calcium waves. However, the strength of those Ca<sup>2+</sup> currents at the internal store should be investigated in future studies.

Moreover, I could show that especially the sodium signal propagation was affected by the assumed tortuosities in the intra- and extracellular space and by consideration of either an open or a sealed end of the astrocytic process. By assuming different tortuosities in the intra- and extracellular space, different diffusion constants were obtained in these spaces (see Results Section 3). The application of a higher tortuosity in the intracellular space compared to the extracellular space resulted in a lower diffusion constant in the intracellular space. During the application of this imbalance in the diffusion coefficients I could observe an increased flux of sodium out of the cell and the resulting undershoot of the intracellular sodium concentration. However, assuming the same tortuosity and thus the same diffusion coefficient in the intra- and extracellular space prevented such an undershoot. Interestingly, also the consideration of open ends of the astrocytic process prevented an undershoot of the sodium concentration. Since an undershoot of the sodium concentration during the sodium signal propagation has not been reported in experimental studies (Rose

and Karus, 2013), the question arises what the origin of the undershoot is. Various models analyzed diffusive currents in the intra- and extracellular space of glial cells and came to the conclusion that the hindrance of cell structures in the extracellular space is less (Halnes et al., 2013). For this reason, I assume that the same tortuosity in the intra- and extracellular space prevented an undershoot, but the values of the tortuosity were not the main reason for triggering an undershoot. Rather, the closed ends of the process could play a major role, since this condition limited the maximum number of ions in the system. Under physiological conditions the astrocytic process would not be isolated, but coupled to other subcellular compartments like processes and the soma. Thus, in an astrocyte sodium can flow from adjacent subcellular compartments into the astrocytic process and these adjacent compartments would then function as a sodium bath. Therefore, physiological realistic structures, such as the combination of several subcellular compartments, might show a realistic image of signal propagation in astrocytes.

The multi-compartment model presented in this last part of my thesis provided important insights into the interaction between the propagation of sodium and calcium signals. However, there are only few experimental results, which could be used to parameterize and test the model. Although, experimental results on the propagation of calcium and sodium signals exist, the impact of transporter activities on the signal propagation was usually not investigated. Moreover, experimental studies so far focused on the propagation of either calcium or sodium signals and did not investigate the interaction of both ions. This made the parametrization and thus also the interpretation of the simulation results difficult. Since this is only one of the first multi-compartment models for signal propagation in astrocytes, the close interaction between experimentalists and theoreticians is indispensable for the development of further multi-compartment models.



# Discussion and Outlook

## 1 Discussion

Within my thesis I developed a computational model describing the calcium signal generation within one compartment of an extended astrocyte. I further derived a reduced version of this model in order to analyze the steady-state behavior of the model and also combined the point-models (full model) to a multi-compartment model in order to study the signal propagation within the astrocyte.

The novelty of my developed computational model for calcium signal generation in astrocytes (see part 1) is the consideration of two pathways contributing to the signal generation. These pathways are the calcium release from internal stores and the calcium entry from the extracellular space. Whereas the mathematical description of calcium release from internal stores has already been used in numerous models (Li and Rinzel, 1994; Nadkarni and Jung, 2007; De Pittà et al., 2009), the consideration of calcium entry via the sodium-calcium exchanger is new. Published computational models considering the calcium entry from the extracellular space rather focus on voltage-gated calcium channels (Postnov et al., 2008; Zeng et al., 2009; Li et al., 2012). Moreover, the model can be parameterized for different positions along the astrocytic process by varying the surface volume ratio of the astrocytic compartment together with the volume fraction of internal calcium store. Thus, my point-model of an astrocyte allows to study the generation of calcium signals under different morphological conditions.

Within the second part of my thesis I derived a reduced version of the model presented in part 1 by a separation of time scales of the model variables. On the one hand, this reduced model has very well mapped the quantitative and qualitative behavior of the full model, and, on the other hand, the reduced model enabled a detailed analytic model investigation in order to predict its steady-state behavior. This approach of the separate computation of the steady-state values of the fast model variables and the subsequent analysis of the reduced model behavior differs significantly from other computational studies investigating calcium signal generation in astrocytes. Most other computational models either focus on only one mechanisms for the generation of calcium signals in astrocytes and are thus easy to analyze, or consider more than one mechanisms and are thus high-dimensional and complicated to analyze. My approach takes different mechanisms for the generation of calcium signals into account and still allows a detailed model analysis. Thus, my approach gives important insights into the interaction of the mechanisms,

which would not be offered by numerical simulations.

Object of the third part of this thesis is the development of a multi-compartment model for the signal propagation in astrocytic subcellular compartments. In order to do so I diffusively coupled the single-point models presented in the first part of the thesis. The obtained multi-compartment model allowed me to study the propagation of calcium and sodium signals along a single astrocytic process or along a branching process. To my best knowledge the developed multi-compartment model is the first, which combines calcium and sodium dynamics in astrocytes. Other computational models rather focus on the propagation of calcium waves within astrocyte networks (Ullah et al., 2006; Kang and Othmer, 2009) than on the propagation along one astrocytic process. Thus, the multi-compartment model allows to study complex propagation patterns like for example the interaction of calcium and sodium signal propagation.

In summary, my developed models allow to study the generation and propagation of calcium signals in astrocytes and by that contribute to a better understanding of the astrocyte function. However, the investigation of astrocytes has only begun many decades after that of neurons. Thus, computational models of astrocytes are not yet as sophisticated in terms of the investigation of the signal propagation or the astrocyte morphology as neuron models. Furthermore, existing astrocyte models function either as a reproduction of experimental data or as an extension of experiments and by that investigate problems which are not accessible with current experimental methods. For the purpose of developing and applying astrocyte models more specifically, a close cooperation between experimentalists and theoreticians is essential. In this way a close link between model predictions, which are tested in experiments, and model fine tuning, which is based on experimental data, could be implemented. Based on this, important aspects regarding the functional role of astrocytes in neural information processing could be targeted.

## 2 Outlook

Based on the results presented in this thesis, several model extensions and future studies are possible. This possible future studies can be divided into extensions of the single-compartment model and the multi-compartment model.

The single-compartment model could be extended with further mechanisms mediating a calcium entry from the extracellular space. Possible mechanisms are for example voltage-gated calcium channels or store-operated calcium channels. These mechanisms could be applied to both the full and the reduced model in order to investigate the model behavior in response to time-varying and constant stimuli, respectively. Moreover, further channels mediating a sodium influx like the NMDA-receptors could be added to the model. By considering additional NMDA-receptors, the model could account for astrocytes in different brain regions as NMDA receptors are mainly expressed in cortical astrocytes (Conti et al., 1997; Verkhratsky et al., 1998; Conti et al., 1999). Moreover, the single-compartment model could be extended with calcium buffering as calcium-binding proteins determine the amount of free calcium in a cell. Experimental studies could prove the effect

of calcium-binding proteins on the intra- and intercellular propagation of calcium signals (Wang et al., 1997; Gerlai et al., 1995). In order to develop and analyze a computational model for calcium buffering in astrocytes, I would suggest to first extend the single-compartment model with calcium buffering. Subsequently, I would introduce this mechanisms to the multi-compartment model in order to study the effect of calcium buffering on intracellular calcium signal propagation.

The multi-compartment model could be extended with more complex and realistic morphologies. For example, it would be conceivable to link several processes that form a primary branch. Furthermore, so far the signal propagation within the soma has not been considered. Especially in the soma the signal propagation in three directions is of great importance. Therefore, a more detailed model, which takes the propagation of the signals into three directions into account, should be used for the modeling of the soma. Once a detailed model of the soma and primary astrocytic branches is developed, a combination of these structures could be used to investigate the integration of neuronal signals within the astrocyte.



# Bibliography

- Abbott, Rönnbäck, and Hansson. 2006. Astrocyte-endothelial interactions at the blood-brain barrier, 2006. ISSN 1471003X. URL <http://www.nature.com/articles/nrn1824>.
- Agulhon, Petravicz, McMullen, Sweger, Minton, Taves, Casper, Fiacco, and McCarthy. 2008. What is the role of astrocyte calcium in neurophysiology? *Neuron*. doi: 10.1016/j.neuron.2008.09.004.
- Amiri, Hosseinmardi, Bahrami, and Janahmadi. 2013. Astrocyte-neuron interaction as a mechanism responsible for generation of neural synchrony: a study based on modeling and experiments. *Journal of Computational Neuroscience*. doi: 10.1007/s10827-012-0432-6.
- Bazargani and Attwell. 2016. Astrocyte calcium signaling: the third wave. *Nature Neuroscience*. doi: 10.1038/nn.4201.
- Bindocci, Savtchouk, Liaudet, Becker, Carriero, and Volterra. 2017. Neuroscience: Three-dimensional Ca<sup>2+</sup> imaging advances understanding of astrocyte biology. *Science*. doi: 10.1126/science.aai8185.
- Blaustein and Santiago. 1977. Effects of internal and external cations and of ATP on sodium-calcium and calcium-calcium exchange in squid axons. *Biophys J*.
- Boulay, Brown, Qin, Jiang, Dietrich, Zhu, Chen, Birnbaumer, Mikoshiba, and Birnbaumer. 1999. Modulation of Ca(2+) entry by polypeptides of the inositol 1,4,5-trisphosphate receptor (IP3R) that bind transient receptor potential (TRP): evidence for roles of TRP and IP3R in store depletion-activated Ca(2+) entry. *Proceedings of the National Academy of Sciences of the United States of America*. doi: 10.1073/pnas.96.26.14955.
- Canchi, Sarntinoranont, Hong, Flint, Subhash, and King. 2017. Simulated blast overpressure induces specific astrocyte injury in an ex vivo brain slice model. *PLoS ONE*. doi: 10.1371/journal.pone.0175396.
- Charles, Merrill, Dirksen, and Sandersont. 1991. Intercellular signaling in glial cells: Calcium waves and oscillations in response to mechanical stimulation and glutamate. *Neuron*. doi: 10.1016/0896-6273(91)90238-U.

- Chatton, Marquet, and Magistretti. 2000. A quantitative analysis of l-glutamate-regulated Na<sup>+</sup> dynamics in mouse cortical astrocytes: implications for cellular bioenergetics. *European Journal of Neuroscience*. doi: 10.1046/j.1460-9568.2000.00269.x.
- Chatton, Pellerin, and Magistretti. 2003. GABA uptake into astrocytes is not associated with significant metabolic cost: implications for brain imaging of inhibitory transmission. *PNAS*. doi: 10.1073/pnas.2132096100.
- Conti, Barbaresi, Melone, and Ducati. 1999. Neuronal and glial localization of NR1 and NR2A/B subunits of the NMDA receptor in the human cerebral cortex. *Cerebral Cortex*.
- Conti, Minelli, DeBiasi, and Melone. 1997. Neuronal and glial localization of NMDA receptors in the cerebral cortex. *Molecular neurobiology*.
- Cornell-Bell, Finkbeiner, Cooper, and Smith. 1990. Glutamate induces calcium waves in cultured astrocytes: Long-range glial signaling. *Science*. doi: 10.1126/science.1967852.
- Danbolt. 2001. Glutamate uptake, 2001.
- De Pittà, Goldberg, Volman, Berry, and Ben-Jacob. 2009. Glutamate regulation of calcium and IP<sub>3</sub> oscillating and pulsating dynamics in astrocytes. *Journal of Biological Physics*.
- Diniz, Oliveira, Lima, Foro, Sosthenes, Bento-Torres, Costa Vasconcelos, Anthony, and Diniz. 2016. Age, environment, object recognition and morphological diversity of GFAP-immunolabeled astrocytes. *Behavioral and Brain Functions*. doi: 10.1186/s12993-016-0111-2.
- Doengi, Hirnet, Coulon, Pape, Deitmer, and Lohr. 2009. GABA uptake-dependent Ca<sup>2+</sup> signaling in developing olfactory bulb astrocytes. *Proceedings of the National Academy of Sciences*. doi: 10.1073/pnas.0809513106.
- Dupont and Goldbeter. 1993. One-pool model for Ca<sup>2+</sup> oscillations involving Ca<sup>2+</sup> and inositol 1,4,5-trisphosphate as co-agonists for Ca<sup>2+</sup> release. *Cell Calcium*.
- Falcke, Hudson, Camacho, and Lechleiter. 1999. Impact of Mitochondrial Ca<sup>2+</sup> Cycling on Pattern Formation and Stability. *Biophysical Journal*. doi: 10.1016/S0006-3495(99)76870-0.
- Fuhrmann, Markram, and Tsodyks. 2002. Spike frequency adaptation and neocortical rhythms. *J. Neurophysiol.*
- García-Marín, García-López, and Freire. 2007. Cajal's contributions to glia research, 2007. ISSN 01662236.
- Gerlai, Wojtowicz, Marks, and Roder. 1995. Overexpression of a calcium-binding protein, S100 beta, in astrocytes alters synaptic plasticity and impairs spatial learning in transgenic mice. *Learning & memory (Cold Spring Harbor, N.Y.)*.

- Giaume and Venance. 1998. Intercellular calcium signaling and gap junctional communication in astrocytes. *Glia*.
- Goldman, Yarowsky, Juhaszova, Krueger, and Blaustein. 1994. Sodium/calcium exchange in rat cortical astrocytes. *J Neurosci*.
- Golovina and Blaustein. 2000. Unloading and refilling of two classes of spatially resolved endoplasmic reticulum Ca<sup>2+</sup> stores in astrocytes. *Glia*.
- Golovina. 2005. Visualization of localized store-operated calcium entry in mouse astrocytes. Close proximity to the endoplasmic reticulum. *Journal of Physiology*. doi: 10.1113/jphysiol.2005.085035.
- Goodman and Brette. 2008. Brian: a simulator for spiking neural networks in python. *Frontiers in neuroinformatics*. doi: 10.3389/neuro.11.005.2008.
- Goto, Kinoshita, and Natsume. 2004. The model of glutamate-induced intracellular Ca<sup>2+</sup> oscillation and intercellular Ca<sup>2+</sup> wave in brain astrocytes. *Neurocomputing*.
- Halnes, Østby, Pettersen, Omholt, and Einevoll. 2013. Electrodiffusive Model for Astrocytic and Neuronal Ion Concentration Dynamics. *PLoS Computational Biology*.
- Hamilton, Vayro, Kirchhoff, Verkhatsky, Robbins, Gorecki, and Butt. 2008. Mechanisms of ATP- and glutamate-mediated calcium signaling in white matter astrocytes. *GLIA*. doi: 10.1002/glia.20649.
- Handy, Taheri, White, and Borisjuk. 2017. Mathematical investigation of IP<sub>3</sub>-dependent calcium dynamics in astrocytes. *Journal of Computational Neuroscience*. doi: 10.1007/s10827-017-0640-1.
- Henneberger, Papouin, Oliet, and Rusakov. 2010. Long-term potentiation depends on release of D-serine from astrocytes. *Nature*. doi: 10.1038/nature08673.
- Hines. 1984. Efficient computation of branched nerve equations. *International Journal of Bio-Medical Computing*. doi: 10.1016/0020-7101(84)90008-4.
- Höfer, Venance, and Giaume. 2002. Control and plasticity of intercellular calcium waves in astrocytes: a modeling approach. *The Journal of Neuroscience*.
- Horak, Nashner, and Diener. 1990. Characterization of glutamate uptake into and release from astrocytes and neurons cultured from different brain regions. *Experimental Brain Research*. doi: 10.1007/BF00239385.
- Kanemaru, Sekiya, Xu, Satoh, Kitajima, Yoshida, Okubo, Sasaki, Moritoh, Hasuwa, Mimura, Horikawa, Matsui, Nagai, Iino, and Tanaka. 2014. In Vivo visualization of subtle, transient, and local activity of astrocytes using an ultrasensitive Ca<sup>2+</sup> indicator. *Cell Reports*. doi: 10.1016/j.celrep.2014.05.056.
- Kang, Jiang, Goldman, and Nedergaard. 1998. Astrocyte-mediated potentiation of inhibitory synaptic transmission. *Nature Neuroscience*. doi: 10.1038/3684.

- Kang and Othmer. 2009. Spatiotemporal characteristics of calcium dynamics in astrocytes. *Chaos (Woodbury, N.Y.)*. doi: 10.1063/1.3206698.
- Kanner and Bendahan. 1982. Binding order of substrates to the sodium and potassium ion coupled L-glutamic acid transporter from rat brain. *Biochemistry*. doi: 10.1021/bi00267a044.
- Kaplan. 2002. Biochemistry of Na<sup>+</sup>-K<sup>+</sup>-ATPase. *Annual Review of Biochemistry*. doi: 10.1146/annurev.biochem.71.102201.141218.
- Kettenmann and Ransom. 2013. *Neuroglia*. Oxford University Press. ISBN 9780199794591.
- Kettenmann and Verkhratsky. 2008. Neuroglia: the 150 years after, 2008.
- Kirischuk and Kettenmann. 1997. Na<sup>+</sup>/Ca<sup>2+</sup>-exchanger modulates Ca<sup>2+</sup> signaling in Bergmann glial cells in situ. *Federation of American Societies for Experimental Biology*.
- Kirischuk, Kettenmann, and Verkhratsky. 2007. Membrane currents and cytoplasmic sodium transients generated by glutamate transport in Bergmann glial cells. *Pflügers Archiv - European Journal of Physiology*. doi: 10.1007/s00424-007-0207-5.
- Kirischuk, Parpura, and Verkhratsky. 2012. Sodium dynamics: another key to astroglial excitability? *Trends in Neurosciences*. doi: 10.1016/j.tins.2012.04.003.
- Koch. 1999. *BIOPHYSICS OF COMPUTATION*. Oxford University Press, New York.
- Kuffler, Nicholls, and Orkand. 1966. Physiological properties of glial cells in the central nervous system of amphibia. *Journal of neurophysiology*. doi: MO1.
- Langer, Stephan, Theis, and Rose. 2012. Gap junctions mediate intercellular spread of sodium between hippocampal astrocytes in situ. *Glia*.
- Langer, Gerkau, Derouiche, Kleinhans, Moshrefi-Ravasdjani, Fredrich, Kafitz, Seifert, Steinhäuser, and Rose. 2016. Rapid sodium signaling couples glutamate uptake to breakdown of ATP in perivascular astrocyte endfeet, 2016.
- Langer and Rose. 2009. Synaptically induced sodium signals in hippocampal astrocytes in situ. *Journal of Physiology*. doi: 10.1113/jphysiol.2009.182279.
- Li, Chen, Zeng, Luo, and Li. 2012. Modeling the Contributions of Ca<sup>2+</sup> Flows to Spontaneous Ca<sup>2+</sup> Oscillations and Cortical Spreading Depression-Triggered Ca<sup>2+</sup> Waves in Astrocyte Networks. *PLoS ONE*. doi: 10.1371/journal.pone.0048534.
- Li and Rinzel. 1994. Equations for InsP<sub>3</sub> Receptor-mediated [Ca<sup>2+</sup>]<sub>i</sub> Oscillations Derived from a Detailed Kinetic Model: A Hodgkin-Huxley Like Formalism. *Journal of Theoretical Biology*.

- Luo and Rudy. 1994. A dynamic model of the cardiac ventricular action potential. I. Simulations of ionic currents and concentration changes. *Circulation research*.
- Manninen, Havela, and Linne. 2018. Computational Models for Calcium-Mediated Astrocyte Functions. *Frontiers in Computational Neuroscience*. doi: 10.3389/fncom.2018.00014.
- Mathiisen, Lehre, Danbolt, and Ottersen. 2010. The perivascular astroglial sheath provides a complete covering of the brain microvessels: An electron microscopic 3D reconstruction. *GLIA*. doi: 10.1002/glia.20990.
- McCaslin, Chen, Radosevich, Cauli, and Hillman. 2011. In vivo 3D morphology of astrocyte-vasculature interactions in the somatosensory cortex: Implications for neurovascular coupling. *Journal of Cerebral Blood Flow and Metabolism*. doi: 10.1038/jcbfm.2010.204.
- McKhann, D'Ambrosio, and Janigro. 1997. Heterogeneity of astrocyte resting membrane potentials and intercellular coupling revealed by whole-cell and gramicidin-perforated patch recordings from cultured neocortical and hippocampal slice astrocytes. *The Journal of neuroscience : the official journal of the Society for Neuroscience*.
- Minelli, Castaldo, Gobbi, Salucci, Magi, and Amoroso. 2007. Cellular and subcellular localization of Na<sup>+</sup>-Ca<sup>2+</sup> exchanger protein isoforms, NCX1, NCX2, and NCX3 in cerebral cortex and hippocampus of adult rat. *Cell Calcium*.
- Nadkarni and Jung. 2007. Modeling synaptic transmission of the tripartite synapse. *Physical biology*. doi: 10.1088/1478-3975/4/1/001.
- Nedergaard, Ransom, and Goldman. 2003. New roles for astrocytes: Redefining the functional architecture of the brain, 2003. URL <http://tins.trends.com>.
- Norenberg and Martinez-Hernandez. 1979. Fine structural localization of glutamine synthetase in astrocytes of rat brain. *Brain Research*. doi: 10.1016/0006-8993(79)90071-4.
- Orkand, Nicholls, and Kuffler. 1966. Effect of nerve impulses on the membrane potential of glial cells in the central nervous system of amphibia. *Journal of neurophysiology*. doi: 10.1152/jn.1966.29.4.788.
- Oschmann, Berry, Obermayer, and Lenk. 2017a. From in silico astrocyte cell models to neuron-astrocyte network models: A review. *Brain research bulletin*. doi: 10.1016/j.brainresbull.2017.01.027.
- Oschmann, Mergenthaler, Jungnickel, and Obermayer. 2017b. Spatial separation of two different pathways accounting for the generation of calcium signals in astrocytes. *PLOS Computational Biology*. doi: 10.1371/journal.pcbi.1005377.

- Østby, Øyehaug, Einevoll, Nagelhus, Plahte, Zeuthen, Lloyd, Ottersen, and Omholt. 2009. Astrocytic mechanisms explaining neural-activity-induced shrinkage of extraneuronal space. *PLoS Computational Biology*. doi: 10.1371/journal.pcbi.1000272.
- Parekh and Lewis. 2005. Store-Operated Calcium Channels. *Physiological Reviews*. doi: 10.1152/physrev.00057.2003.
- Pasti, Zonta, Pozzan, Vicini, and Carmignoto. 2001. Cytosolic calcium oscillations in astrocytes may regulate exocytotic release of glutamate. *The Journal of neuroscience : the official journal of the Society for Neuroscience*. doi: 10.1523/JNEUROSCI.2112-01.2001.
- Patrushev, Gavrilov, Turlapov, and Semyanov. 2013. Subcellular location of astrocytic calcium stores favors extrasynaptic neuron–astrocyte communication. *Cell Calcium*.
- Perea, Navarrete, and Araque. 2009. Tripartite synapses: astrocytes process and control synaptic information. *Trends in Neurosciences*.
- Pizzo, Burgo, Pozzan, and Fasolato. 2001. Role of capacitative calcium entry on glutamate-induced calcium influx in type-I rat cortical astrocytes. *Journal of Neurochemistry*. doi: 10.1046/j.1471-4159.2001.00539.x.
- Postnov, Ryazanova, Brazhe, Brazhe, Maximov, Mosekilde, and Sosnovtseva. 2008. Giant glial cell: New insight through mechanism-based modeling. *Journal of Biological Physics*.
- Putney. 1986. A model for receptor-regulated calcium entry. *Cell Calcium*. doi: 10.1016/0143-4160(86)90026-6.
- Qian and Sejnowski. 1989. An electro-diffusion model for computing membrane potentials and ionic concentrations in branching dendrites, spines and axons. *Biological Cybernetics*. doi: 10.1007/BF00217656.
- Reyes, Verkhratsky, and Parpura. 2012. Plasmalemmal Na<sup>+</sup>/Ca<sup>2+</sup> exchanger modulates Ca<sup>2+</sup>-dependent exocytotic release of glutamate from rat cortical astrocytes. *ASN neuro*.
- Rojas, Colina, Ramos, Benaim, Jaffe, Caputo, and DiPolo. 2007. Na<sup>+</sup> entry via glutamate transporter activates the reverse Na<sup>+</sup>/Ca<sup>2+</sup> exchange and triggers Ca<sup>2+</sup>-induced Ca<sup>2+</sup> release in rat cerebellar Type-1 astrocytes. *Journal of Neurochemistry*.
- Rose. 2002. Book Review: Na<sup>+</sup> Signals at Central Synapses. *The Neuroscientist*. doi: 10.1177/1073858402238512.
- Rose and Karus. 2013. Two sides of the same coin: Sodium homeostasis and signaling in astrocytes under physiological and pathophysiological conditions. *Glia*.
- Rose, Koo, Antflick, Ahmed, Angers, and Hampson. 2009. Glutamate transporter coupling to Na,K-ATPase. *The Journal of neuroscience : the official journal of the Society for Neuroscience*. doi: 10.1523/JNEUROSCI.1081-09.2009.

- Rusakov, Zheng, and Henneberger. 2011. Astrocytes as Regulators of Synaptic Function A Quest for the Ca<sup>2+</sup> Master Key. *The Neuroscientist*. doi: 10.1177/1073858410387304.
- Sahlender, Savtchouk, and Volterra. 2014. What do we know about gliotransmitter release from astrocytes?, 2014. ISSN 14712970.
- Scemes. 2000. Components of Astrocytic Intercellular Calcium Signaling. *Molecular Neurobiology*.
- Scemes and Giaume. 2006. Astrocyte calcium waves: What they are and what they do, 2006. ISSN 08941491.
- Schummers, Yu, and Sur. 2008. Tuned responses of astrocytes and their influence on hemodynamic signals in the visual cortex. *Science*.
- Sergeeva, Strokin, Wang, Ubl, and Reiser. 2003. Arachidonic acid in astrocytes blocks Ca<sup>2+</sup> oscillations by inhibiting store-operated Ca<sup>2+</sup> entry, and causes delayed Ca<sup>2+</sup> influx, 2003. ISSN 01434160.
- Sheppard, Simpson, Sharp, Nucifora, Ross, Lange, and Russell. 1997. Comparison of Type 2 Inositol 1,4,5-Trisphosphate Receptor Distribution and Subcellular Ca<sup>2+</sup> Release Sites that Support Ca<sup>2+</sup> Waves in Cultured Astrocytes. *Journal of Neurochemistry*.
- Shigetomi, Tong, Kwan, Corey, and Khakh. 2012. TRPA1 channels regulate astrocyte resting calcium and inhibitory synapse efficacy through GAT-3. *Nature Neuroscience*. doi: 10.1038/nn.3000.
- Somjen. 1979. Extracellular potassium in the mammalian central nervous system. *Annu Rev Physiol*. doi: 10.1146/annurev.ph.41.030179.001111.
- Spät, Bradford, McKinney, Rubin, and Putney. 1986. A saturable receptor for 32P-inositol-1,4,5-trisphosphate in hepatocytes and neutrophils. *Nature*. doi: 10.1038/319514a0.
- Srinivasan, Huang, Venugopal, Johnston, Chai, Zeng, Golshani, and Khakh. 2015. Ca(2+) signaling in astrocytes from Ip3r2(-/-) mice in brain slices and during startle responses in vivo. *Nature neuroscience*.
- Stobart, Ferrari, Barrett, Stobart, Looser, Saab, and Weber. 2016. Long-term In Vivo Calcium Imaging of Astrocytes Reveals Distinct Cellular Compartment Responses to Sensory Stimulation. *Cerebral Cortex*. doi: 10.1093/cercor/bhw366.
- Streb, Irvine, Berridge, and Schulz. 1983. Release of Ca<sup>2+</sup> from a nonmitochondrial intracellular store in pancreatic acinar cells by inositol-1,4,5-trisphosphate. *Nature*. doi: 10.1038/306067a0.
- Tsodyks and Markram. 1997. The neural code between neocortical pyramidal neurons depends on neurotransmitter release probability. *Proceedings of the National Academy of Sciences*. doi: 10.1073/pnas.94.2.719.

- Tzingounis and Wadiche. 2007. Glutamate transporters: confining runaway excitation by shaping synaptic transmission. *Nat Rev Neurosci*. doi: 10.1038/nrn2274.
- Ullah, Jung, and Cornell-Bell. 2006. Anti-phase calcium oscillations in astrocytes via inositol (1, 4, 5)-trisphosphate regeneration. *Cell Calcium*. doi: 10.1016/j.ceca.2005.10.009.
- Verkhratsky and Steinhäuser. 2000. Ion channels in glial cells, 2000. ISSN 01650173.
- Verkhratsky, Orkand, and Kettenmann. 1998. Glial calcium: homeostasis and signaling function. *Physiological reviews*. doi: 10.1152/physrev.1998.78.1.99.
- Virchow. 1858. *Cellular pathology: as based upon physiological and pathological histology. Twenty lectures delivered in the pathological institute of Berlin during the months of February, March and April, 1858 [in German]*. Berlin.
- Wadiche, Arriza, Amara, and Kavanaugh. 1995. Kinetics of a human glutamate transporter. *Neuron*. doi: 0896-6273(95)90340-2[pii].
- Wallach, Lallouette, Herzog, De Pittà, Jacob, Berry, and Hanein. 2014. Glutamate Mediated Astrocytic Filtering of Neuronal Activity. *PLoS Computational Biology*.
- Walz and Hinks. 1986. A transmembrane sodium cycle in astrocytes. *Brain Research*. doi: 10.1016/0006-8993(86)90565-2.
- Wang, Tymianski, Jones, and Nedergaard. 1997. Impact of cytoplasmic calcium buffering on the spatial and temporal characteristics of intercellular calcium signals in astrocytes. *The Journal of Neuroscience*.
- Zeng, Li, Zeng, and Chen. 2009. Simulation of Spontaneous Ca<sup>2+</sup> Oscillations in Astrocytes Mediated by Voltage-Gated Calcium Channels. *Biophysical Journal*. doi: 10.1016/j.bpj.2009.08.030.
- Zhang, Bassam, Thomas, Williams, Liu, Nance, Rojas, Slusher, and Kannan. 2016. Maternal inflammation leads to impaired glutamate homeostasis and up-regulation of glutamate carboxypeptidase II in activated microglia in the fetal/newborn rabbit brain. *Neurobiology of Disease*. doi: 10.1016/j.nbd.2016.06.010.